Emergent Properties of Two-Dimensional Materials

Flatlands beyond Graphene

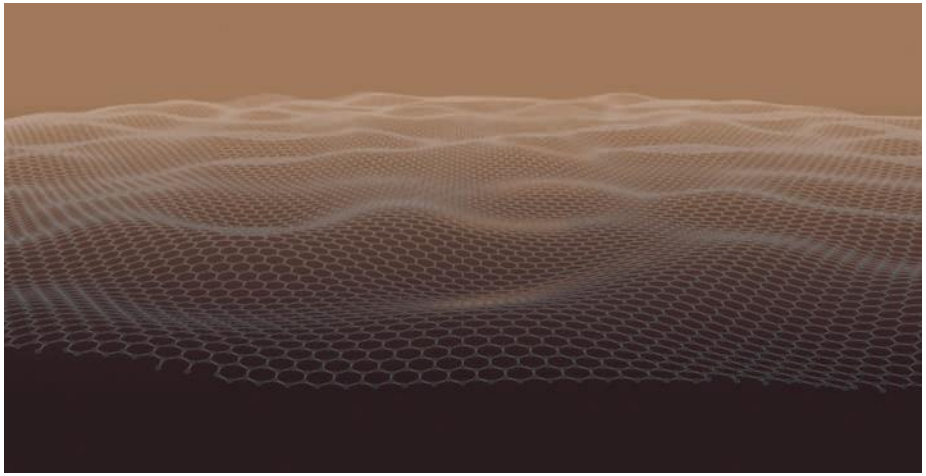

Prof. J. Raynien Kwo
Department of Physics,
National Tsing Hua University

Why the interest?

- **2D crystal with extraordinarily few defects**
- **Exotic electrical behaviors**
  - E = $\mathbf{v_F} \bullet \mathbf{P}$ (massless Dirac fermions)
  - Efficient tunneling through energy barrier, quantum Hall effects (QHE), …
- **Excellent materials properties**
  - Electrical -- high electron mobility, high current carrying capacity,…
  - Mechanical -- large Young's modulus, high tensile strength, low friction, …
  - Thermal -- high thermal conductivity
- **Excellent controllability**
  - Electrical gating, structural patterning, etc

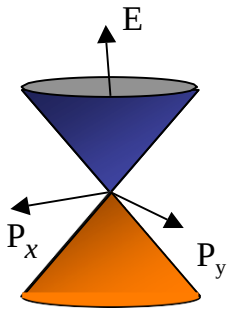

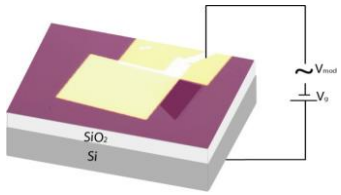

Attractive for fundamental physics and technological applications

Hot spots of graphene

Nobel Prize in Physics for 2010

"for groundbreaking experiments regarding the two-dimensional material graphene"

Andre Geim Konstantin Novoselov (2004)

www.graphene-flagship.eu

GRAPHENE FLAGSHIP

European Commission has chosen graphene as a ten-year, 1 billion euro Future Emerging Technology flagship. (Jan 28, 2013)

Aim to get graphene into industry and product development

http://www.graphene-flagship.eu/GF/index.php

SAMSUNG

SAMSUNG TECHWIN

The South Korean government has invested $200 million, beating the amount actually spent on graphene by the UK government, so far at least twenty times over. Samsung has added another $200million in South Korean spend.

http://www.cambridgenetwork.co.uk/news/is-the-uk-set-to-miss-out-on-the-graphene-revolution/

Graphene's Applications

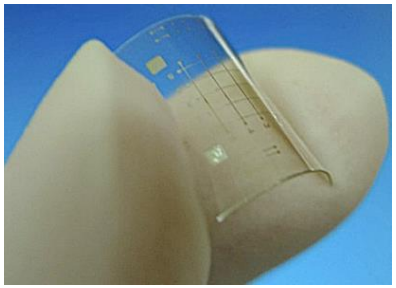

Flexible Memristors

Photo: Sung-Yool Choi
Nano Lett., ***10*** (11), 4381 (2010)

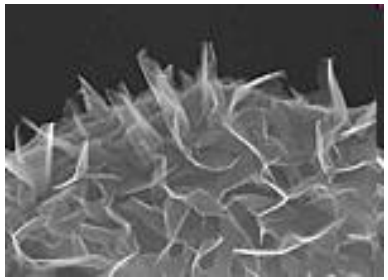

Ultracapacitor

Image: Ron Outlaw
Science **329** (5999) 1637 (2010)

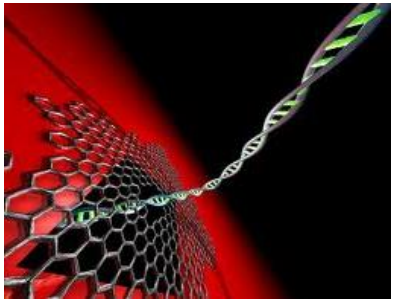

DNA graphene nanopore

Nano Lett., ***10*** (8), 3163 (2010)
Nano Lett.,, ***10*** (8), 2915 (2010)
Nature **467**, 190–193 (2010)

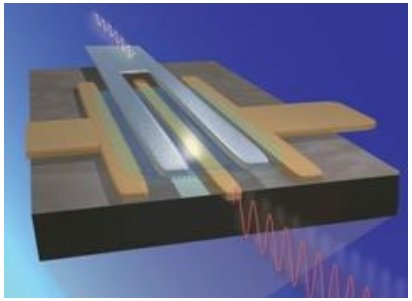

RF transistors

Nano Letters **9** (1), 422 (2009)
Nano Letters, **9** (12), 4474 (2009)
Science, **327**(5966), 662 (2010)
IEEE EDL, **31**(1), 68 (2010)
Nature **467**, 305–308 (2010)

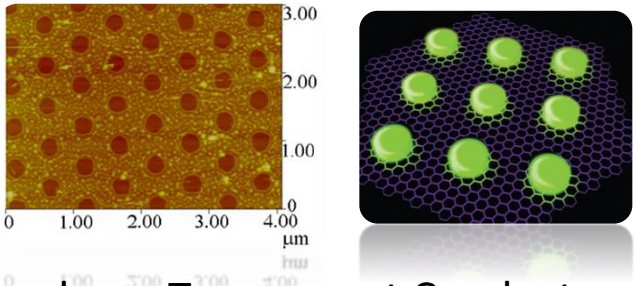

Graphene Transparent Conductors
APL **99**, 023111 (2011) and Adv. Mater. **24**, 71 (2012)

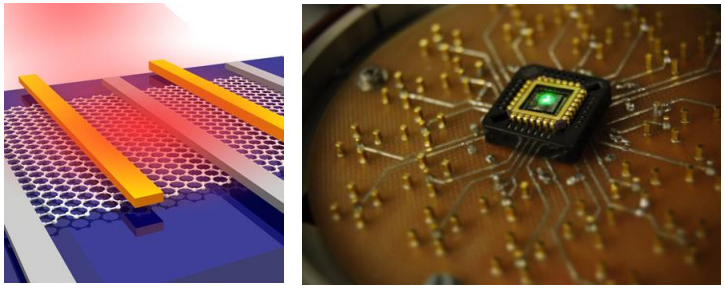

Graphene Photodetector
Nature Photonics **4**, 297 - 301 (2010)
Nature Nanotechnology **7**, 363–368 (2012)

Graphene Commercialization Breakthrough*

- OLED Lighting
- Transparent Conductors
- Logic & Memory
- Printed Electronics Manufacturing
- Catalytic support
- Stretchable and Sensing Electronics
- Solar Opportunities
- Energy Storage
- Advanced carbon based materials for Lithium Ion battery electrodes

*http://www.nanowerk.com/news2/newsid=27702.php

Fabrication of graphene

Method	Descriptions	Merits	References
Mechanical cleavage or exfoliation	Scotch Tape 	Minimal defects Intrinsic properties Small sizes	Science 306, 666 (2004)
Chemical oxidized process	Producing GO by the oxidation of graphite with acid	Large scale flakes Composite	Nature 442, 282 (2006)
Epitaxial growth on SiC	Epitaxial growing graphene on SiC	Large area Multilayer High temperature	J. Phys. Chem. B 108, 19912 (2004)
Chemical vapor deposition on Ni	Ambient-pressure CVD on evaporated polycrystalline Ni	Large area multilayer	Nano Lett., Vol. 9, No. 1, 200
Chemical vapor deposition on Cu	Growing graphene on Cu with methane and hydrogen.	Large area, one-layer Defect Mechanism	Science 324, 1312 (2009)
Solid carbon source to graphene	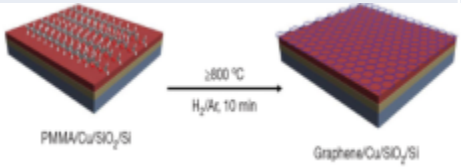	Poly (methyl methacrylate) One step to doped graphene	Nature, 468, 549 (2010)

Exfoliated Graphene Monolayers and Bilayers

Reflecting microscope images.

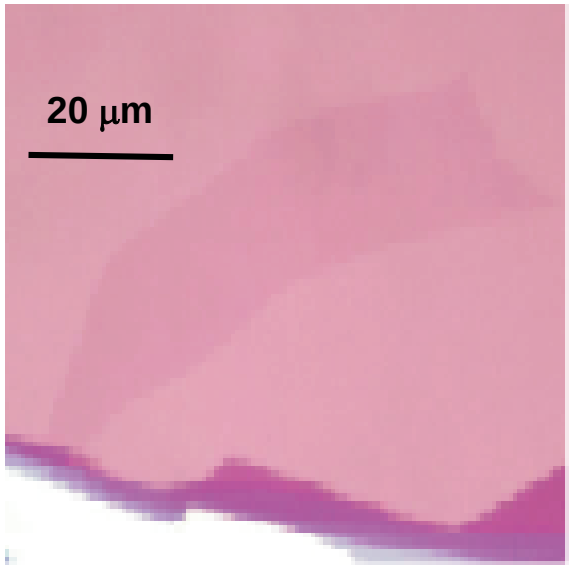

Monolayer

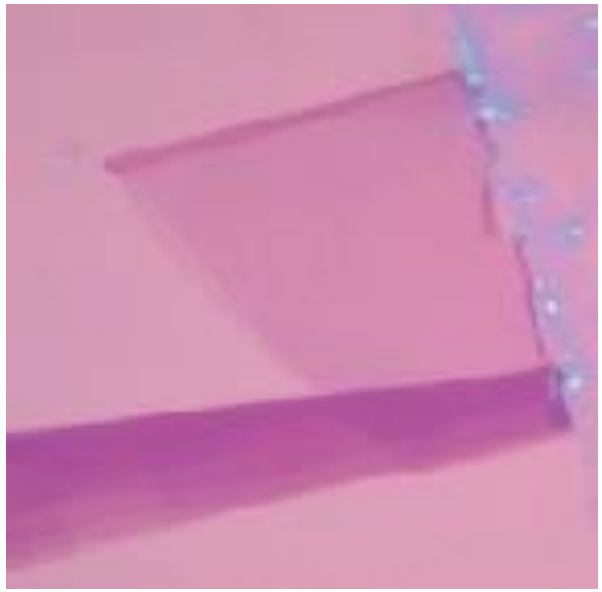

Bilayer

Graphene's unique optical properties produce an unexpectedly high opacity for an atomic monolayer in vacuum, absorbing $\pi\alpha \approx 2.3\%$ of red light, where α is the fine structure constant. This one-atom-thick crystal can be seen with the naked eye, because it absorbs approximately 2.6% of green light, and 2.3% of red light

K. S. Novoselov *et al.*, *Science* **306**, 666 (2004).

Epitaxial growth of graphene

Epitaxial graphene grown on SiC(0001) surfaces

One often ends up with multi-layers of graphene with small grains 30nm-200nm

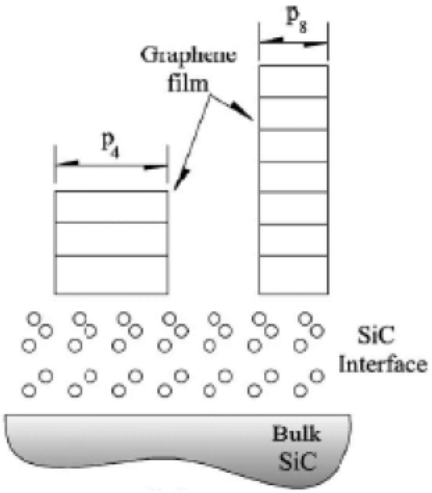

Recent progress:

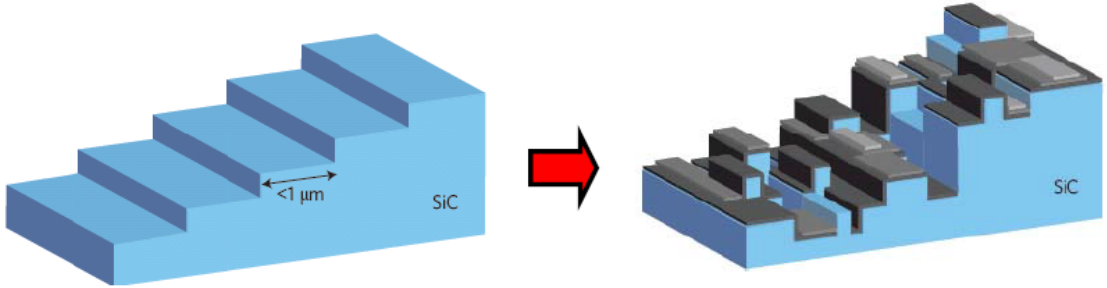

UHV

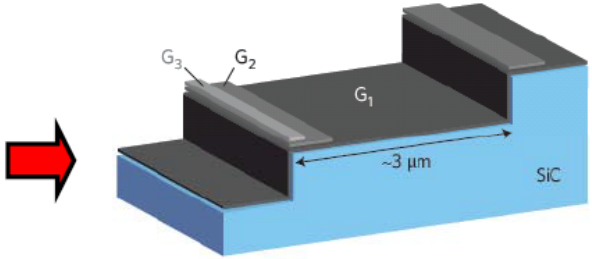

In the presence of pressurized Ar
K.V. Emvsev et al., Nature Materials 8, 203 (2009)

Vary Ar pressure to adjust the terrace size

CVD graphene on metal substrates

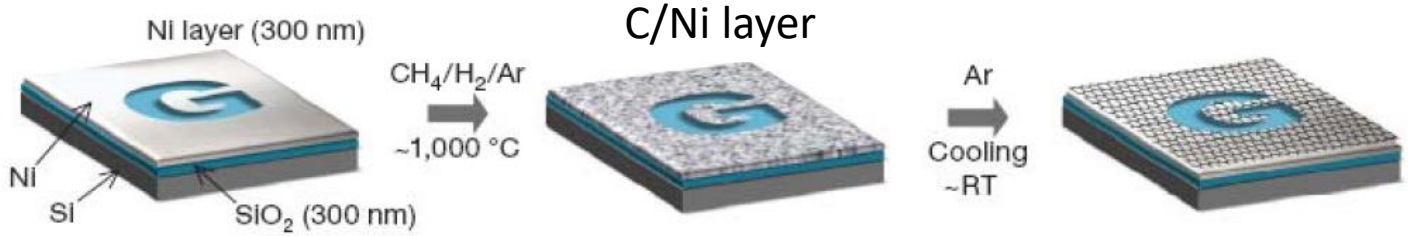

Etching and transfer

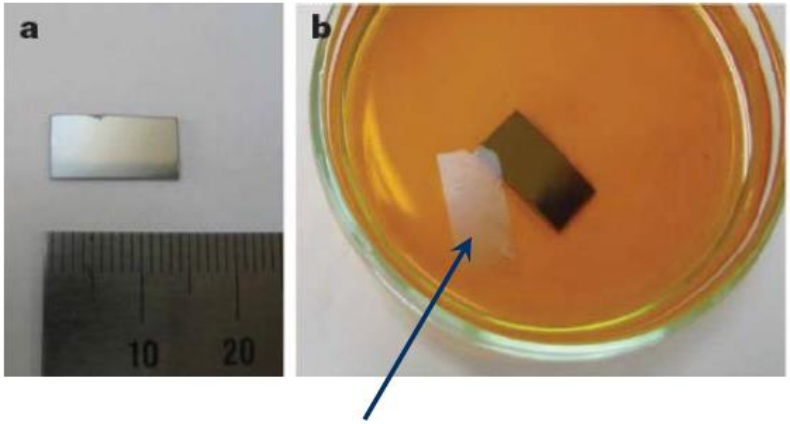

Floating graphene after Ni being etched
Ni: Kim et al., Nature 457, 706 (2009)

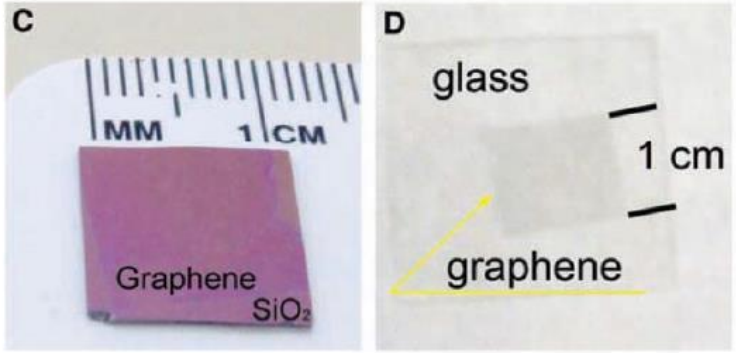

Cu: Li et al., Science 324, 1312 (2009)

Ripples of graphene on a SiO_2 substrate

"rippling" of the flat sheet, with amplitude ~1 nm

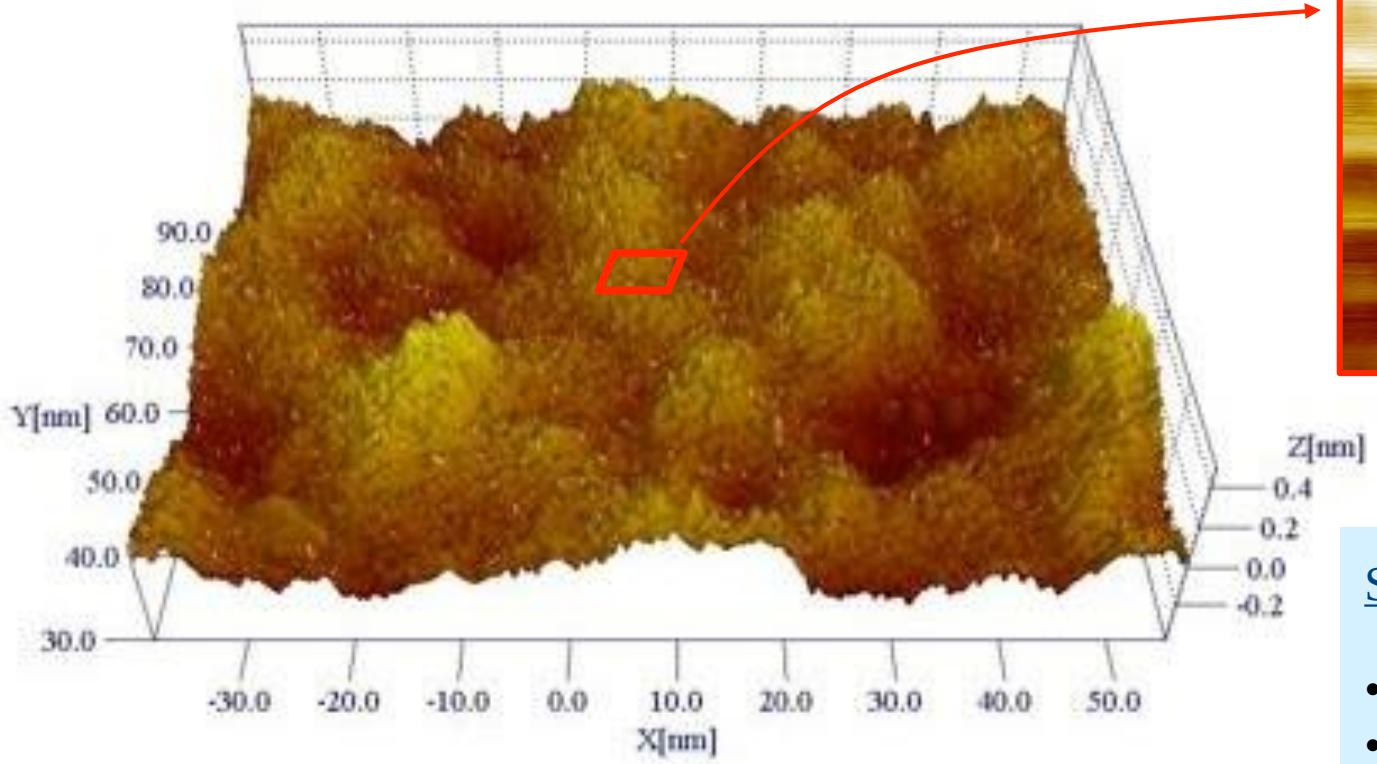

Atomic resolution

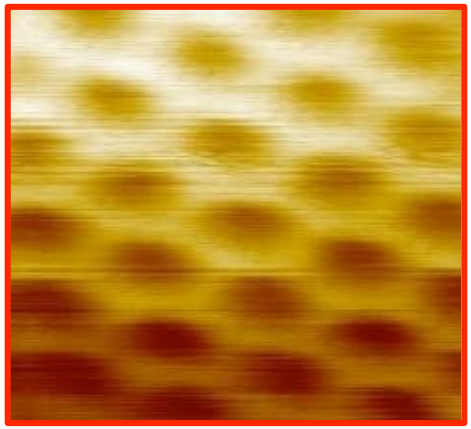

Scattering Mechanism?

- Ripples
- Substrate (charge trap)
- Absorption
- Structural defects

Elena Polyakova et al (Columbia Groups), PNAS (2007)

See also Meyer et al, Nature (2007) and Ishigami et al, Nano Letters (2007)

Extraordinary Properties of Graphene

- **Room-temperature electron mobility of 2.5×10^5 cm^2V^{-1} s^{-1}**

  Nano Lett. 11, 2396–2399 (2011).

- **Young's modulus of 1 TPa and intrinsic strength of 130 Gpa, the strongest materials ever tested.**

  Cu: 0.117 TPa Phys. Rev. B 76, 064120 (2007).

- **High thermal conductivity: above 3,000 $Wm^{-1}K^{-1}$**

  Cu: 401 $Wm^{-1}K^{-1}$ Nature Mater. 10, 569–581 (2011).

- **A prediction in 2015 suggested a melting point at least 5000 K.**

- **Optical absorption of 2.3%**

  Science 320, 1308 (2008).

- **No band gap for undoped graphene**

- **The electrical resistivity of graphene < 10^{-6} Ω·cm, less than silver, the lowest known at RT.**

Super-Qualities

★ m* = 0 expect huge mobility

Carrier mobility: 200000 $cm^2/V.s$

(Geim, 2008, 300K, $n \approx 10^{13} cm^{-2}$)

Ballistic transport at micronscale

Epitaxial graphene: 2000 $cm^2/V.s$ **(27K)** $\lambda_\phi \geq 1\mu m$

CVD graphene: 4050 $cm^2/V.s$ **(room temp)**

Si 1500 $cm^2/V.s$ **high speed GaAs 8500** $cm^2/V.s$

InSb (undoped) 77000 $cm^2/V.s$

★ Thermal conductivity (room temp)

$\approx 5 \times 10^3 Wm^{-1}K^{-1}$ ~ 10 × Cu or Al

$\mu = v/E$

$\sigma = ne\mu_e + ne\mu_h$

$\mu_e = e\,\tau_e/m_e$

$\mu_h = e\,\tau_h/m_h$

Exotic Behaviors

- **Klein's paradox**
- **Quantum Hall effect**
- **Berry Phase**
- **Ballistic transport**
- **Others**

Electron scattering from a potential barrier in applying the Dirac equation (1929)

Potential complication: Klein Paradox

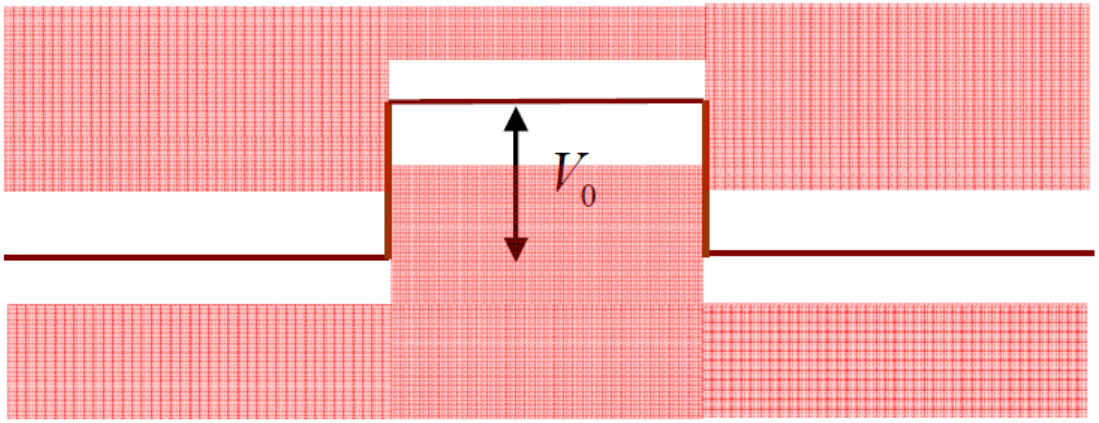

As $V_o \sim mC^2$, $T \rightarrow 1$, $R \rightarrow 0$

As the potential approaches infinity,
the reflection diminishes and the electron always transmits

No confinement for electrons

On/off ratio is reduced in graphene FET

Element of Carbon Network

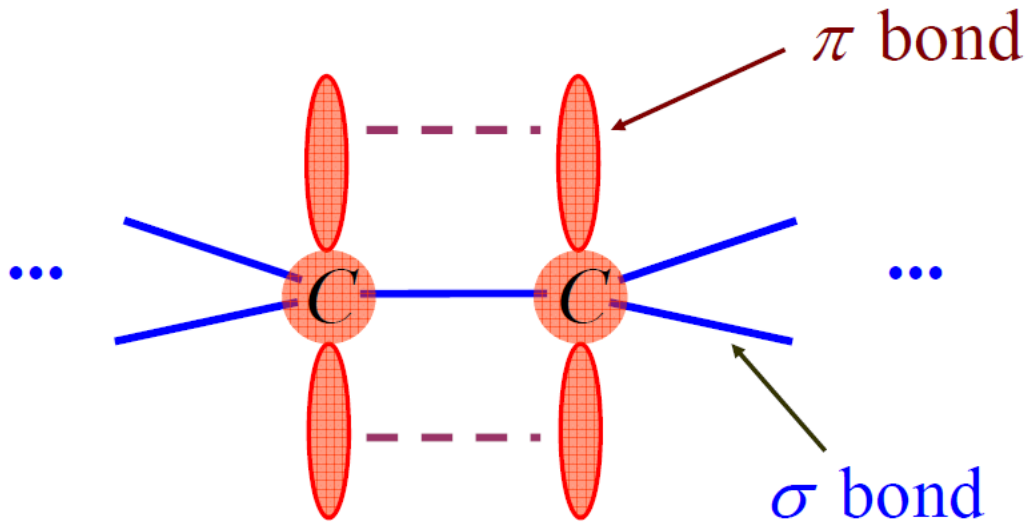

Carbon $1S^2\,\underbrace{2S^2\,2P^2}$

4 electrons in σ bonds (SP^2) + π bond or SP^3

(s, p_x, p_y orbitals) p_z orbital

Graphene and Related Carbon sp^2-bonded Structures

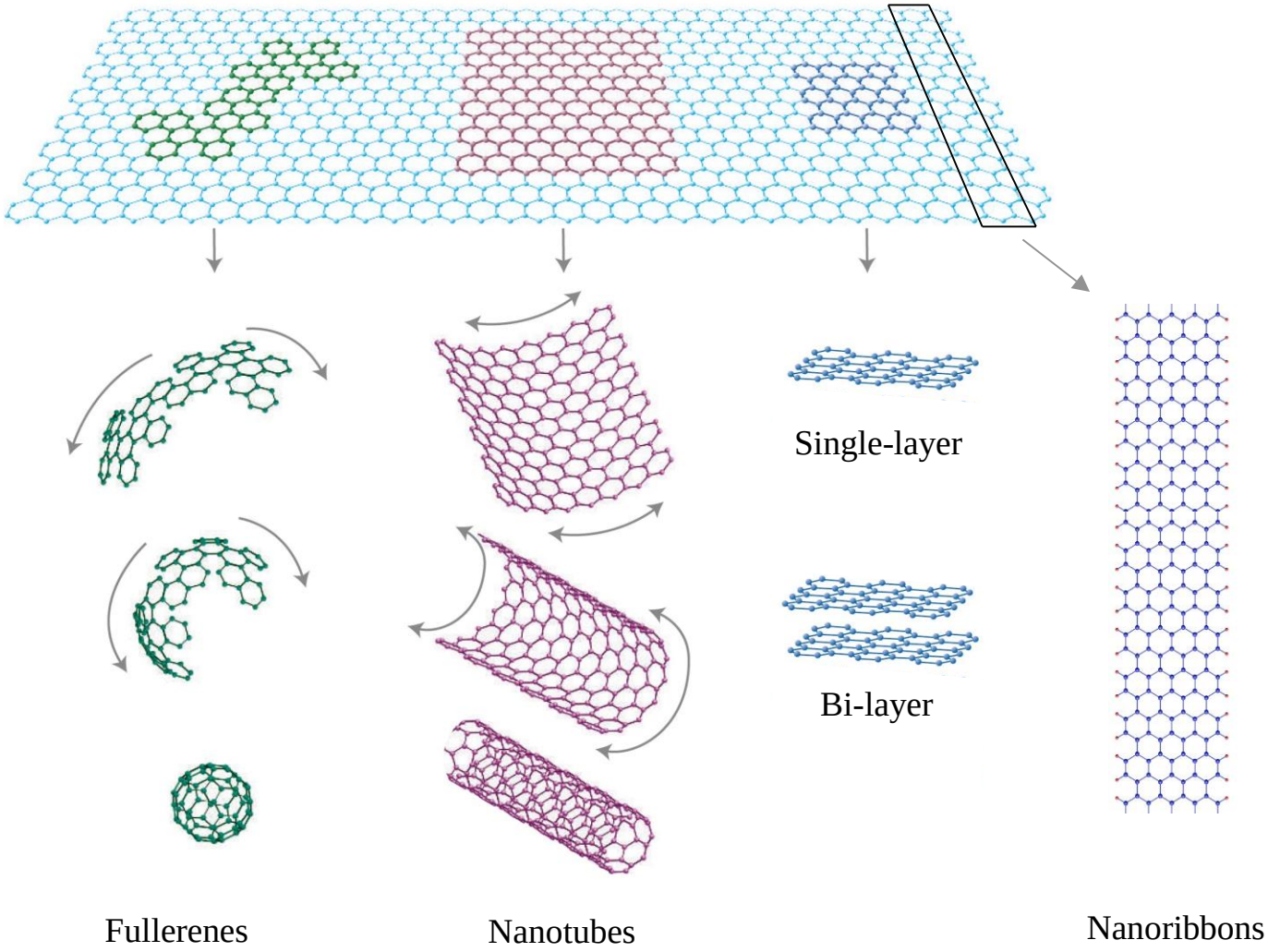

Honeycomb lattice and Brillouin zone of graphene

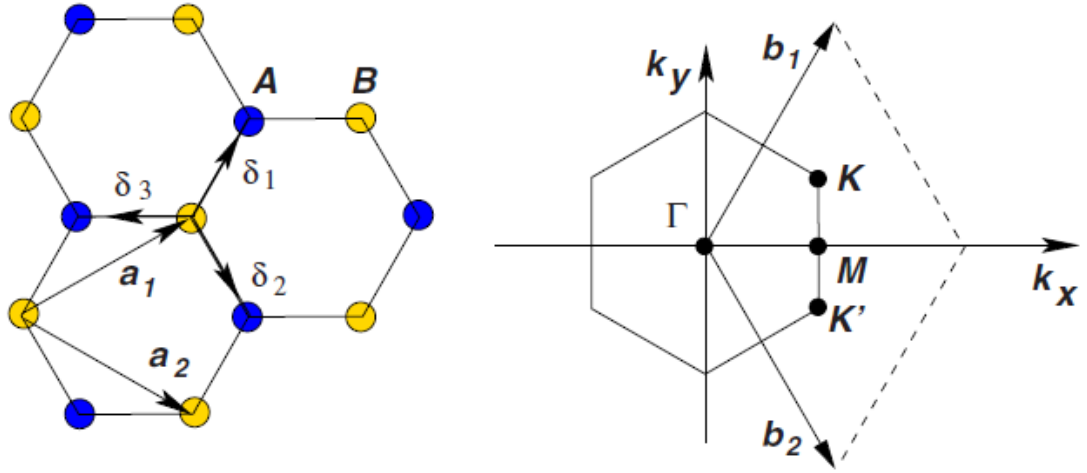

FIG. 2. (Color online) Honeycomb lattice and its Brillouin zone. Left: lattice structure of graphene, made out of two interpenetrating triangular lattices ($\boldsymbol{a}_1$ and $\boldsymbol{a}_2$ are the lattice unit vectors, and δ_i, $i=1,2,3$ are the nearest-neighbor vectors). Right: corresponding Brillouin zone. The Dirac cones are located at the K and K' points.

Graphene electronic structures

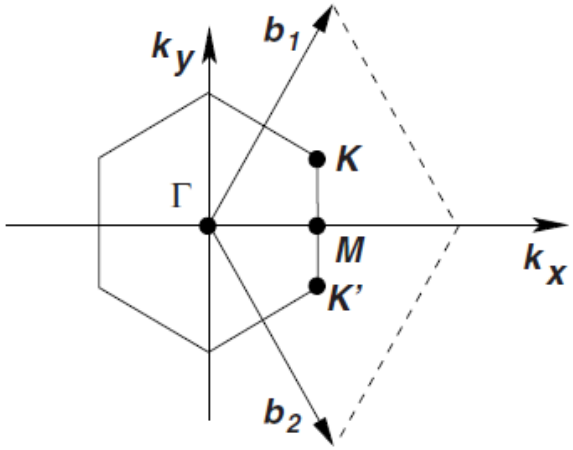

- The *E–K* relation is *linear* for low energies near the six corners of the 2-D hexagonal Brillouin zone, leading to zero effective mass for electrons and holes.
- Due to this linear dispersion relation at low energies, electrons and holes near these six points, the two adjacent ones, are inequivalent, behave like *relativistic* particles described by the Dirac equation for spin 1/2 particles.
- The electrons and holes are called Dirac Fermions, and the six corners of the Brillouin zone are called the Dirac points. The equation describing the *E–K* relation is $E = \hbar v_F \sqrt{k_x^2 + k_y^2}$, where the Fermi velocity v_F ~10^6 m/s.

Graphene : 2-D Massless Dirac Fermions

Band structure of graphene

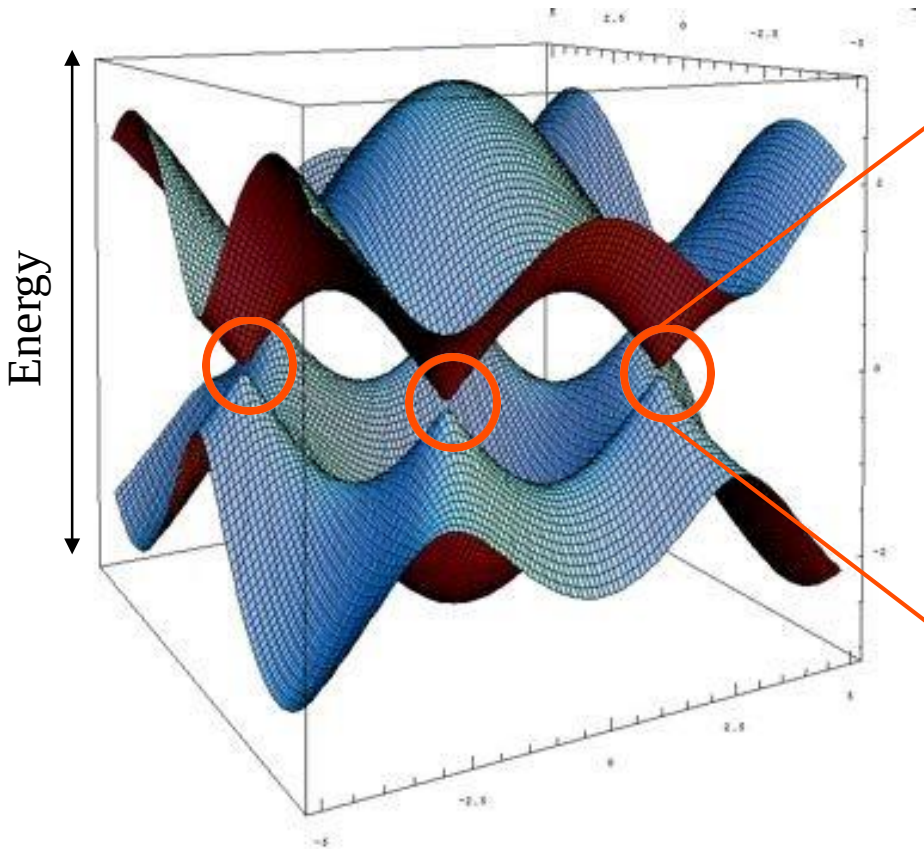

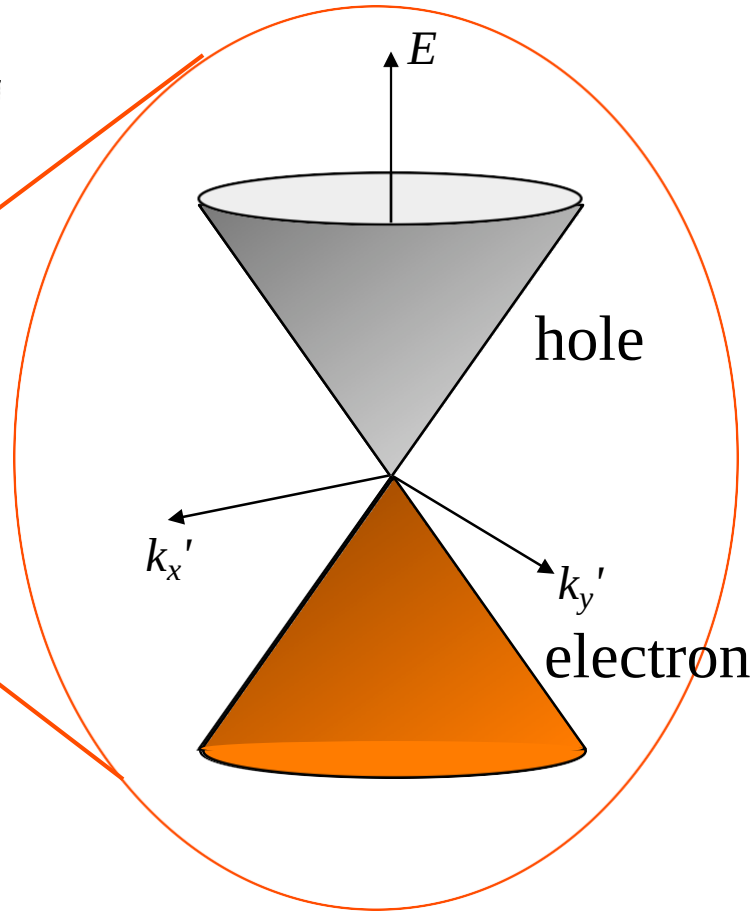

$$E \approx \hbar v_F \left| \vec{k}_\perp' \right|$$

Zero effective mass particles moving with a constant speed v_F

Quasi-Dirac Fermions

$E = \hbar \upsilon k$ with $m = 0$

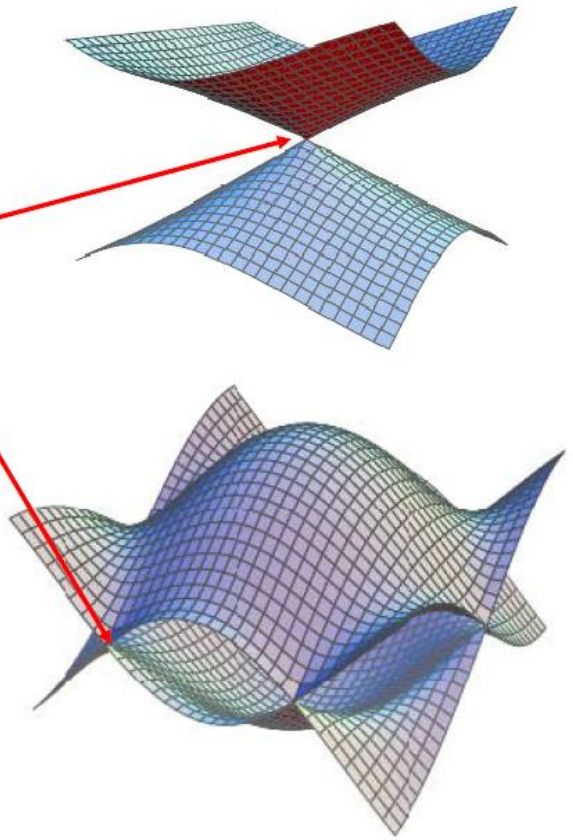

Dirac points

New playground for testing relativistic QM and QED!

Not exactly Dirac Fermions

$\upsilon \approx c/300$

$k_D \neq 0$ and inter-Dirac point scatterings!

Graphene

Single layer of graphite
Two carbon atoms per unit cell
in a honeycomb structure

For a nanoribbon, in zig-zag orientation, always metallic, with zero bandgap

In arm chair, semiconducting or metallic, with nonzero bandgap

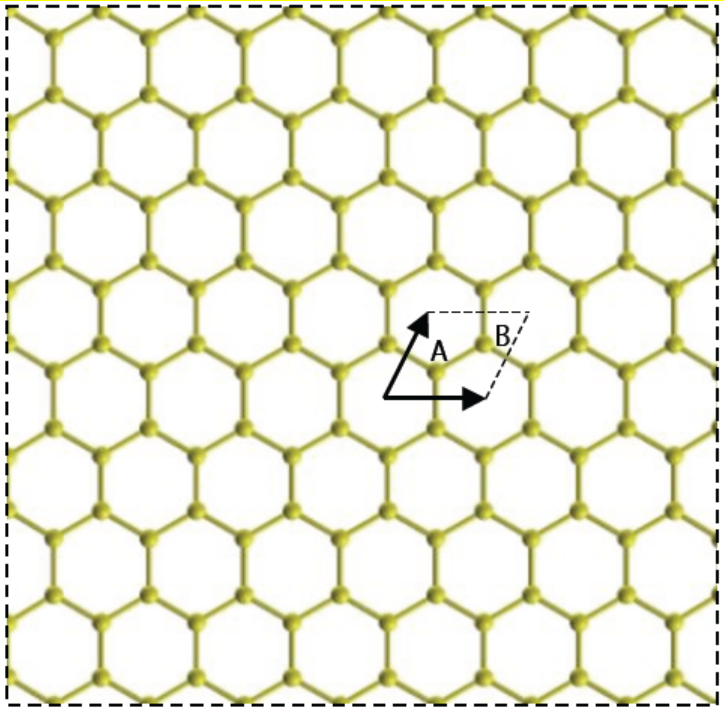

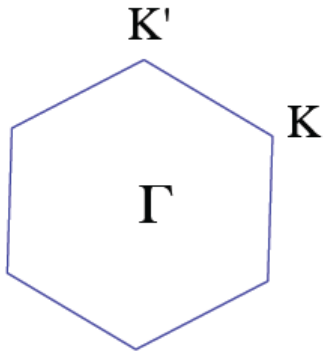

Brillouin zone

The **quantum Hall effect** is a quantum mechanical version of the Hall effect, which is the production of transverse (perpendicular to the main current) conductivity in the presence of a magnetic field. The quantization of the Hall effect σ_{xy} at integer multiples (the "Landau level") of the basic quantity e^2/h (where e is the elementary electric charge and h is Planck's constant). $\sigma_{xy} = \pm N e^2/h$. It can usually be observed only in very clean silicon or gallium arsenide solids at temperatures around 3 K and high magnetic fields.

Graphene shows the quantum Hall effect with respect to conductivity quantization: the effect is anomalous in that the sequence of steps is shifted by **1/2** with respect to the standard sequence and with an additional factor of **4**. Graphene's Hall conductivity is $\sigma_{xy} = \pm 4 \cdot (N + 1 / 2) e^2/h$, where N is the Landau level and the double valley and double spin degeneracies give the factor of 4. These anomalies are present at room temperature, i.e. at roughly 20 °C (293 K).

This behavior is a direct result of graphene's **massless Dirac electrons**. In a magnetic field, their spectrum has a Landau level with energy precisely at the Dirac point. This level is a consequence of the **Atiyah–Singer index theorem** and is half-filled in neutral graphene, leading to the "+1/2" in the Hall conductivity. **Bilayer graphene** also shows the quantum Hall effect, but with only one of the two anomalies, i.e. $\sigma_{xy} = \pm 4 \cdot N \cdot e^2/h$. In the second anomaly, the first plateau at N=0 is absent, indicating that bilayer graphene stays metallic at the neutrality point.

Unlike normal metals, graphene's longitudinal resistance shows maxima rather than minima for integral values of the Landau filling factor in measurements of the Shubnikov–de Haas oscillations, whereby the term integral quantum Hall effect. **These oscillations show a phase shift of π, known as Berry's phase.** Berry's phase arises due to the zero effective carrier mass near the Dirac points. The temperature dependence of the oscillations reveals that the carriers have a non-zero cyclotron mass, despite their zero effective mass.

Transport Single Layer Graphene

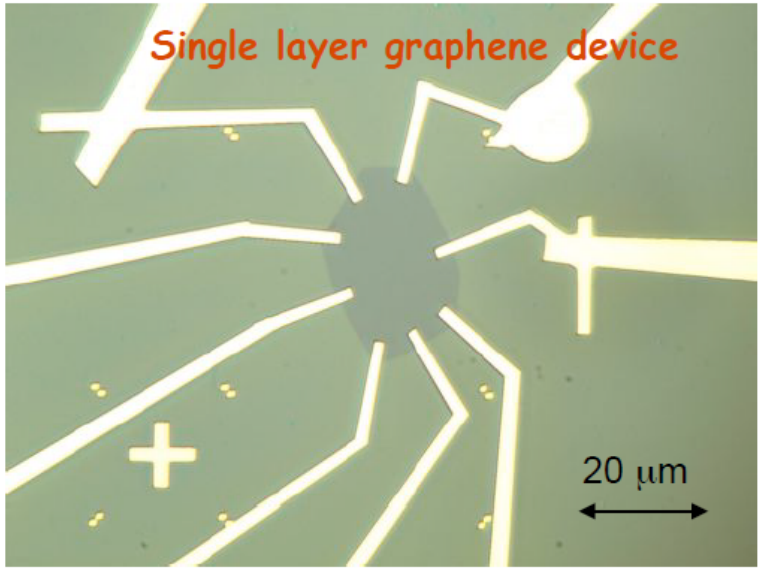

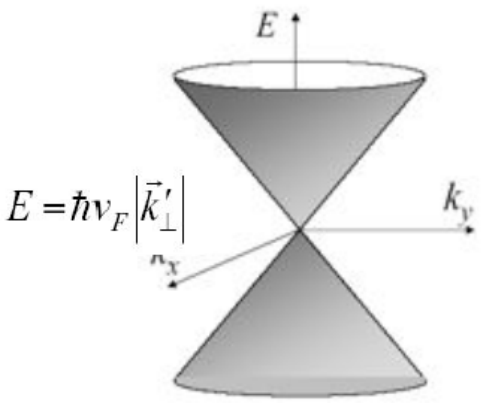

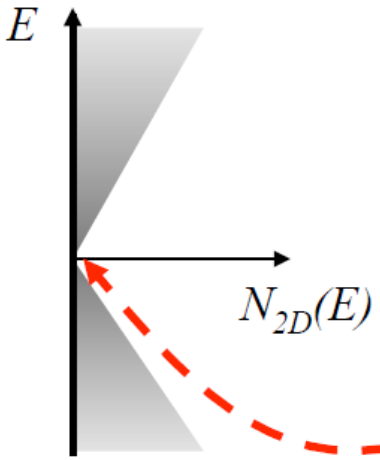

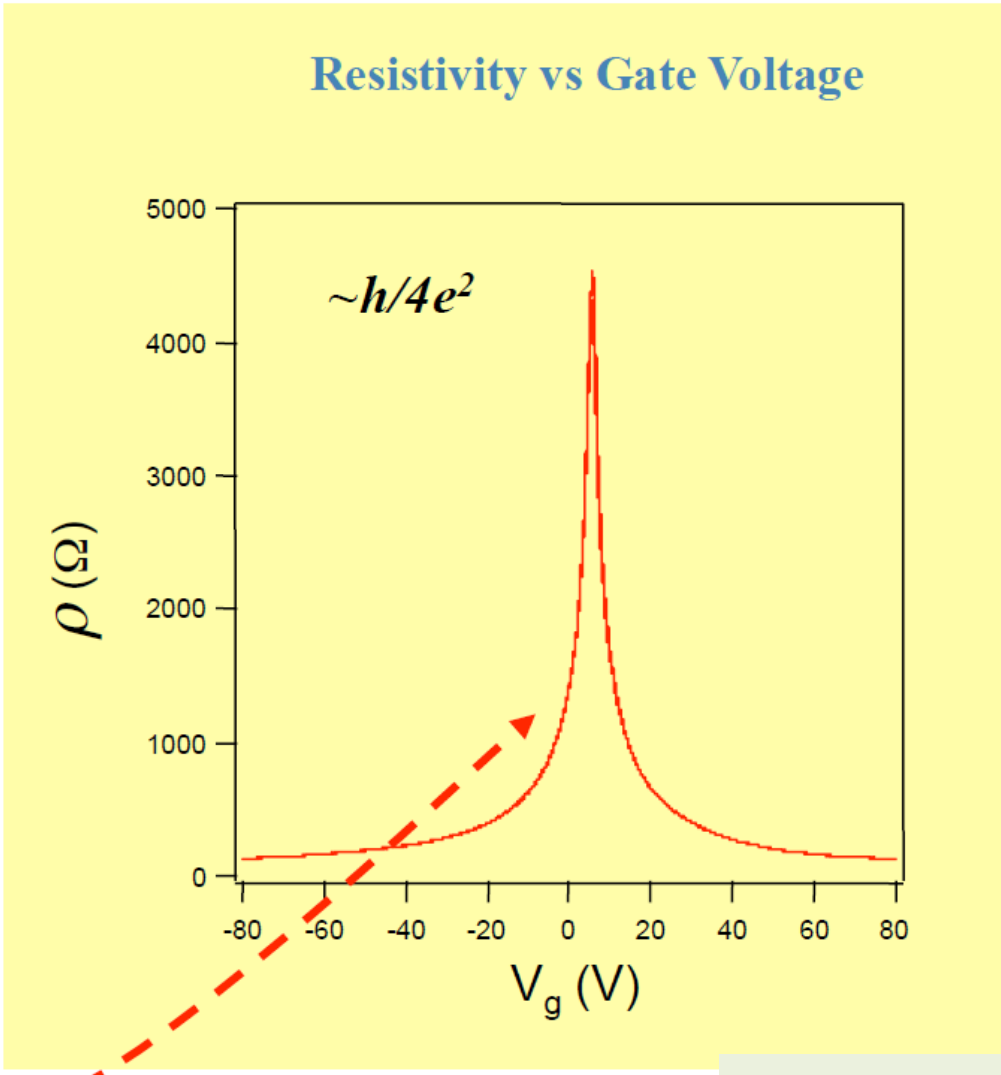

$$\rho^{-1} = e^2 v_F \, l_e \, N_{2D}$$

P. Kim et al , Nature (2005)

Quantum Hall Effect in Graphene

T = 4K, B= 14T

2-layer graphene: Integer

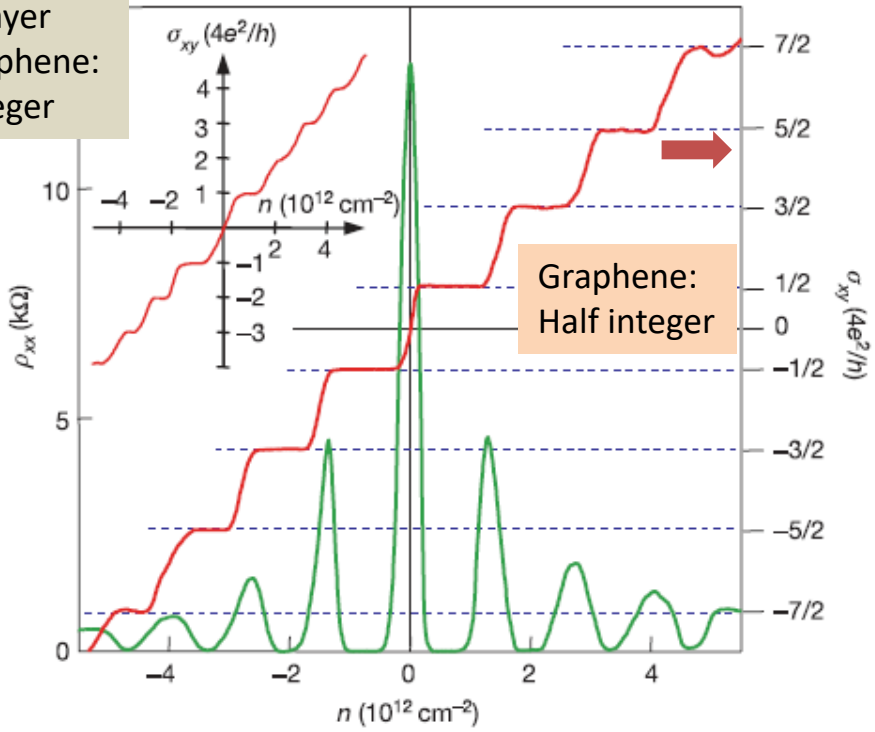

Figure 4 | QHE for massless Dirac fermions. Hall conductivity σ_{xy} and longitudinal resistivity ρ_{xx} of graphene as a function of their concentration at $B = 14$ T and $T = 4$ K. $\sigma_{xy} \equiv (4e^2/h)\nu$ is calculated from the measured dependences of $\rho_{xy}(V_g)$ and $\rho_{xx}(V_g)$ as $\sigma_{xy} = \rho_{xy}/(\rho_{xy}^2 + \rho_{xx}^2)$. The behaviour of $1/\rho_{xy}$ is similar but exhibits a discontinuity at $V_g \approx 0$, which is avoided by plotting σ_{xy}. Inset: σ_{xy} in 'two-layer graphene' where the quantization sequence is normal and occurs at integer ν. The latter shows that the half-integer QHE is exclusive to 'ideal' graphene.

Novoselov et al, Nature, 438, 197, (2005)
Zhang et al, Nature, 438, 201, (2005)

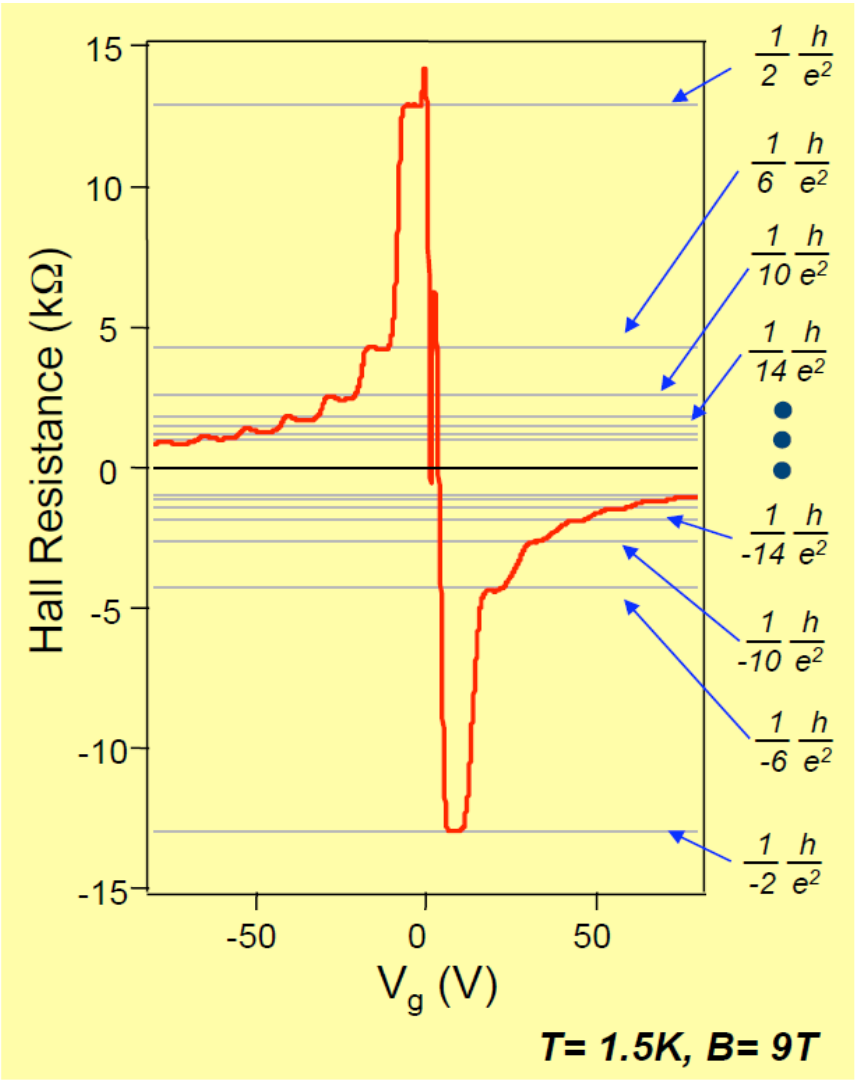

Quantization:

$$R_{xy}^{-1} = 4\left(n + \frac{1}{2}\right)\frac{e^2}{h}$$

Room Temperature Quantum Hall Effect

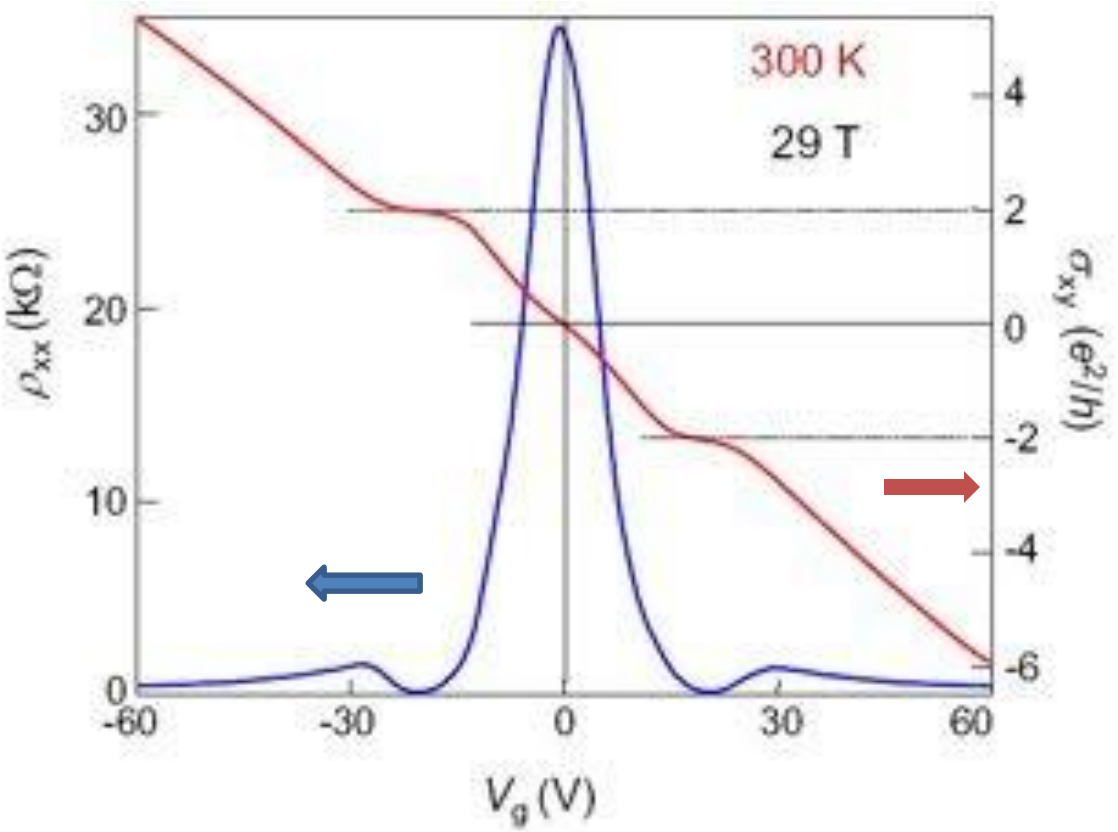

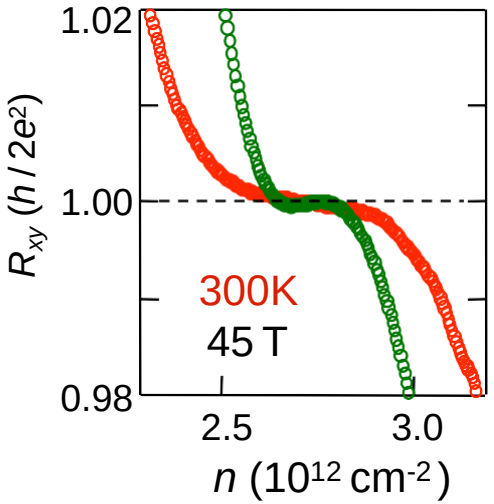

Deviation < 0.3%

$$E_n = \pm\sqrt{2e\hbar v_F^2 |n| B}$$

$E_1 \sim 100$ meV @ 5 T

Novoselov, Jiang, Zhang, Morozov, Stormer, Zeitler, Maan, Boebinger, Kim, and Geim, *Science* (2007)

Graphene Mobility

GaAs HEMT

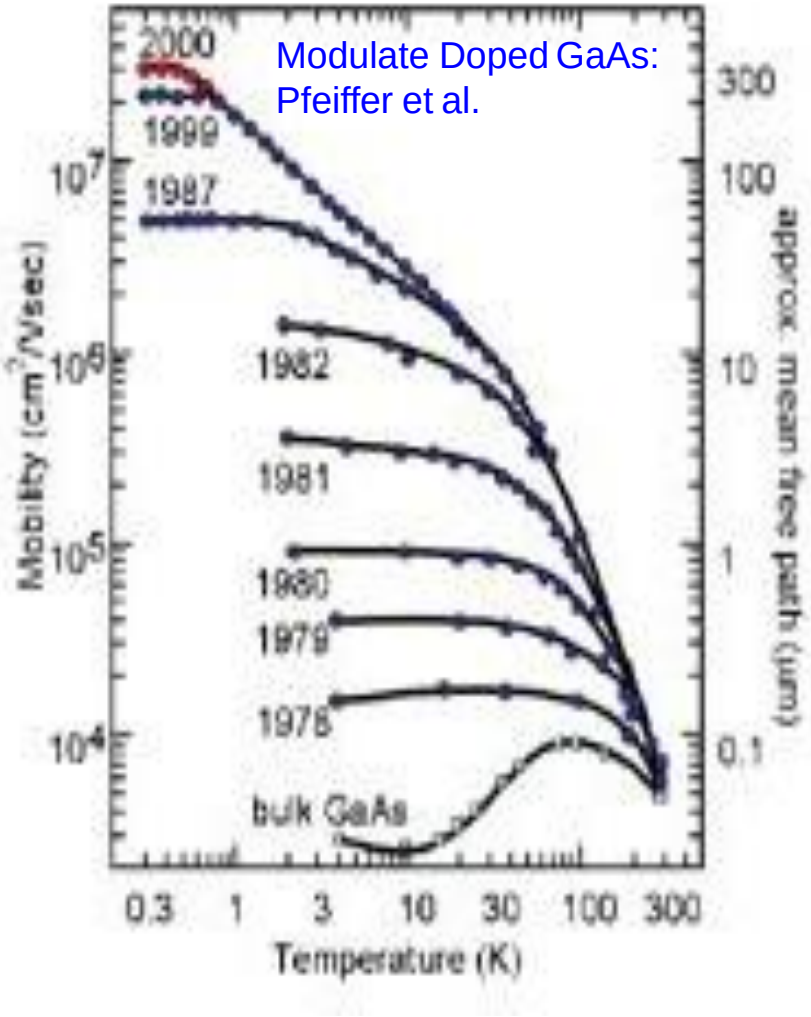

Graphene Mobility

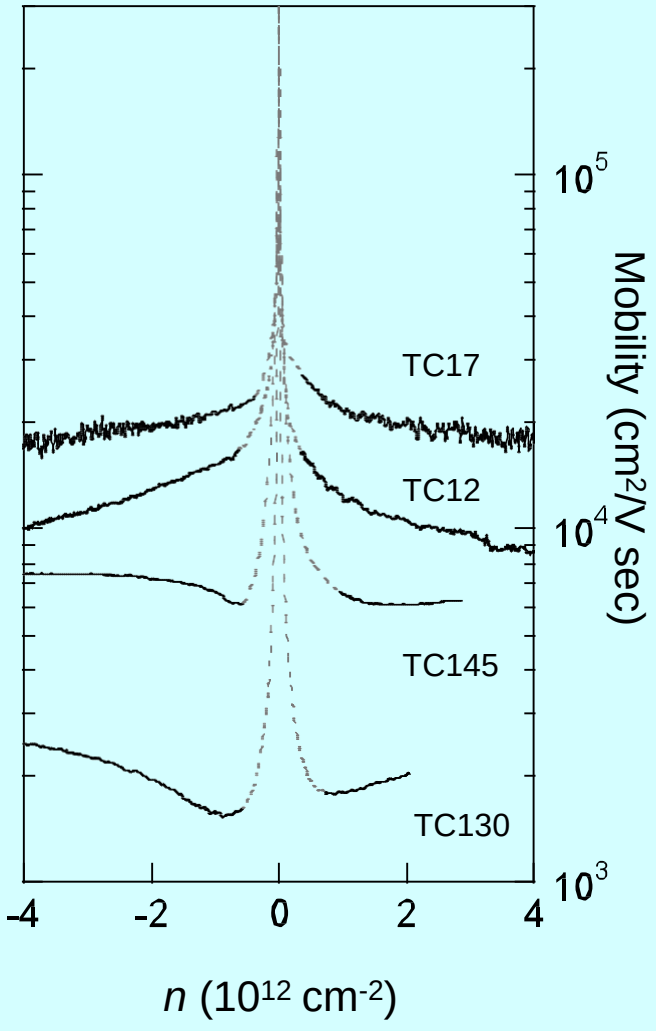

Tan al. PRL (2007)

Conductivity, Mobility, & Mean Free Path

$$\sigma = en\mu = \frac{e^2}{\hbar}\ell\sqrt{\frac{n}{\pi}}$$

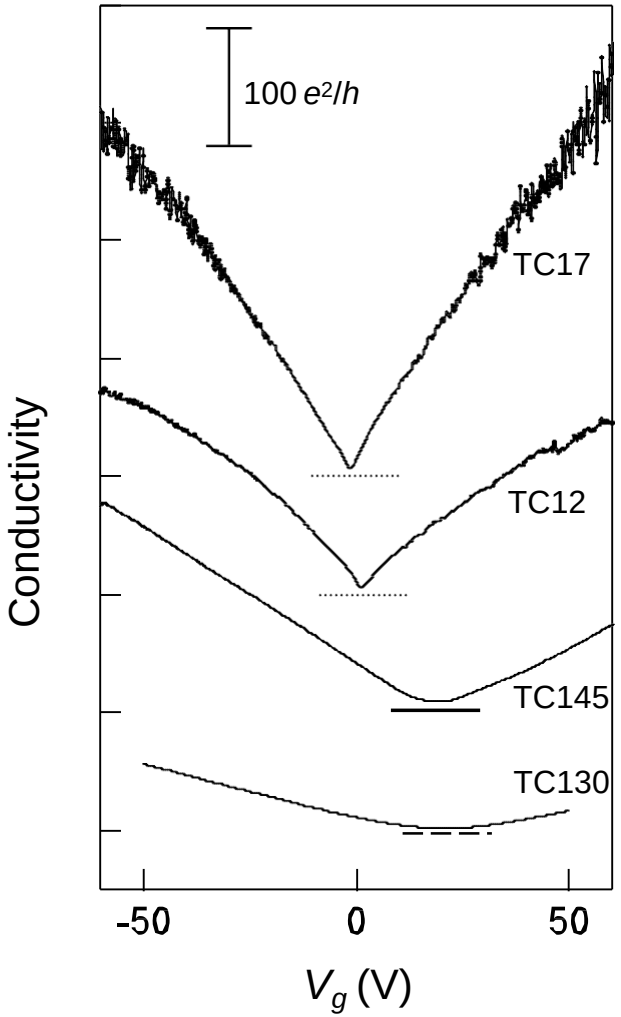

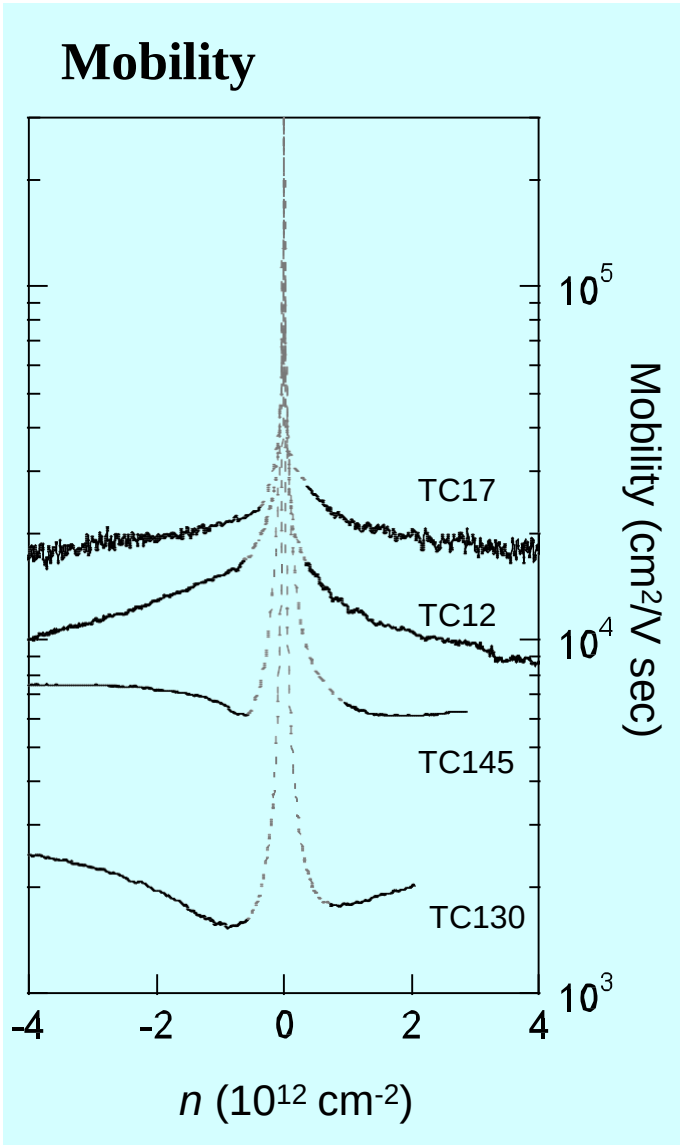

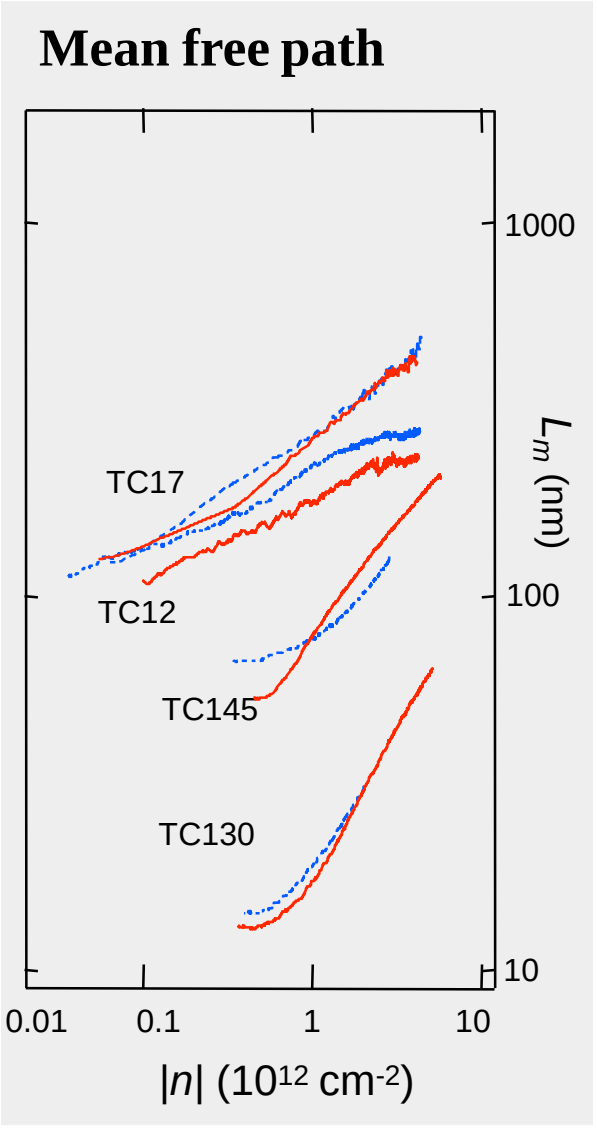

Spin transport

- Graphene is claimed to be an ideal material for spintronics due to its small spin orbit interaction and the near absence of nuclear magnetic moment in carbon.
- Electrical spin current injection and detection has been demonstrated up to room temperature.
- Spin coherence length λ over 1 μm at room temperature was observed, and control of the spin current polarity with an electrical gate was observed at low temperature.
- Spintronic and magnetic properties can be present in graphene simultaneously.

Toward High Mobility: Suspending Samples

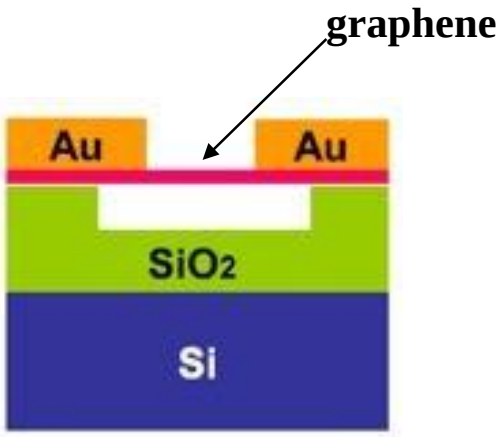

HF etching
-> critical pointing drying

SEM image of suspended graphene

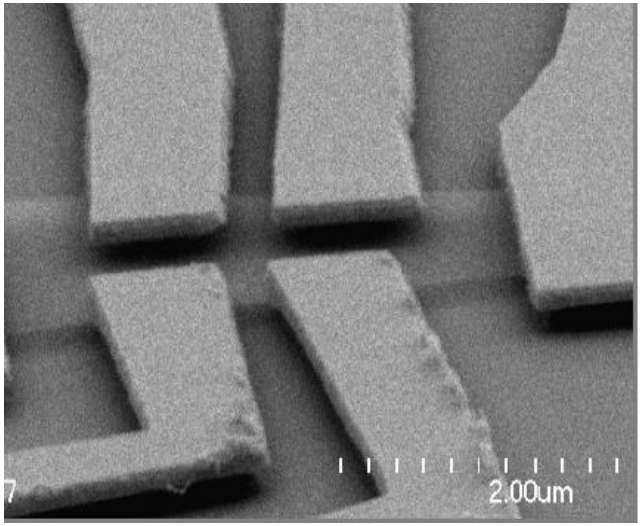

AFM image of suspended graphene

You should not apply to high gate voltage, otherwise…

Collapsed graphene devices…

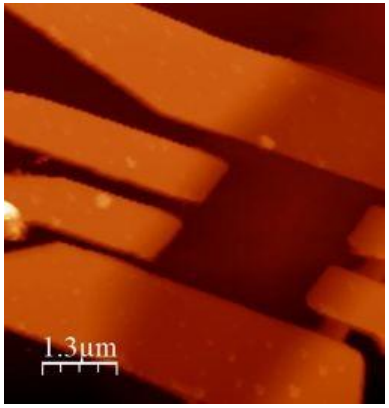

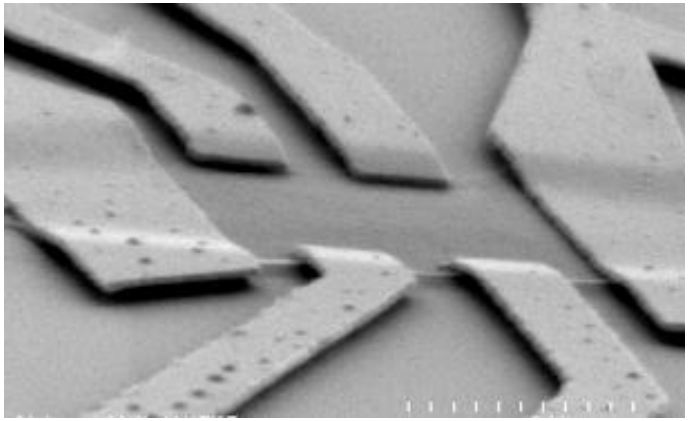

Graphene Electronics

Engineer Dreams

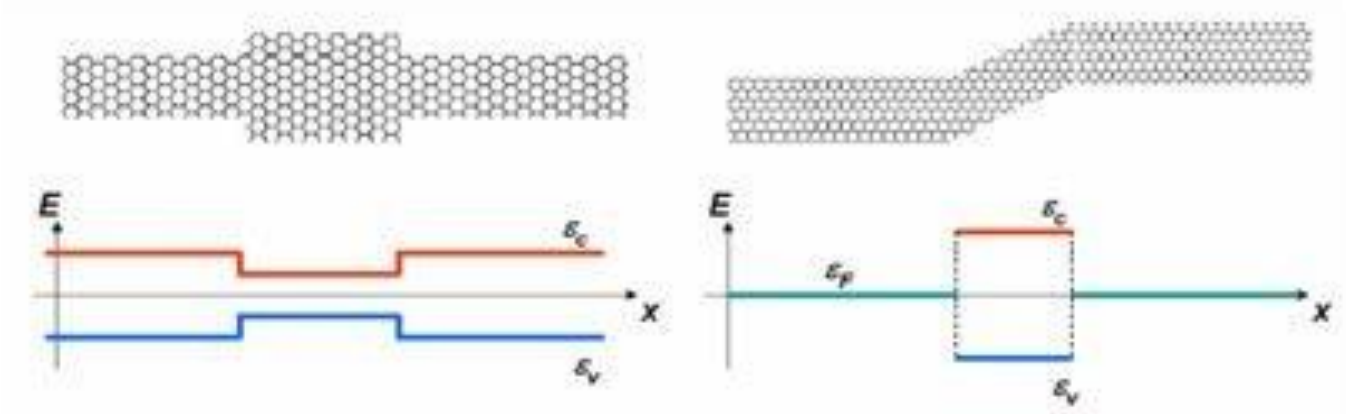

Theorist Dreams

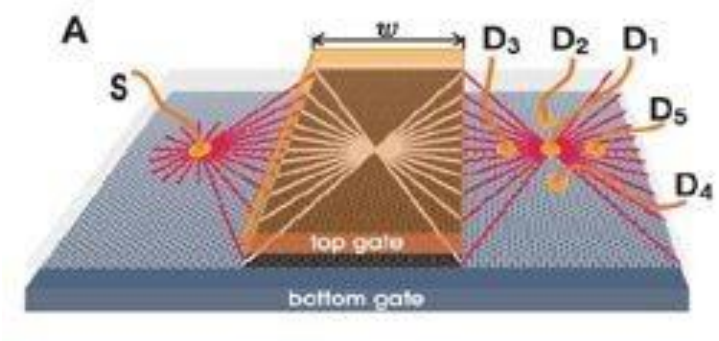

Graphene Veselago lense

Cheianov *et al. Science* (07)

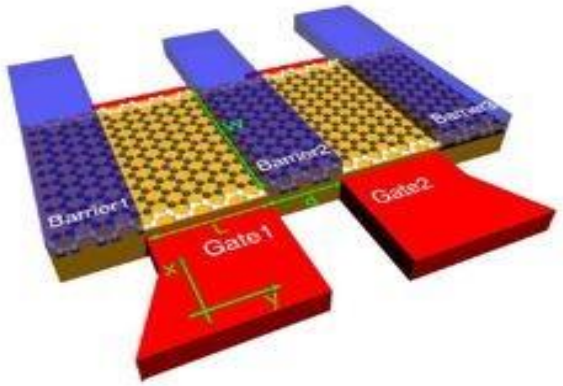

Graphene q-bits

Trauzettel *et al. Nature Phys.* (07)

and
more …

The Focusing of Electron Flow and a Veselago Lens in Graphene *p-n* Junctions

Science, VOL 315, 1252 (2007)

The focusing of electric current by a single *p-n* junction in graphene is theoretically predicted, as achieved by fine-tuning the densities of carriers on the *n*- and *p*-sides of the junction to equal values. This finding is useful for the engineering of electronic lenses and focused beam splitters using gate-controlled *n-p-n* junctions in graphene-based transistors.

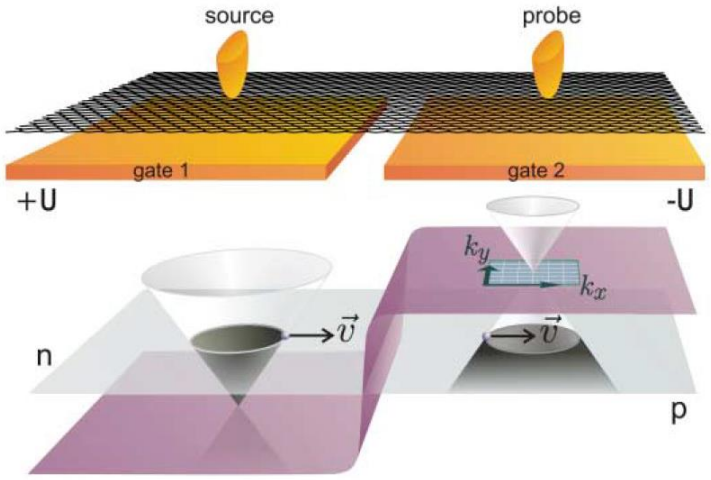

Fig. 1. Graphene *p-n* junction (PNJ). Monolayer of graphite is placed over the split gate, which is used to create *n*- (**left**) and *p*-doped (**right**) regions. The energy diagram shows the position of the Fermi level with respect to the touching point of the valence and the conduction bands.

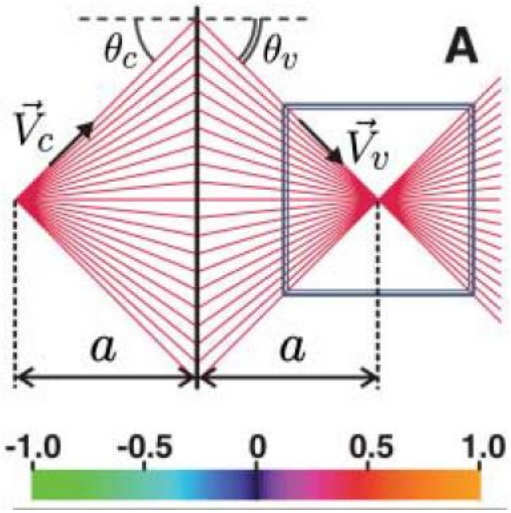

Fig. 2. Focusing of electrons by symmetric PNJ, $\rho_h = \rho_e$. (**A**) Classical trajectories of electrons diverging from a source at distance *a* from the junction become convergent after refraction. (**B**)

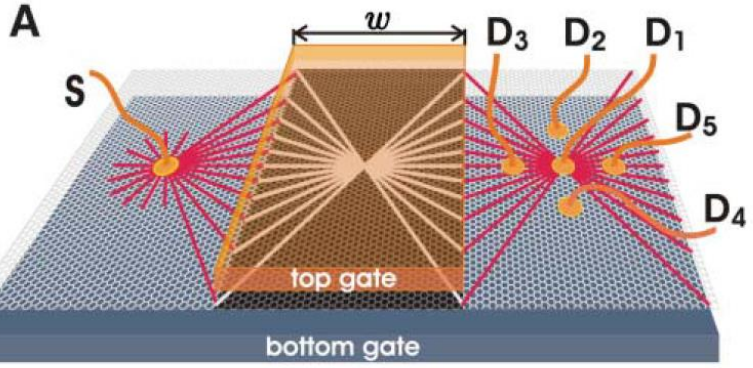

Fig. 4. (**A**) Electron Veselago lens and (**B** and **C**) prism-shaped focusing beam splitter in the ballistic *n-p-n* junction in graphene-based transistor.

From Graphene “Samples” To Graphene “Devices”

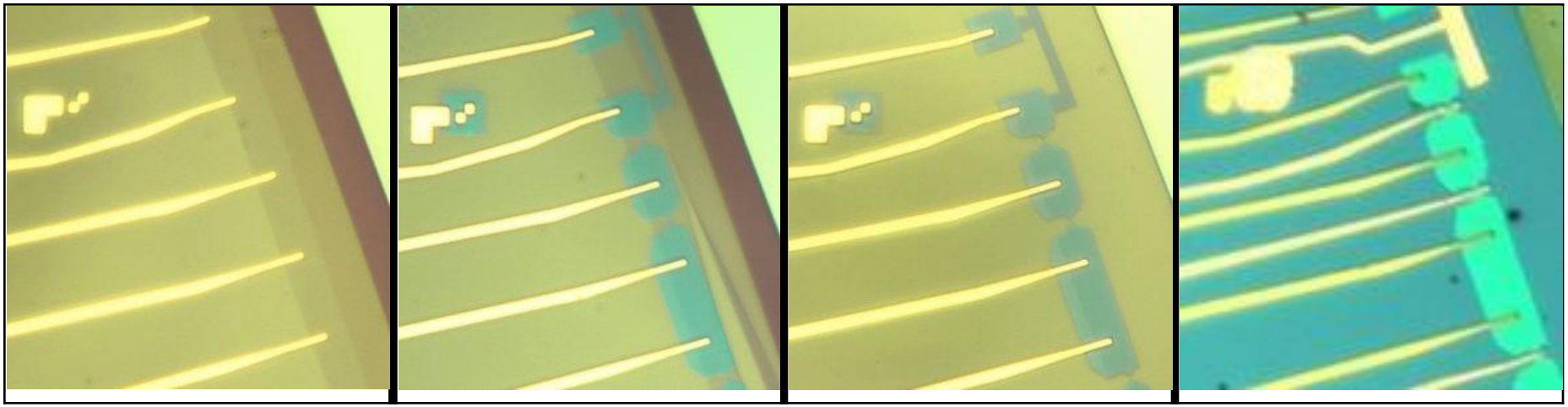

Contacts :	**Graphene patterning**:	**Graphene etching:**	**Local gates:**
PMMA EBL Evaporation	HSQ EBL Development	Oxygen plasma	ALD HfO_2 EBL Evaporation

Graphene Nanoribbons: Confined Dirac Particles

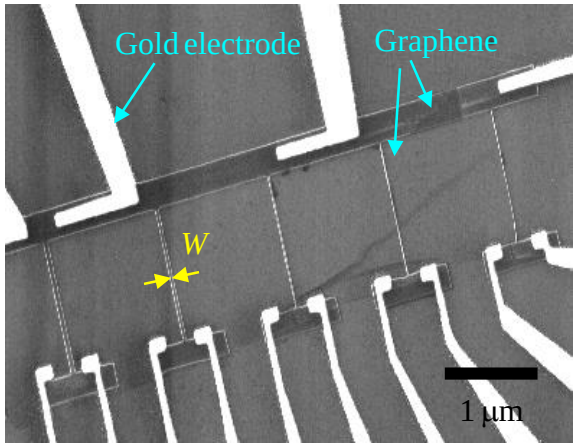

10 nm < *W* < 100 nm

Dirac Particle Confinement

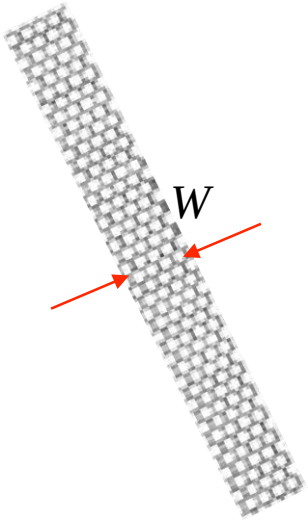

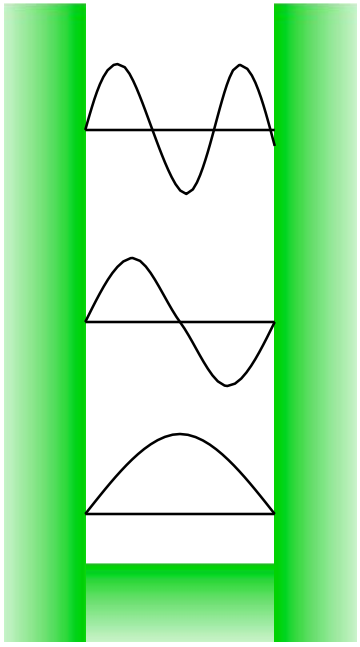

$$k_3 = \frac{3 \cdot \pi}{W}$$

$$k_2 = \frac{2 \cdot \pi}{W}$$

$$k_1 = \frac{1 \cdot \pi}{W}$$

$$\Delta k - \frac{\pi}{W}$$

Graphene nanoribbon theory partial list

K. Nakada, M. Fujita, G. Dresselhaus, M. S. Dresselhaus, Phys. Rev. B **54**, 17954 (1996).
K. Wakabayashi, M. Fujita, H. Ajiki, M. Sigrist, Phys. Rev. B **59**, 8271 (1999).
Y. Miyamoto, K. Nakada, M. Fujita, Phys. Rev. B **59**, 9858 (1999).
M. Ezawa, Phys. Rev. B **73**, 045432 (2006).
N. M. R. Peres, A. H. Castro Neto, and F. Guinea, Phys. Rev. B **73**, 195411 (2006)
L. Brey and H. A. Fertig, Phys. Rev. B **73**, 235411 (2006).
Y. Ouyang, Y. Yoon, J. K. Fodor, and J. Guo, Appl. Phys. Lett. **89**, 203107 (2006).
Y.-W. Son, M. L. Cohen, S. G. Louie, Nature **444**, 347 (2006)
Y.-W. Son, M. L. Cohen, S. G. Louie, Phys. Rev. Lett. **97**, 216803 (2006).
V. Barone, O. Hod, G. E. Scuseria, Nano Lett **6** 2748 (2006).
D. A. Areshkin, D. Gunlycke, C. T. White, Nano Lett. **7**, 204 (2007).

• • •

$$E_{gap} \sim \hbar v_F * k \sim h v_F / W$$

Graphene Ribbon Devices

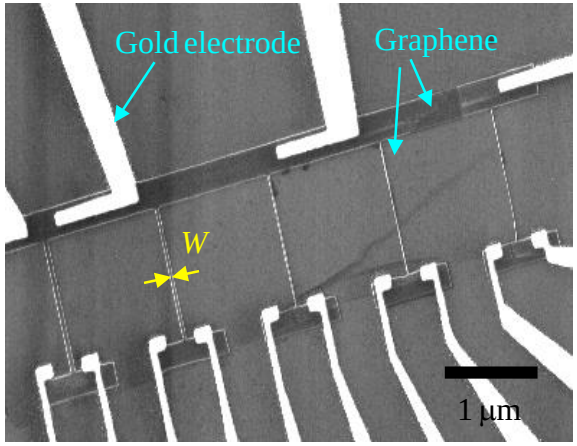

10 nm < *W* < 100 nm

Dirac Particle Confinement

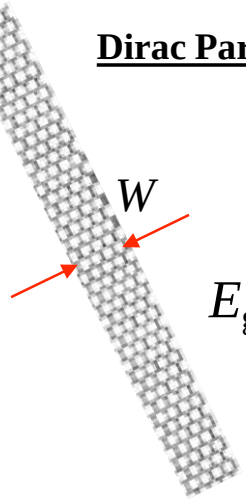

$E_{gap} \sim \hbar v_F / W$

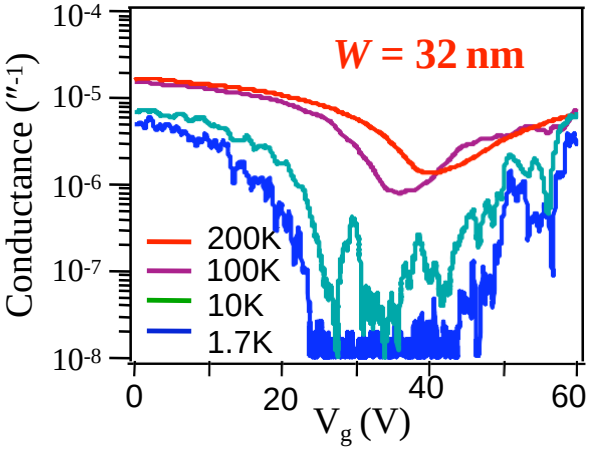

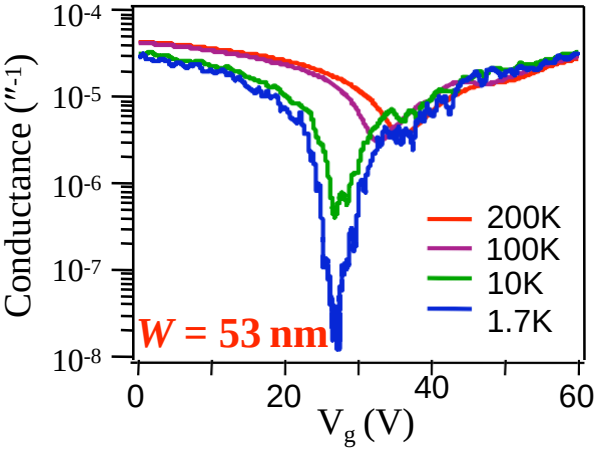

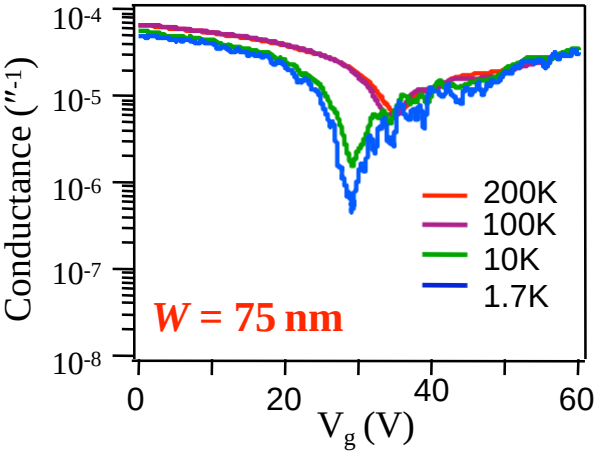

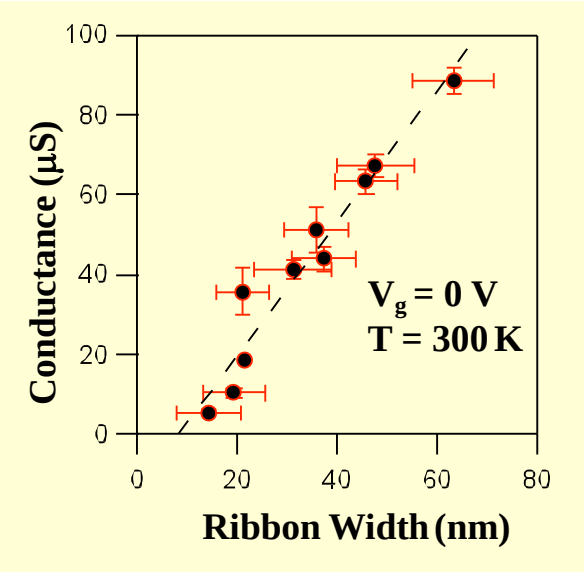

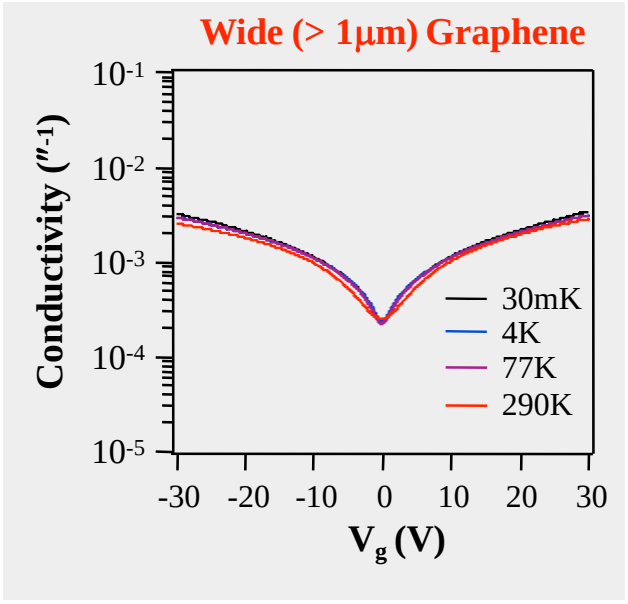

Scaling of Energy Gaps in Graphene Nanoribbons

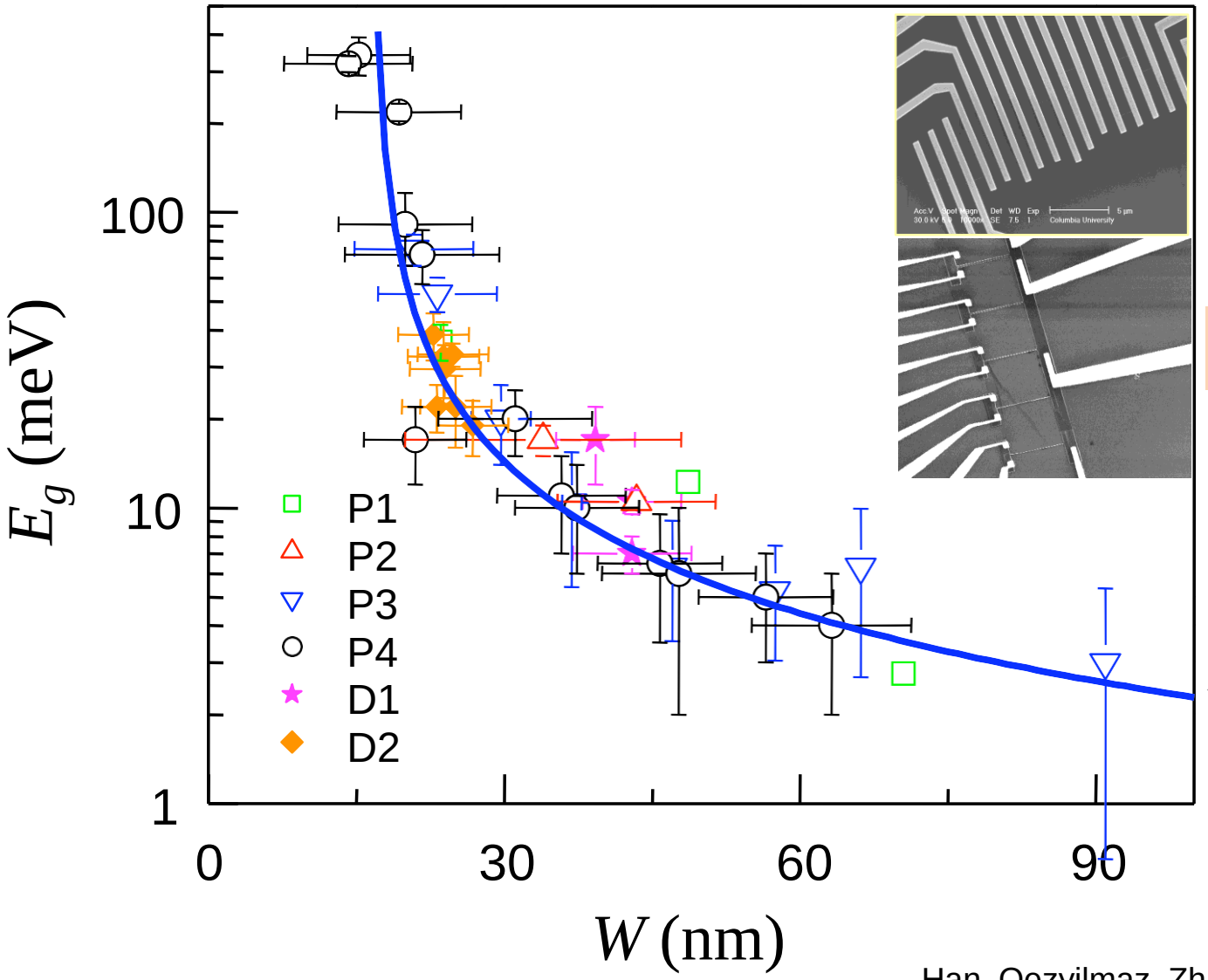

$E_{gap} \sim h v_F * k \sim h v_F / W$

$E_g = E_0 / (W - W_0)$

Han, Oezyilmaz, Zhang and Kim, PRL (2007)

Parent spectrum
Two dimensional Dirac Fermions

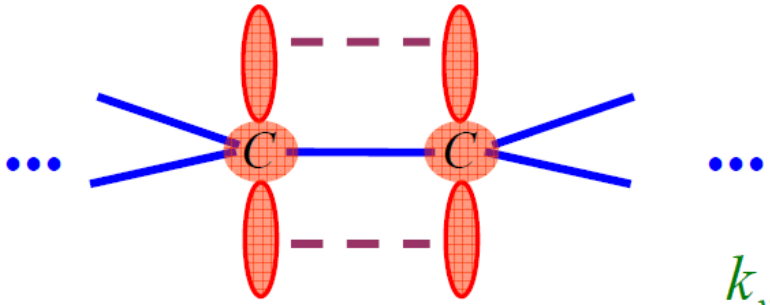

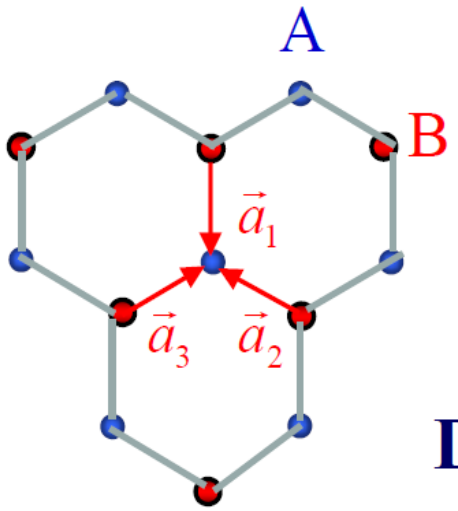

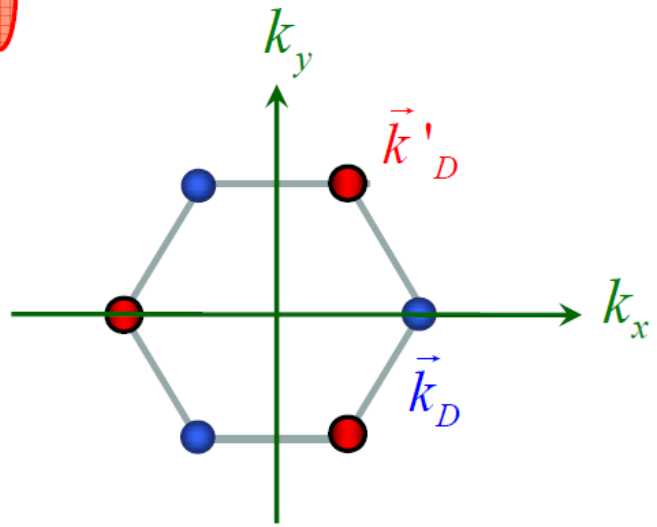

Dirac points

$$e^{i\vec{k}_D\cdot\vec{a}_n} = 1,\ e^{i2\pi/3},\ e^{i4\pi/3} \Leftrightarrow \sum_n e^{i\vec{k}_D\cdot\vec{a}_n} = 0$$

Pseudo Spin in Graphene Lattice

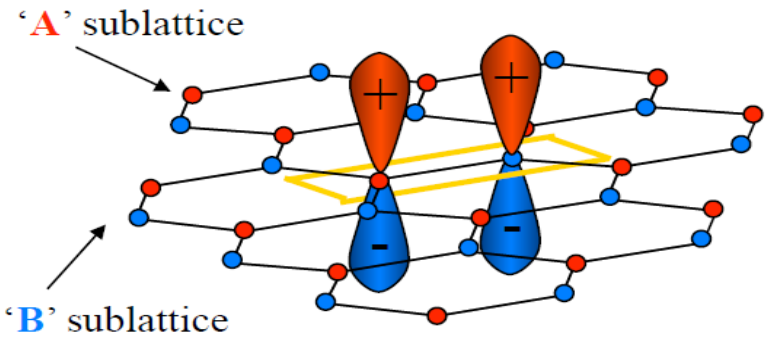

½ Spinor

$$\begin{pmatrix} 1 \\ e^{i\theta} \end{pmatrix}$$

$p_z^{A}(r)$

$p_z^{B}(r)$

Relative amplitude of sublattice wavefunctions

$p_z^{A}(r) + e^{i\theta} p_z^{B}(r)$ $\quad \theta = 0$: bonding $\theta = \pi$: antibonding

$k \cdot p$ perturbation theory

$$H_{eff} = \hbar v_F \begin{pmatrix} 0 & k_x - ik_y \\ k_x + ik_y & 0 \end{pmatrix} = \hbar v_F \vec{\sigma} \cdot \vec{k}_\perp$$

$$|k_\perp\rangle = e^{i\mathbf{k}\cdot\mathbf{r}} \frac{1}{\sqrt{2}} \begin{pmatrix} 1 \\ e^{i\theta_\kappa} \end{pmatrix}$$

$$\theta_k = \tan^{-1}(k_y / k_x)$$

DiVincenzo and Mele, PRB (1984); T. Ando, JPSJ (1998);McEuen at al, PRL (1999)

Dirac Fermions in Graphene : "Helicity"

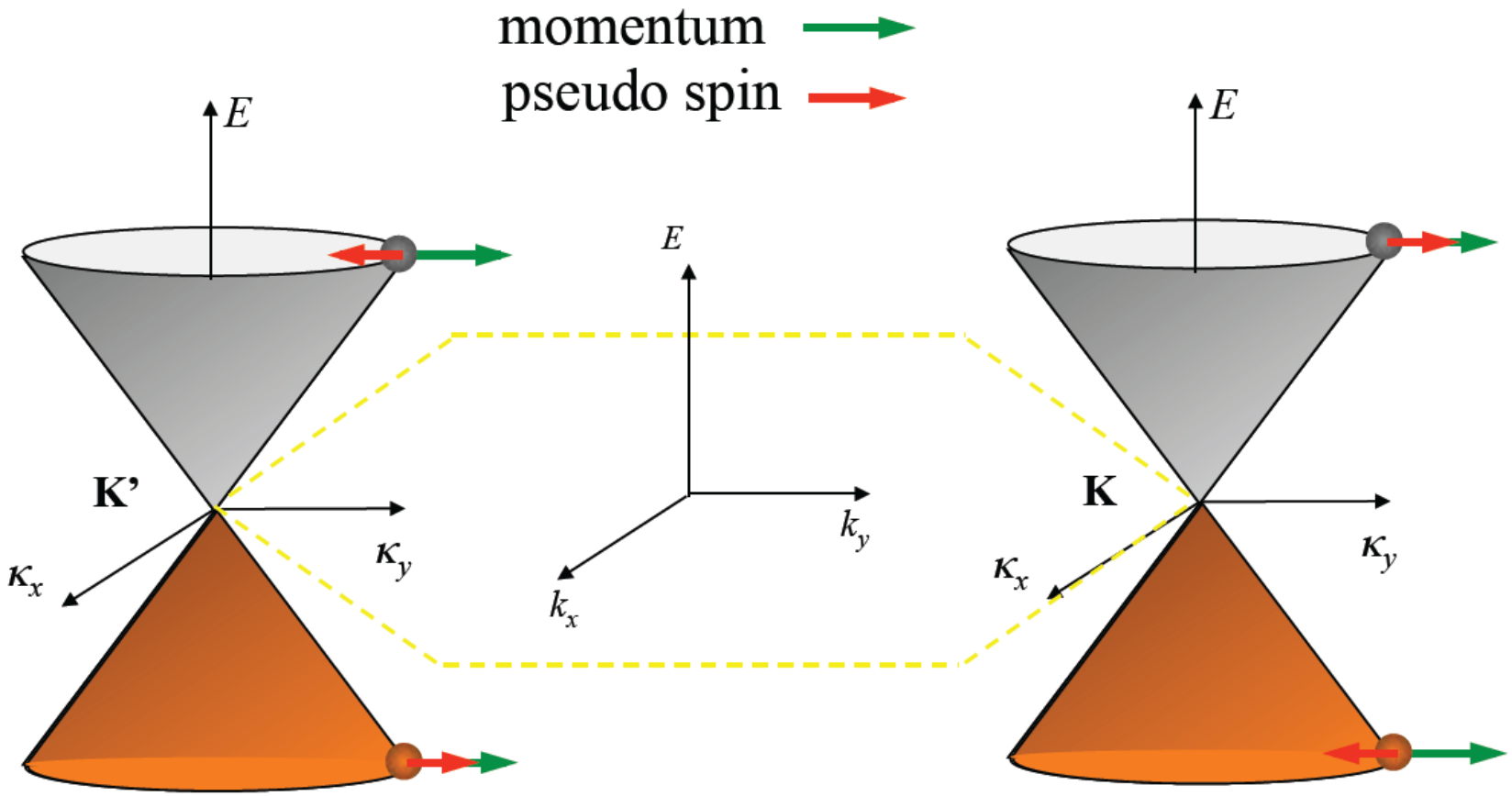

$$H_{eff} = \hbar v_F \vec{\sigma}^* \cdot \vec{k}_\perp$$

$$H_{eff} = \hbar v_F \vec{\sigma} \cdot \vec{k}_\perp$$

Electronic Structure and Pseudospin Physics in Graphene

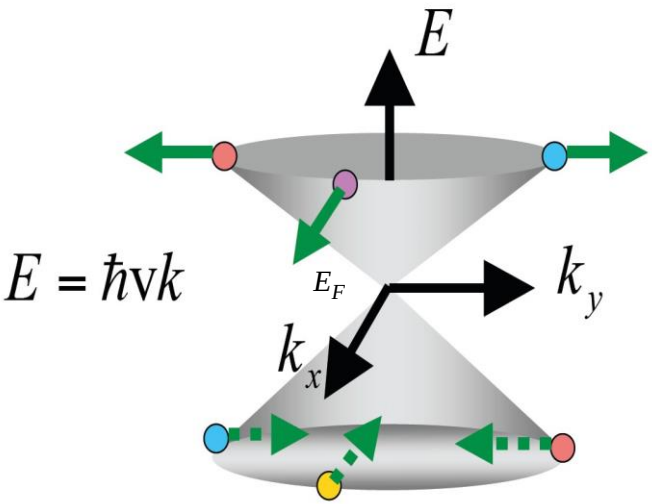

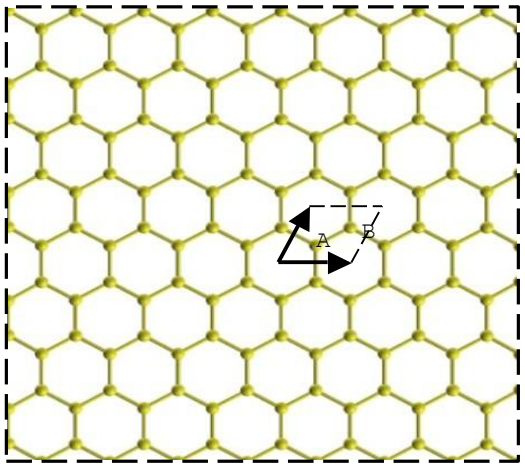

- Energy dispersion of the electron in graphene near the Fermi surface looks like that of ***light***, i.e., a cone.
- A pseudospin pointing along **k** associated with each state, describing the bonding character between the neighboring carbon atoms in the two sublattices.
- The ***chirality*** of graphene wavefunctions near the Dirac point suppresses backscattering events.

T. Ando, et al (1998); McEuen, Louie, et al (1999)

Extremely Long Mean Free Path: Hidden Symmetry ?

1D band structure of nanotubes

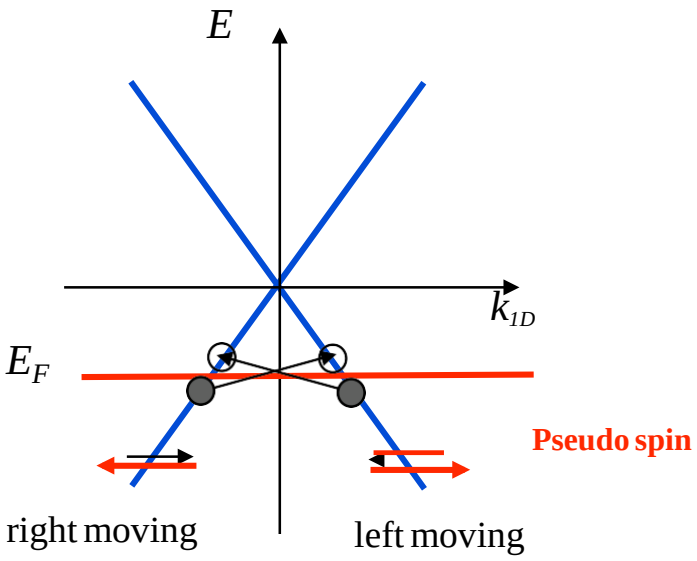

Low energy band structure of graphene

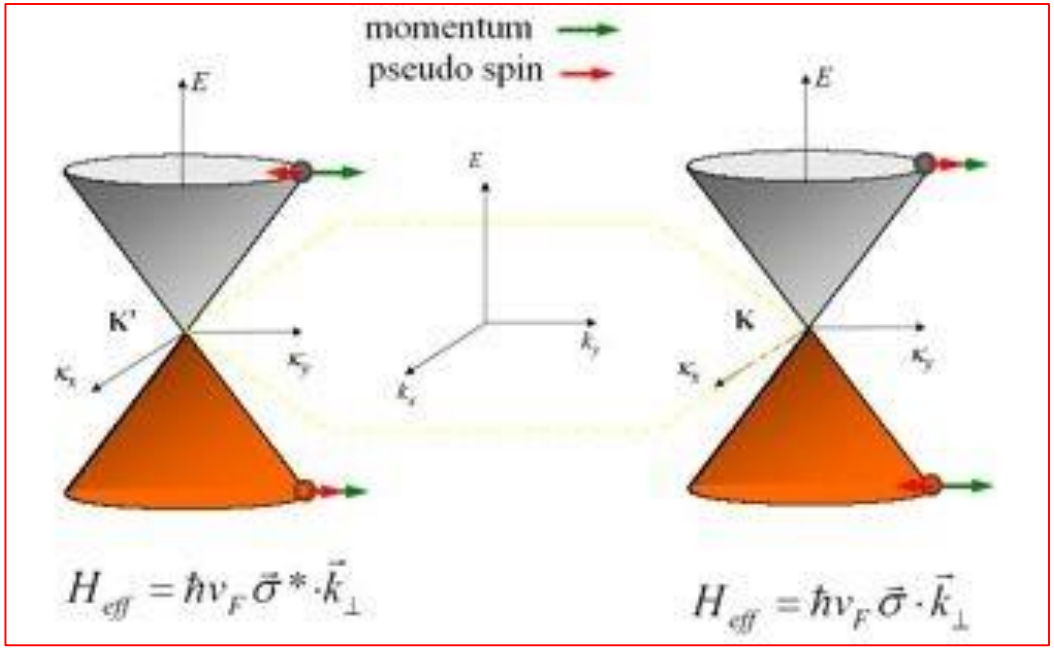

• Small momentum transfer backward scattering becomes inefficient, since it requires pseudo spin flipping.

T. Ando, JPSJ (1998); McEuen at al, PRL (1999)

Berry's Phase and Magnetoresistance Oscillations

Landau orbit near the Fermi level

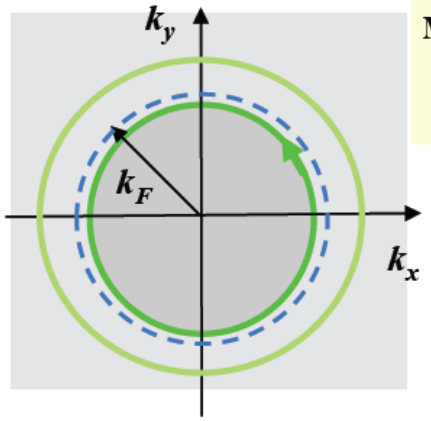

Magnetic flux in cyclotron orbit

$$\Phi_B = \Phi_o \, B_F/B$$

$$\Phi_o = h/e$$

$$B_F = \Phi_o \, k_F^2/4\pi$$

$$\psi \sim \psi_o \exp[2\pi(\Phi_B/\Phi_o)]$$

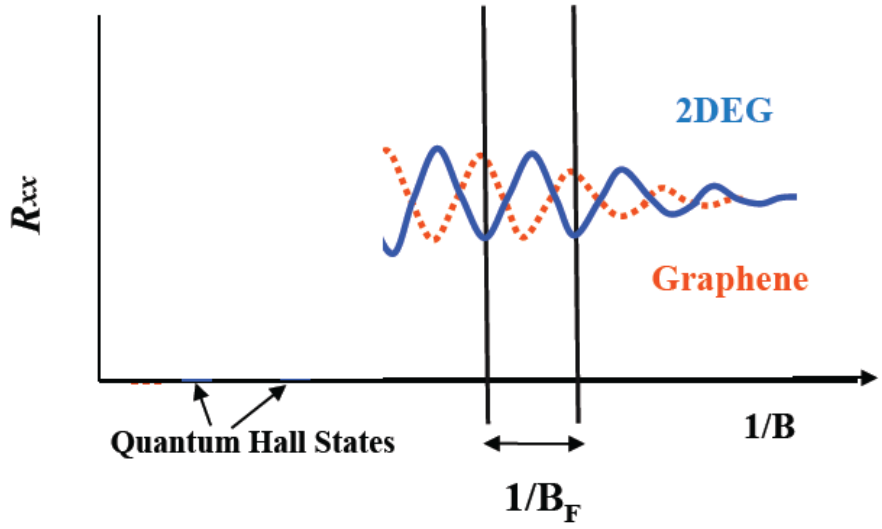

Graphene: $H_{eff} = \hbar v_F \vec{\sigma} \cdot \vec{k}'_{\perp}$

Pseudo Spin

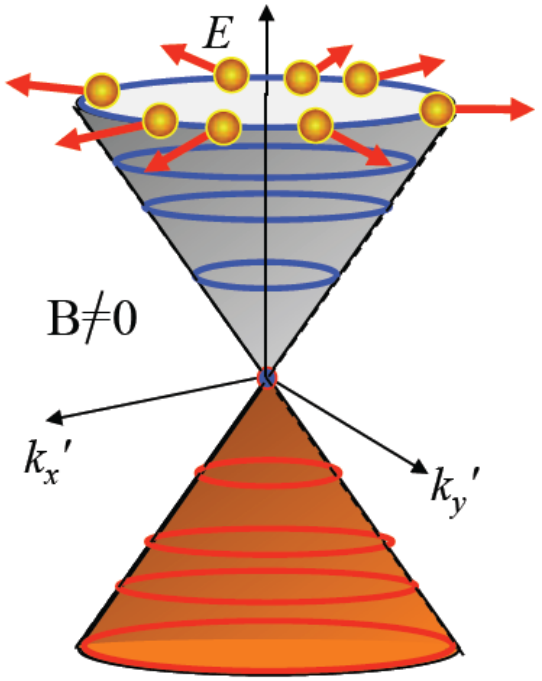

$S = \hbar/2$

$\theta = 2\pi$

$$\psi \sim \psi_o \exp[2\pi(\Phi_B/\Phi_o) - \underbrace{S\theta/h}_{\pi}]$$

k·p perturbation theory

In solid state theory, the k·p perturbation theory is an approximated semi-empirical approach for calculating the band structure, particularly effective mass and optical properties of crystalline solids.

Bloch's theorem and wavevectors

According to quantum mechanics (in the single-electron approximation), the quasi-free electrons in any solid are characterized by wavefunctions which are eigenstates of the following stationary Schrödinger equation:

$$\left(\frac{p^2}{2m} + V\right)\psi = E\psi$$

where **p** is the quantum-mechanical momentum operator, V is the potential, and m is the vacuum mass of the electron. (This equation neglects the spin–orbit effect; see below.)

In a crystalline solid, V is a periodic function, with the same periodicity as the crystal lattice. Bloch's theorem proves that the solutions to this differential equation can be written as follows:

$$\psi_{n,\mathbf{k}}(\mathbf{x}) = e^{i\mathbf{k}\cdot\mathbf{x}} u_{n,\mathbf{k}}(\mathbf{x})$$

where **k** is a vector (called the *wavevector*), n is a discrete index (called the *band index*), and $u_{n,\mathbf{k}}$ is a function with the same periodicity as the crystal lattice.

Perturbation theory

The periodic function $u_{n,\mathbf{k}}$ satisfies the following Schrödinger-type equation[1]

$$H_{\mathbf{k}} u_{n,\mathbf{k}} = E_{n,\mathbf{k}} u_{n,\mathbf{k}}$$

where the Hamiltonian is

$$H_{\mathbf{k}} = \frac{p^2}{2m} + \frac{\hbar \mathbf{k} \cdot \mathbf{p}}{m} + \frac{\hbar^2 k^2}{2m} + V$$

Note that $\mathbf{k}$ is a vector consisting of three real numbers with dimensions of inverse length, while $\mathbf{p}$ is a vector of operators; to be explicit,

$$\mathbf{k} \cdot \mathbf{p} = k_x(-i\hbar\frac{\partial}{\partial x}) + k_y(-i\hbar\frac{\partial}{\partial y}) + k_z(-i\hbar\frac{\partial}{\partial z})$$

In any case, we write this Hamiltonian as the sum of two terms:

$$H = H_0 + H'_{\mathbf{k}}, \quad H_0 = \frac{p^2}{2m} + V, \quad H'_{\mathbf{k}} = \frac{\hbar^2 k^2}{2m} + \frac{\hbar \mathbf{k} \cdot \mathbf{p}}{m}$$

We define the **effective mass** m^* by

$$\boxed{\frac{1}{m^*} = \frac{1}{\hbar^2}\frac{d^2\epsilon}{dk^2}}\ .$$

Tight Binding Model

Band structure

- Tight-binding model with nonorthogonal orbitals

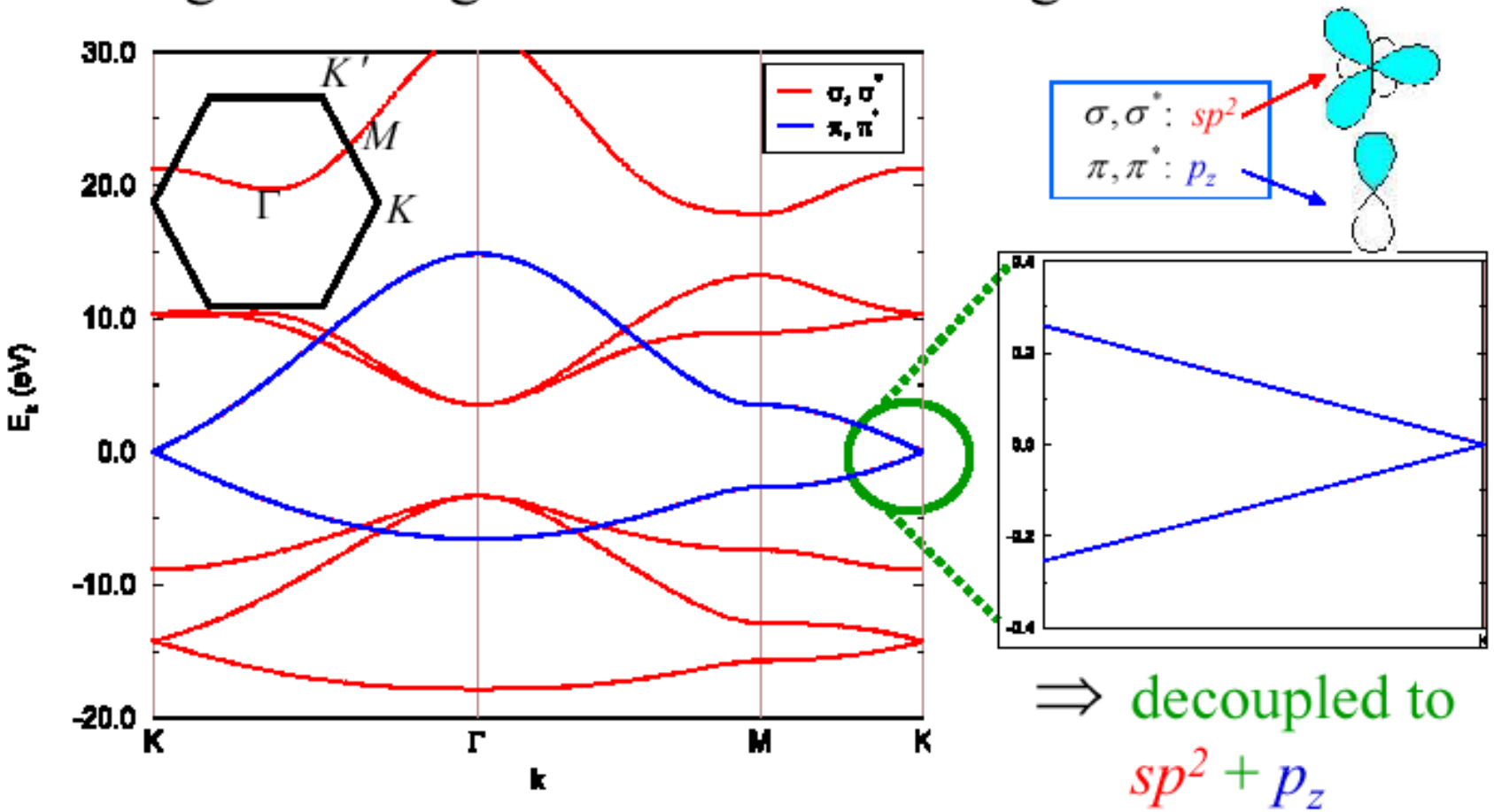

$\Rightarrow$ decoupled to $sp^2 + p_z$

Berry Phase

- **Berry phase**, is a phase difference acquired over the course of a cycle, when a system is subjected to *cyclic adiabatic* process, which results from the geometrical properties of the parameter space of the Hamiltonian.
- In case of **the Aharonov–Bohm effect**, the adiabatic parameter is the magnetic field enclosed by two interference paths, and it is cyclic in the sense that these two paths form a loop.
- Berry phase in quantum mechanics:

In a quantum system at the n^{th} eigenstate, an adiabatic evolution of the Hamiltonian sees the system remain in the n^{th} eigenstate of the Hamiltonian, while also obtaining a phase factor. The phase obtained has a contribution from the state's time evolution and another from the variation of the eigenstate with the changing Hamiltonian. The second term corresponds to the Berry phase, and for non-cyclical variations of the Hamiltonian it can be made to vanish by a different choice of the phase associated with the eigenstates of the Hamiltonian at each point in the evolution. However, *if the variation is cyclical*, the Berry phase cannot be cancelled; it is invariant and becomes an observable property of the system. We could characterize the whole change of the *adiabatic process into* ***a phase term***. Under the adiabatic approximation, the coefficient of the n^{th} eigenstate under adiabatic process is given by

$$C_n(t) = C_n(0)\exp\left[-\int_0^t \langle\psi_n(t')|\dot{\psi}_n(t')\rangle dt'\right] = C_n(0)e^{i\gamma_m(t)}$$

where $\gamma_m(t)$ is the Berry phase with respect of parameter *t.*

Changing the variable t into generalized parameters, we could rewrite the Berry phase into

$$\gamma[C] = i \oint_C \langle n, t | \left(\nabla_R | n, t \rangle \right) \, dR$$

, where ***R*** parametrizes the cyclic adiabatic process. It follows a closed path ***C*** in the appropriate parameter space. Geometric phase along the closed path ***C*** can also be calculated by integrating the Berry curvature over surface enclosed by ***C***.

Geometric phase and quantization of cyclotron motion

Electron subjected to magnetic field ***B*** moves on a circular (cyclotron) orbit. Classically, any cyclotron radius R_c is acceptable. Quantum-mechanically, only discrete energy levels (Landau levels) are allowed, and since R_c is related to electron's energy, this corresponds to quantized values of R_c. The energy quantization condition obtained by solving Schrödinger's equation reads, $E = (n + \alpha)\hbar\omega_c, \alpha = 1/2$ for free electrons (in vacuum), or $E = v\sqrt{2(n+\alpha)eB\hbar}, \alpha = 0$ for electrons in graphene where $n = 0, 1, 2, \ldots$. The alternative way of derivation is based on the semiclassical Bohr-Sommerfeld quantization condition

$$\hbar \oint d\mathbf{r} \cdot \mathbf{k} - e \oint d\mathbf{r} \cdot \mathbf{A} + \hbar\gamma = 2\pi\hbar(n + 1/2)$$

which includes the geometric phase γ picked up by the electron, while it executes its (real-space) motion along the closed loop of the cyclotron orbit. For free electrons, $\gamma = 0$ while $\gamma = \pi$ ctrons in graphene. It turns out that the geometric phase is directly linked to $\alpha = 1/2$ of free electrons and $\alpha = 0$ graphene.

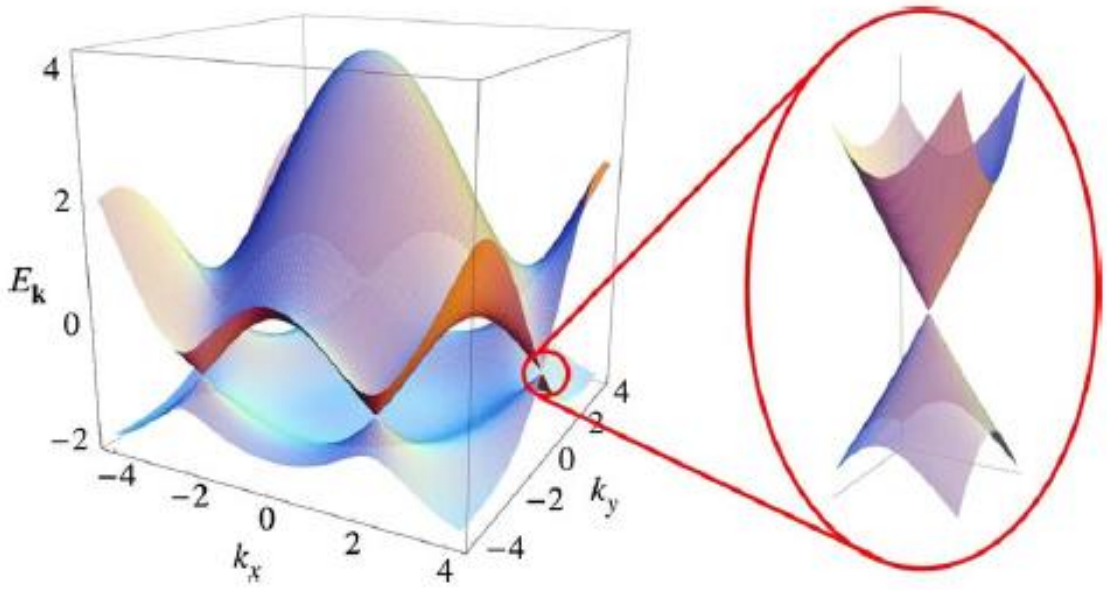

FIG. 3. (Color online) Electronic dispersion in the honeycomb lattice. Left: energy spectrum (in units of t) for finite values of t and t', with $t=2.7$ eV and $t'=-0.2t$. Right: zoom in of the energy bands close to one of the Dirac points.

Quasi-Dirac Fermions

$E = \hbar \upsilon k$ with $m = 0$

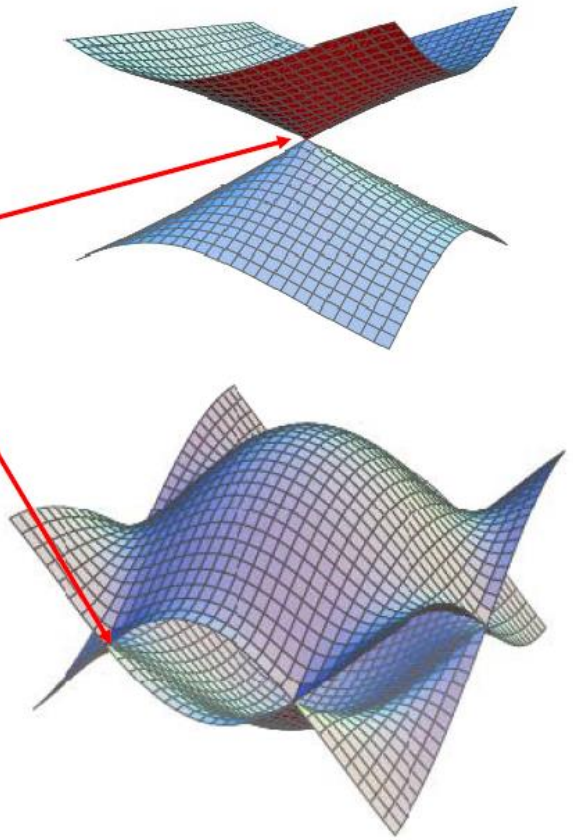

Dirac points

New playground for testing relativistic QM and QED!

Not exactly Dirac Fermions

$\upsilon \approx c/300$

$k_D \neq 0$ and inter-Dirac point scatterings!

Transition Metal Dichalcogenides
MoS_2 (TMD) and
more on
2-D layered materials

The rise of the flattest materials

The number of papers on graphene has grown exponentially since the material was isolated in 2004. Publications about molybdenum disulfide (MoS_2) and phosphorene are now repeating the pattern.

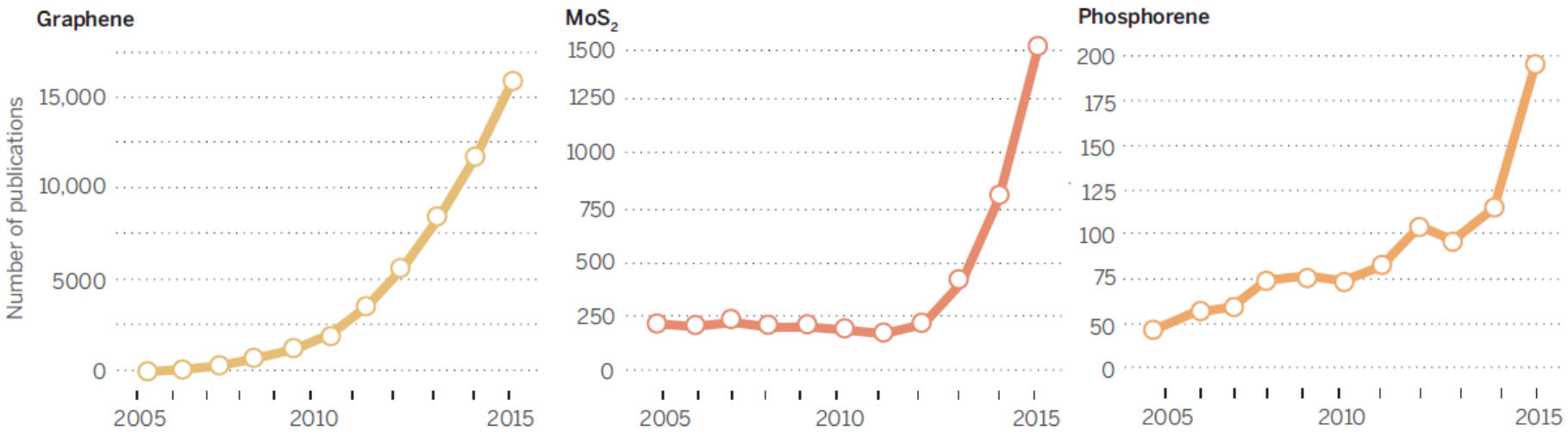

Transition Metal Dichalcogenides (TMDs)

Formula : MX_2 M (transition metals) = Mo, W, Nb, Re, Ti, Ta, etc.
X (chalcogenides) = S, Se, or Te

Semiconducting TMDs

- Semi-metal: TiS_2
- Charge-density-wave (CDW)
- Superconductivity: i.e. MoS_2 Appl. Phys. Lett. 101, 042603 (2012);
- Metal-Insulator Transition (http://arxiv.org/abs/1301.4947)
- **Valleytronics**, involves channeling the charge carriers into "valleys" of set momentum in a controlled way.

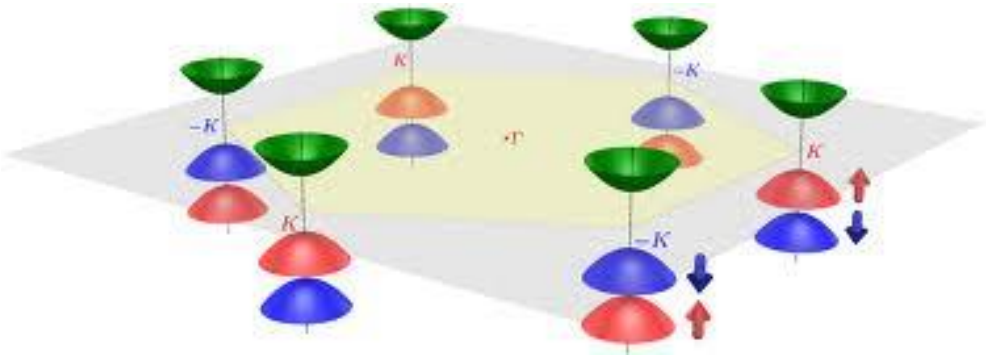

Motivation

1. Why TMDs?
   - A 2D semiconducting transition metal dichalcogenides with potential applications that could complement those of *Graphene*.
     - High on/off ratio and moderate mobility: *electronics*
     - Direct bandgap (for monolayer): *optoelectronics*
     - *Valleytronics*
   - *Large area vapor phase growth accessible (so far MoS_2)*

2. Bandgap Engineering
   - Layer numbers (quantum confinement)
   - Strain
   - Temperature
   - Potentially leads to many optoelectronics applications.

Introduction: TMDc Monolayer

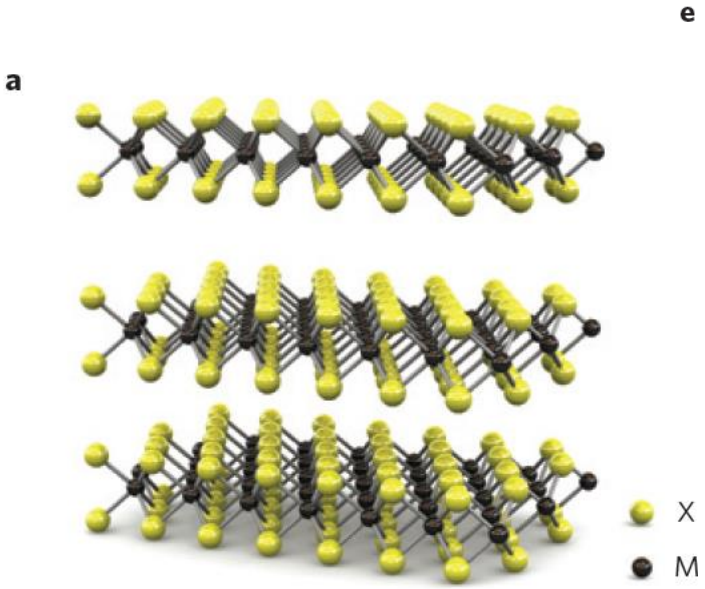

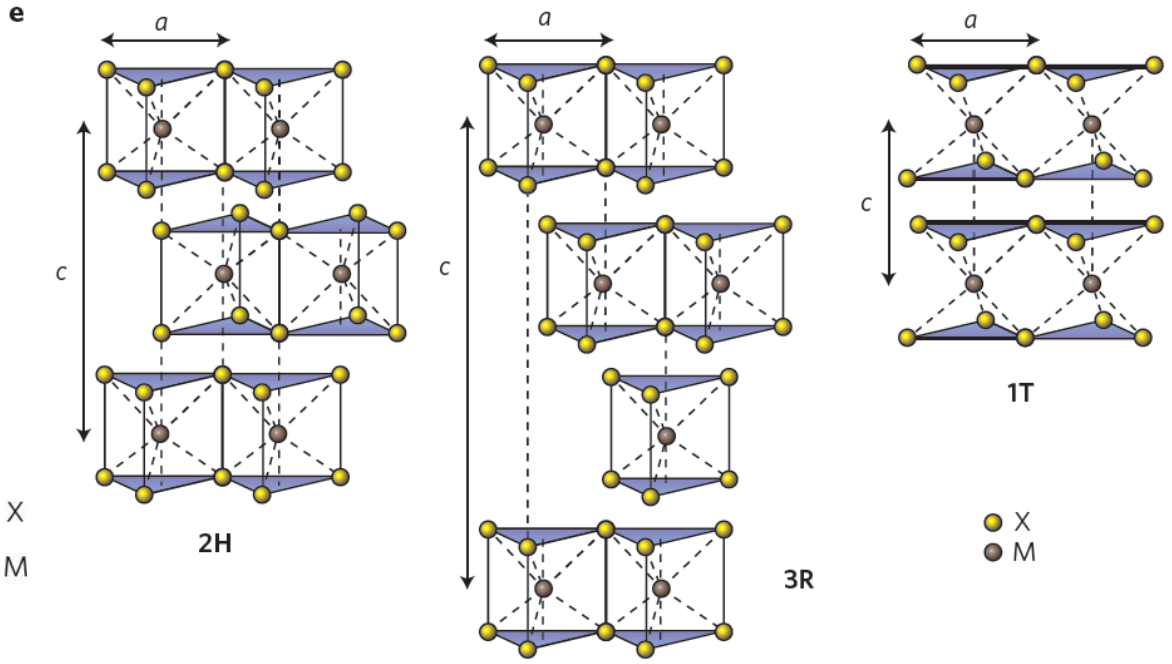

Schematics of the structural polytypes:

- 2H (hexagonal symmetry, two layers per repeat unit, trigonal prismatic coordination),
- 3R (rhombohedral symmetry, three layers per repeat unit, trigonal prismatic coordination), and
- 1T (tetragonal symmetry, one layer per repeat unit, octahedral coordination).

Andras Kis, Nature Nanotech, Vol 6, No 3, 146, (2011).

Schematic illustration of the experimental set-up for CVD-growth of MoS_2

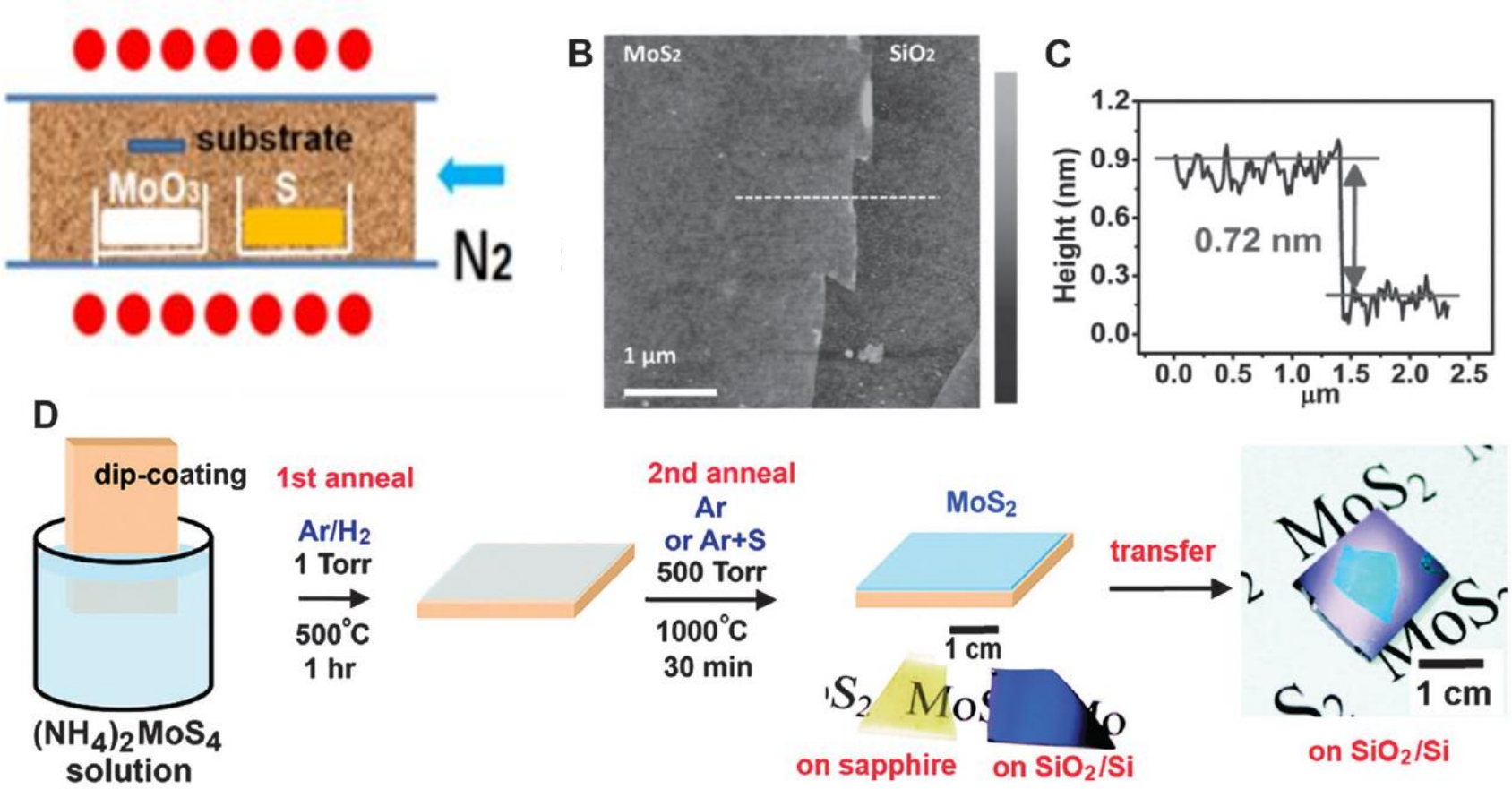

Andras Kis, Nature Nanotechnology
Vol 6, No 3, 146, (2011).

Synthesis: the thinnest semiconductors, TMD Monolayer

- Scalable,
- Single Crystal
- Thinnest semiconductors

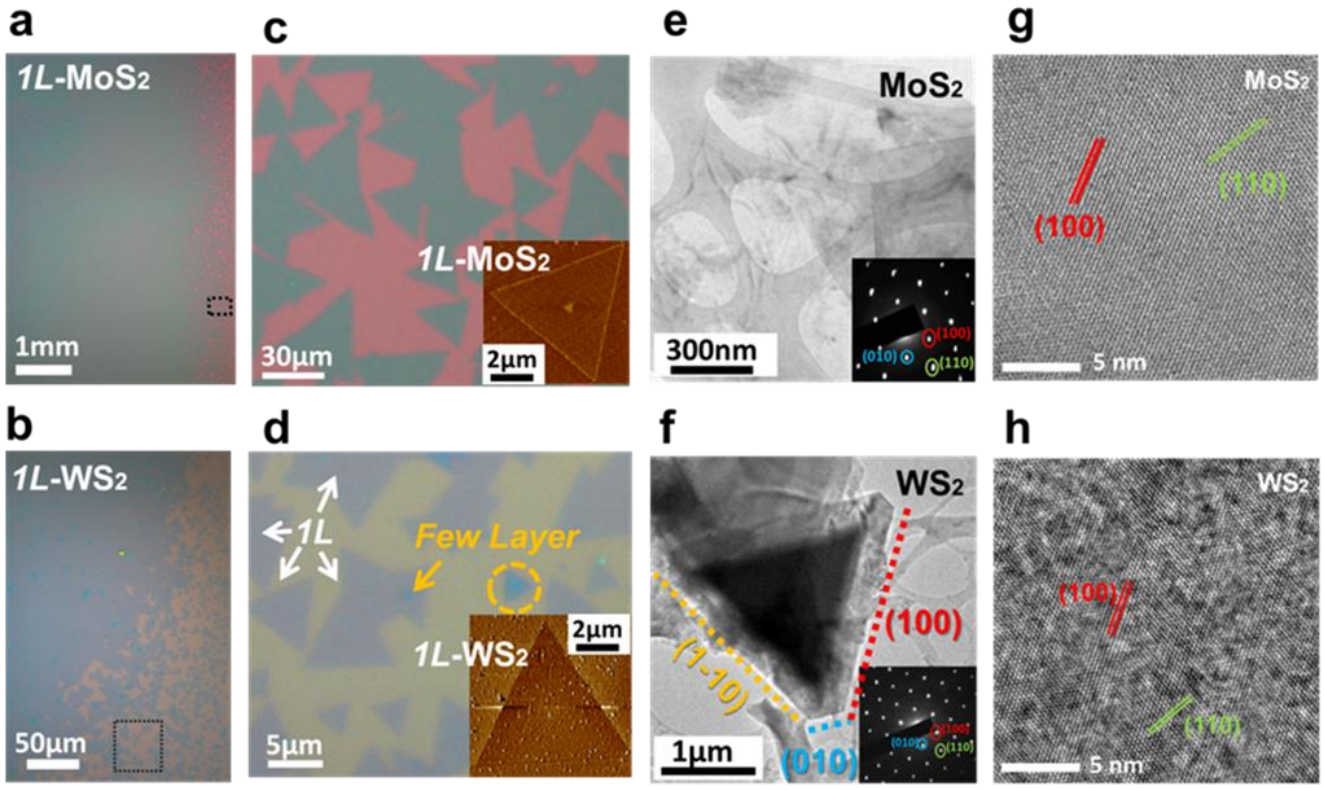

Synthesis of Single Layer Transition Metal Disulfides on Diverse Surfaces

YHLee et. al., ***Nano Lett***. 13, 1852–1857 (2013)

YHLee et. al, ***Adv. Mater***. 24, 2320-2325 (2012)

Atomically Thin MoS_2: A New Direct-Gap Semiconductor

K. F. Mak, T. Heinz, PRL 105, 136805 (2010)

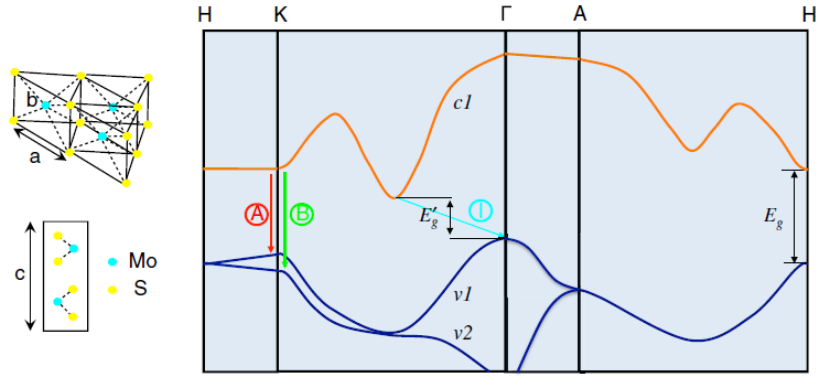

FIG. 1 (color online). Lattice structure of MoS_2 in both the in- and out-of-plane directions and simplified band structure of bulk MoS_2, showing the lowest conduction band $c1$ and the highest split valence bands $v1$ and $v2$. A and B are the direct-gap transitions, and I is the indirect-gap transition. E_g' is the indirect gap for the bulk, and E_g is the direct gap for the monolayer.

- Via optical absorption, photoluminescence, and photoconductivity spectroscopy, the effect of quantum confinement of MoS_2 is traced.
- This leads to a crossover to a direct-gap material in the limit of the single monolayer.
- The freestanding monolayer exhibits an increase in luminescence quantum efficiency by more than a factor of 10^4 compared with the bulk material.

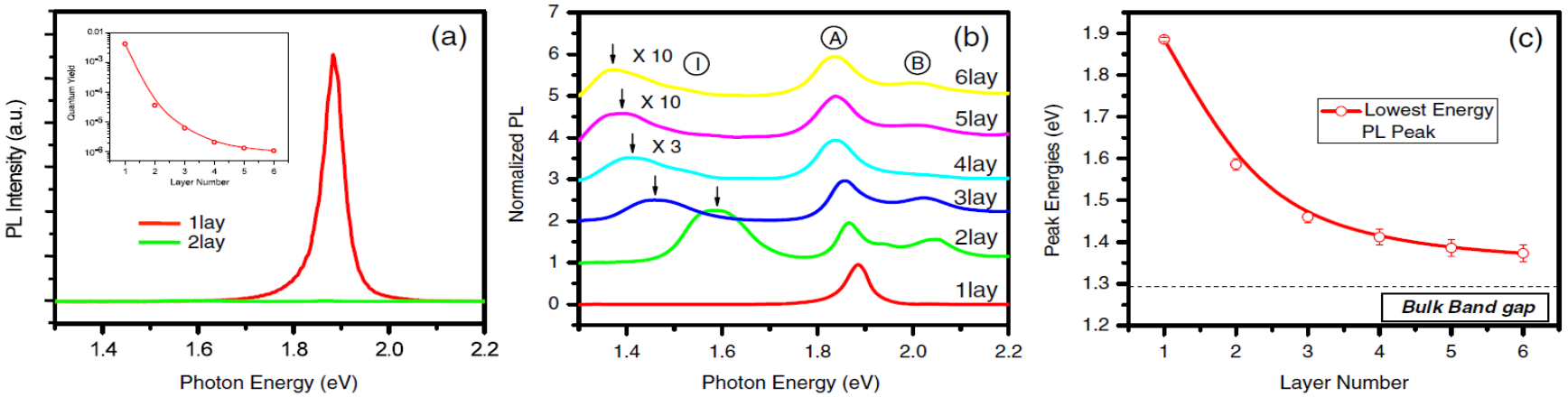

FIG. 3 (color online). (a) PL spectra for mono- and bilayer MoS_2 samples in the photon energy range from 1.3 to 2.2 eV. Inset: PL QY of thin layers for $N = 1$–6. (b) Normalized PL spectra by the intensity of peak A of thin layers of MoS_2 for $N = 1$–6. Feature I for $N = 4$–6 is magnified and the spectra are displaced for clarity. (c) Band-gap energy of thin layers of MoS_2, inferred from the energy of the PL feature I for $N = 2$–6 and from the energy of the PL peak A for $N = 1$. The dashed line represents the (indirect) band-gap energy of bulk MoS_2.

Table 1 | Summary of TMDC materials and properties.

	-S_2		-Se_2		-Te_2	
	Electronic characteristics	**References**	**Electronic characteristics**	**References**	**Electronic characteristics**	**References**
Nb	Metal; superconducting; CDW	138 (E)	Metal; superconducting; CDW	138,164 (E)	Metal	83 (T)
Ta	Metal; superconducting; CDW	138,164 (E)	Metal; superconducting; CDW	138,164 (E)	Metal	83 (T)
Mo	Semiconducting 1L: 1.8 eV Bulk: 1.2 eV	31 (E) 88 (E)	Semiconducting 1L: 1.5 eV Bulk: 1.1 eV	82 (T) 88 (E)	Semiconducting 1L: 1.1 eV Bulk: 1.0 eV	82 (T) 165 (E)
W	Semiconducting 1L: 2.1 eV 1L: 1.9 eV Bulk: 1.4 eV	25 (T) 82 (T) 88 (E)	Semiconducting 1L: 1.7 eV Bulk: 1.2 eV	83 (T) 88 (E)	Semiconducting 1L: 1.1 eV	83 (T)

Andras Kis, Nature Nanotechnology Vol 6, No 3, 146, (2011).

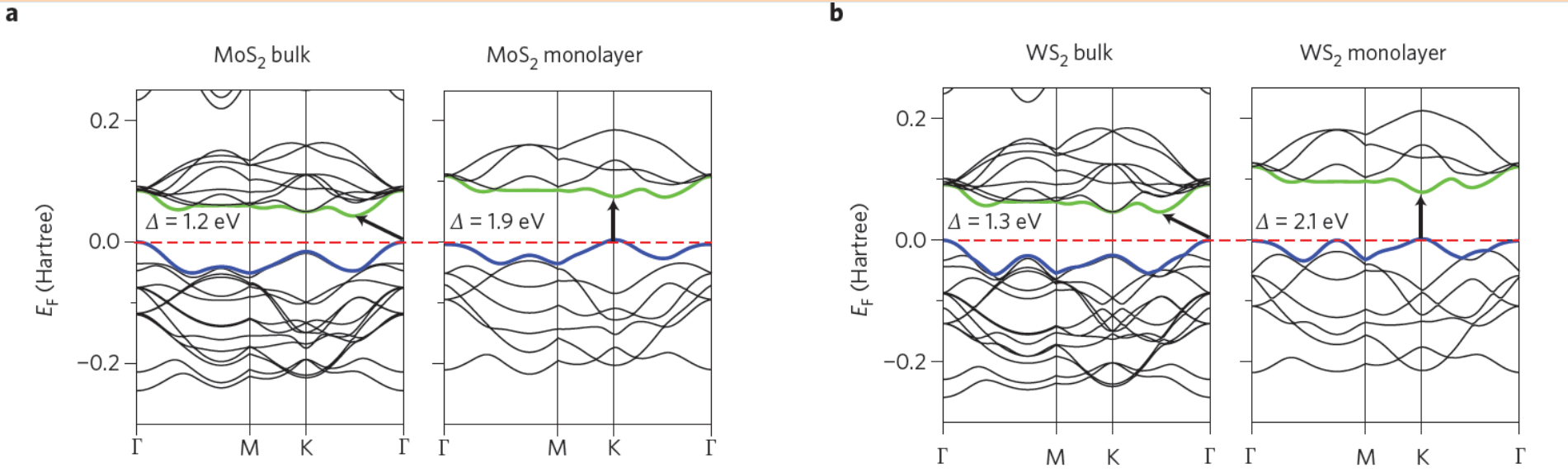

Coupled Spin and Valley Physics in MoS_2

- Inversion symmetry breaking, together with strong SOC, lead to coupled spin and valley physics in monolayer MoS_2 and other group-VI dichalcogenides, making possible spin and valley control in these 2D materials.
- First, the valley Hall effect is accompanied by a spin Hall effect in both electron-doped and hole-doped systems.
- Second, spin and valley relaxation are suppressed at the valence-band edges, as flip of each index alone is forbidden by the valley-contrasting spin splitting (0.1–0.5 eV) caused by inversion symmetry breaking.
- Third, the valley-dependent optical selection rule also becomes spin-dependent, and carriers with various combination of valley and spin indices can be selectively excited by optical fields of different circular polarizations and frequencies.
- We predict photo-induced charge Hall, spin Hall and valley Hall effects.

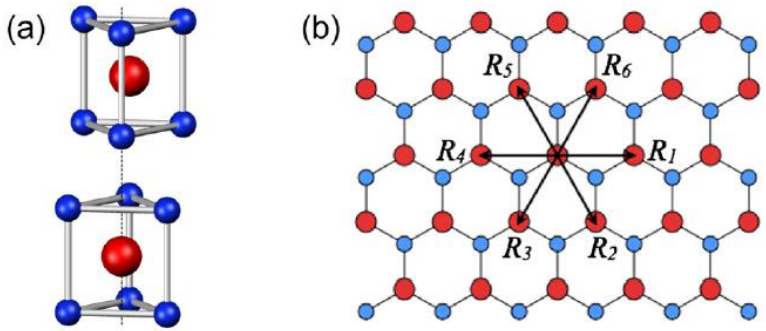

Di Xiao et al, PRL **108**, 196802 (2012)

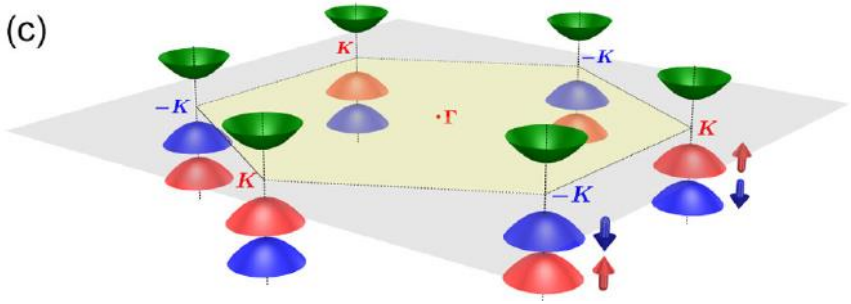

FIG. 1 (color online). (a) The unit cell of bulk $2H$-MoS_2, which has the inversion center located in the middle plane. It contains two unit cells of MoS_2 monolayers, which lacks an inversion center. (b) Top view of the MoS_2 monolayer. $\boldsymbol{R}_i$ are the vectors connecting nearest Mo atoms. (c) Schematic drawing of the band structure at the band edges located at the K points.

Photo-induced charge Hall, spin Hall, and valley Hall effects

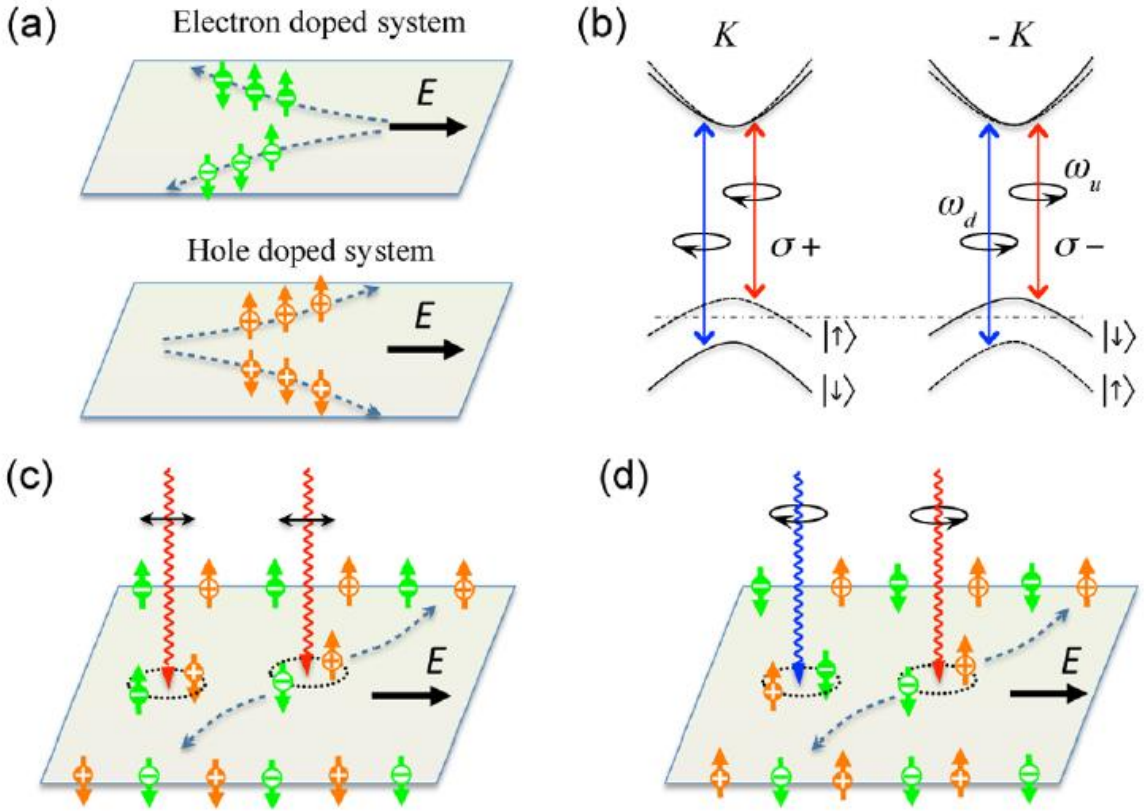

Coupled spin and valley physics in monolayer group-VI dichalcogenides.
The electrons and holes in valley K are denoted by white '+', and '–' symbol in dark circles and their counterparts in valley – K are denoted by inverse color. (a) Spin Hall effects in electron and hole-doped systems. (b) Valley and spin optical transition selection rules. Solid (dashed) curves denote bands with spin-down (-up) quantized along the out-of-plane direction. The splitting in the conduction band is exaggerated. ω_u and ω_d are, respectively, the transition frequencies from the two split valence-band tops to the conduction band bottom. (c) Spin Hall effects of electrons and holes excited by linearly polarized optical field with frequency ω_u . (d) Valley Hall effects of electrons and holes excited by two-color optical fields with frequencies ω_u and ω_d and opposite circular polarizations.

Superconductivity in MoS_2

- **Electro-static carrier doping was attempted in a layered MoS_2 by constructing an electric double-layer transistor with an ionic liquid.**
- **With the application of gate voltage V_G > 3V, a metallic behavior was observed in the MoS_2 channel.**
- **An onset of electric field-induced superconductivity was found in the field induced metallic phase. With a maximum T_C of 9.4K.**
- **APL, 101, 042603 (2012).**

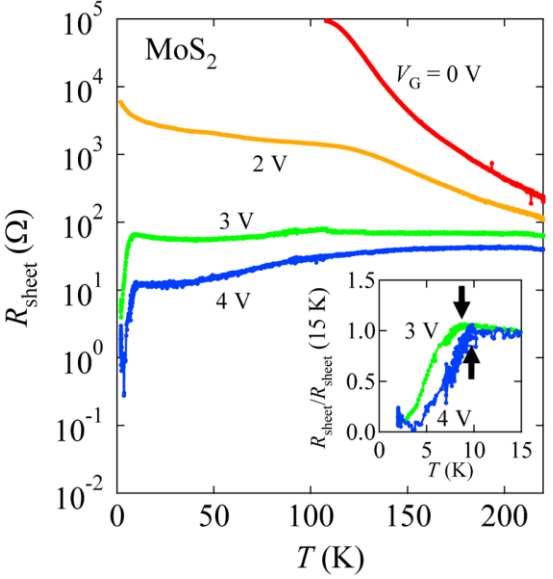

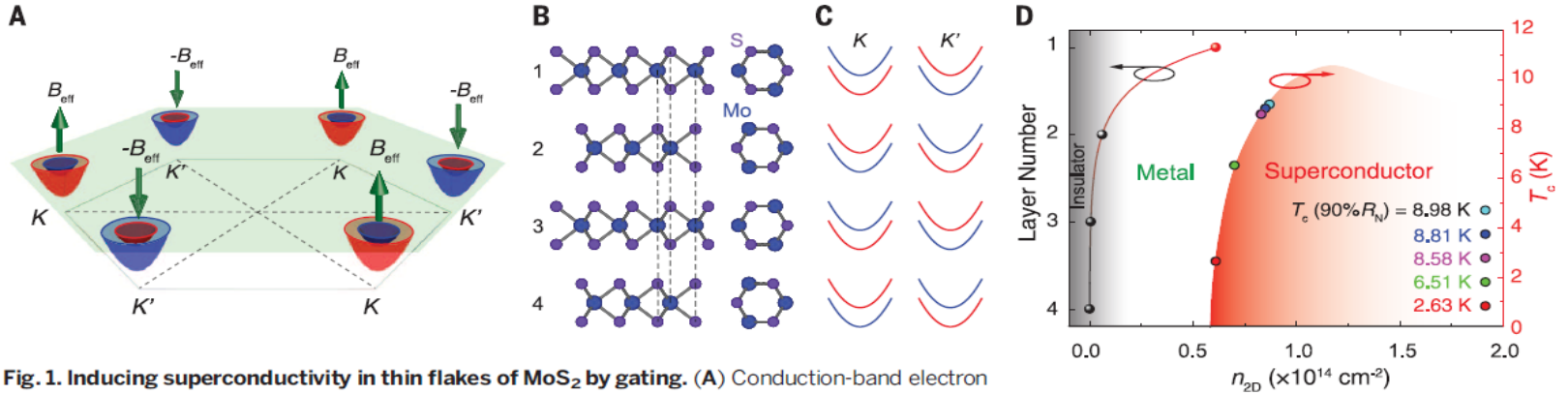

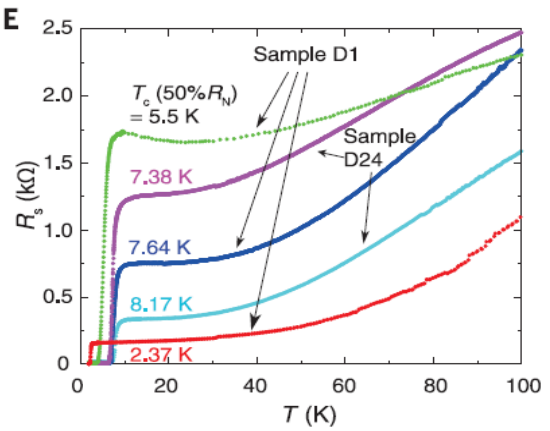

Fig. 1. Inducing superconductivity in thin flakes of MoS_2 by gating. (**A**) Conduction-band electron pockets near the *K* and *K'* points in the hexagonal Brillouin zone of monolayer MoS_2. Electrons in opposite *K* and *K'* points experience opposite effective magnetic fields $\mathbf{B}_{eff}$ and $-\mathbf{B}_{eff}$, respectively (green arrows). The blue and red colored pockets indicate electron spins oriented up and down, respectively. (**B**) Side view (left) and top view (right) of the four outermost layers in a multilayered MoS_2 flake. The vertical dashed lines show the relative positions of Mo and S atoms in *2H*-type stacking. In-plane inversion symmetry is broken in each individual layer, but global inversion symmetry is restored in bulk after stacking. (**C**) Energy-band splitting caused by $\mathbf{B}_{eff}$. Blue and red bands denote spins aligned up and down, respectively. Because of *2H*-type stacking, adjacent layers have opposite $\mathbf{B}_{eff}$ at the same *K* points. (**D**) The red curve (left axis) denotes the theoretical carrier density n_{2D} for the four outermost layers of MoS_2 (*26*) for sample D1, when $T_c(0)$ = 2.37 K. In the phase diagram (right axis), superconducting states with different values of $T_c(0)$ are color-coded; the same color-coding is used across all figures. Here, T_c is determined at the temperature where the resistance drop reaches 90% of R_N at 15 K. This criterion is different from the 50% R_N criterion used in the rest of the paper; it was chosen to be consistent with that used in the phase diagram of (*17*). (**E**) Temperature dependence of R_s, showing different values of T_c corresponding to superconducting states (from samples D1 and D24) denoted in (D).

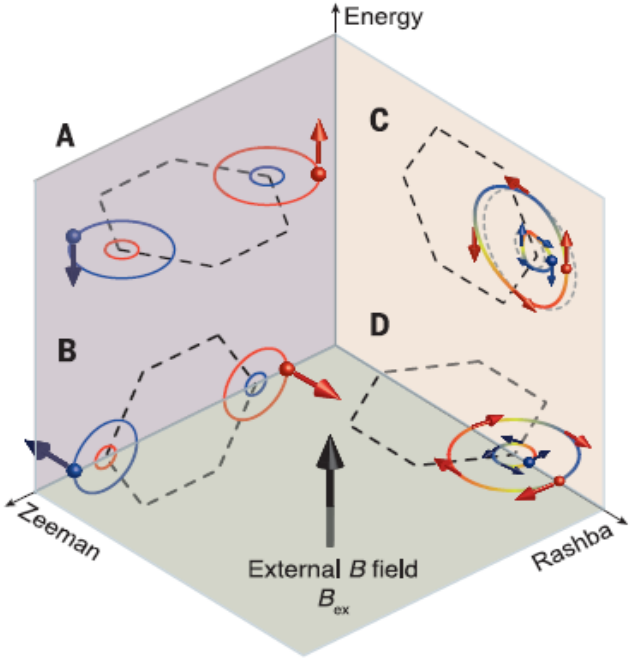

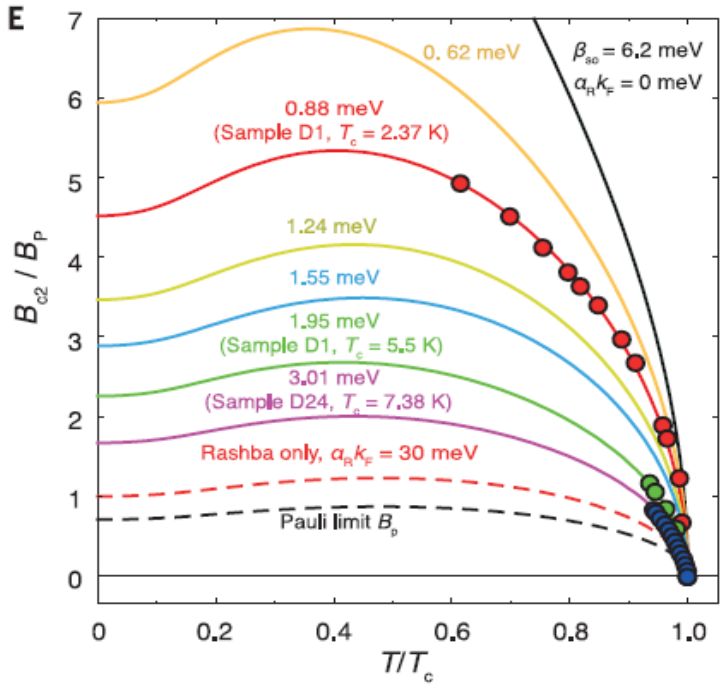

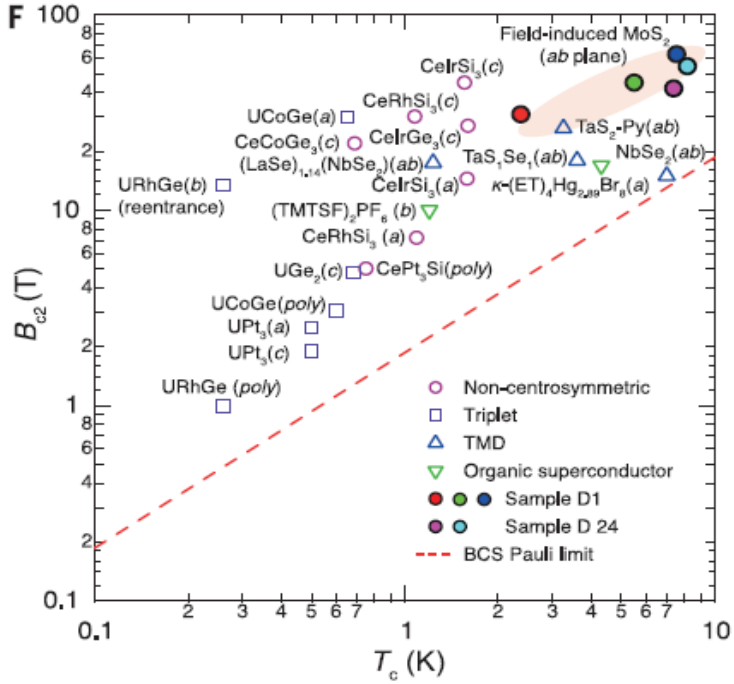

Fig. 4. Interplay between an external magnetic field and the spins of Cooper pairs aligned by Zeeman and Rashba-type effective magnetic fields. (**A** to **D**) Illustration of the acquisition of Zeeman energy through coupling between an external magnetic field and the spins of Cooper pairs formed near the *K* and *K*′ points of the Brillouin zone (not to scale). When Rashba or Zeeman SOC aligns the spins of Cooper pairs parallel to the external field, the increase in Zeeman energy due to parallel coupling between the field and the spin eventually can cause the pair to break [(A) and (C)]. In (B) and (D), the acquired Zeeman energy is minimized as a result of the orthogonal coupling between the field and the aligned spins, which effectively protects the Cooper pairs from depairing. (**E**) Theoretical fitting of the relationship between B_{c2}/B_p and T/T_c for samples D1 [$T_c(0)$ = 2.37 K and 5.5 K] and D24 [$T_c(0)$ = 7.38 K], using a fixed effective Zeeman field (β_{SO} = 6.2 meV) and an increasing Rashba field ($\alpha_R k_F$ ranges from 10 to ~50% of β_{SO}) [section 6 of (*16*)]. Two dashed lines show the special cases calculated by equation S3, when only the Rashba field ($\alpha_R k_F$ = 30 meV; β_{SO} = 0) is considered (red), and when both the Zeeman and Rashba fields are zero (black). In the former case, a large $\alpha_R k_F$ causes a moderate increase of B_{c2} to ~$\sqrt{2}B_p$ (*10*). In the latter case, the conventional Pauli limit at zero temperature is recovered. (**F**) Plot of B_{c2} versus T_c for different superconductors [a magnetic field was applied along crystal axes *a*, *b*, or *c* or to a polycrystalline (*poly*)]. The data shown are from well-known systems including noncentrosymmetric (pink circles), triplet (purple squares) (*6*, *8*, *9*), low-dimensional organic (green triangles) (*40*, *50*–*52*), and bulk TMD superconductors (blue triangles) (*35*–*38*, *47*). The robustness of the spin protection can be measured by the vertical distance between B_{c2} and the red dashed line denoting B_p. Gate-induced superconductivity from samples D1 and D24 are among the states with the highest B_{c2}/B_p ratio. In $(LaSe)_{1.14}(NbSe_2)$, T_c was determined at 95% of R_N; T_c in organic molecule–intercalated TMDs was obtained by extrapolating to zero resistance; and all other systems use the standard of 50% of R_N.

Field-effect transistors (FETs) based on MoS_2.

Andras Kis and co-workers have made an FET in which the channel is a single layer of MoS_2 that is just 0.65 nm thick and 1,500 nm long:

the black spheres in this schematic are Mo atoms; the yellow spheres are S atoms. The MoS_2 layer also has a bandgap, which is crucial for many applications.

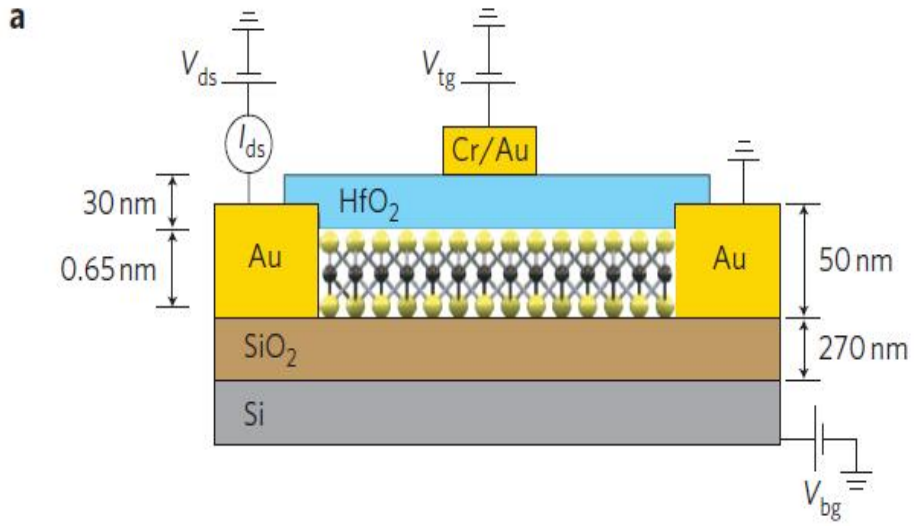

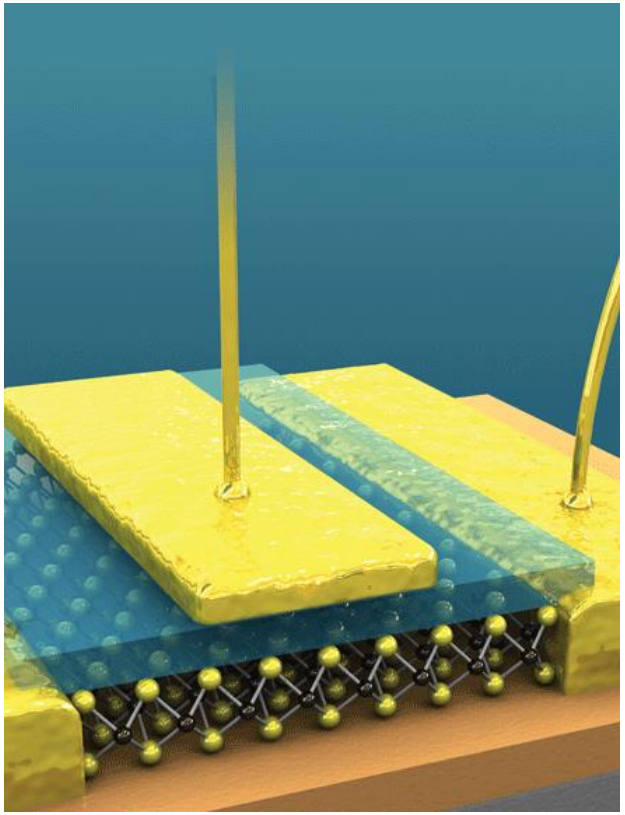

Andras Kis et al, Nature Nanotech. 6, No 3, 146, (2011).

MoS_2

- Switch on and off at 10^9 times/sec, a large on/off ratio, making it easy to differentiate between digital 1s and 0s.
- A Mobility ~ 200; and was later corrected to ~15.

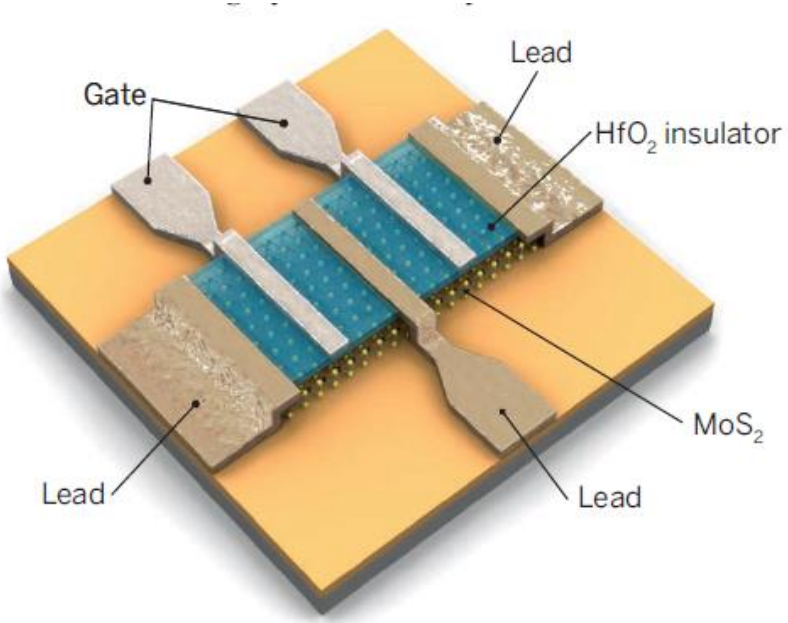

Researchers have made quick progress in turning 2D materials into devices, such as this simple circuit in which two transistors use MoS_2 to ferry charges between electrode leads.

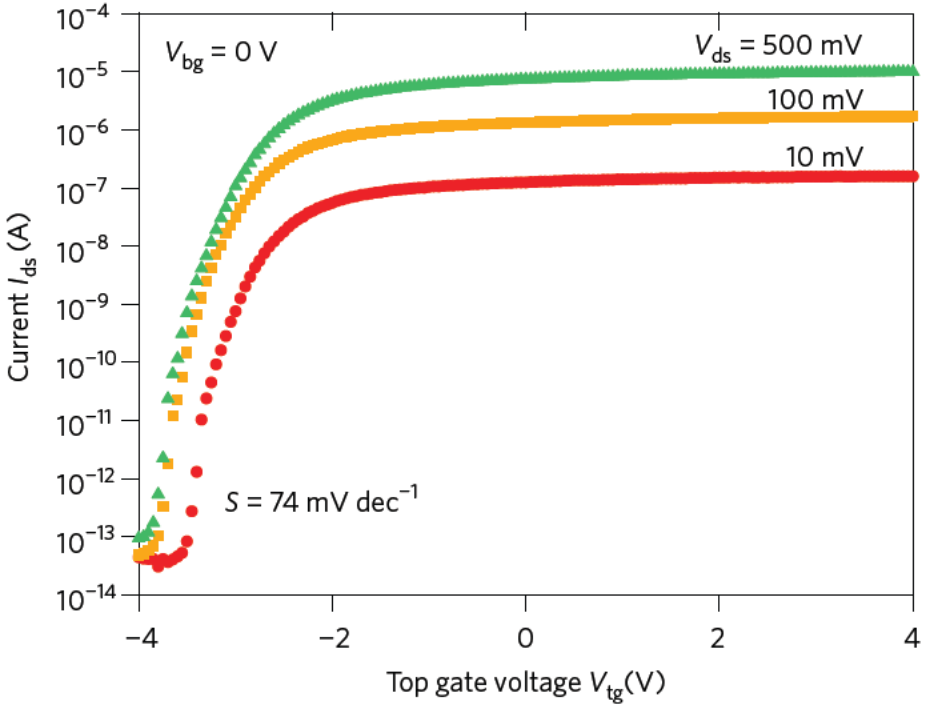

Andras Kis, Nature Nanotechnology Vol 6, No 3, 146, (2011).

Field-Effect Mobility (review)

Monolayer MoS_2

- Room temperature mobility
- Back-gated Silicon oxide : **0.1 - 50** $cm^2/V.s$ SS: $1cm^2/V.s$
- Dual gate (SiO_2+HfO_2): **15** cm^2/V sec
- Original ~200: Nat Nanotechnol **6**, 147 (2011)
- Correction ~ 15: Nat Nanotechnol **8**, 147 (2013)
- On/off ratio: 10^8

Multilayer MoS_2

- Back-gated Al_2O_3: **100** $cm^2/Vsec$
- multilayer MoS_2: 30nm
- On/off ratio: 10^6

  Nature Communications, 3, 1011 (2012)
- On PMMA: $470cm^2/V.s$(electrons)

  $480cm^2/V.s$(holes)

  APL 102(4), 042104 (2013)

MoS_2 Optoelectronics

- MoS_2's strong interactions with light would be favorable for solar cells, light emitters, and other optical devices.

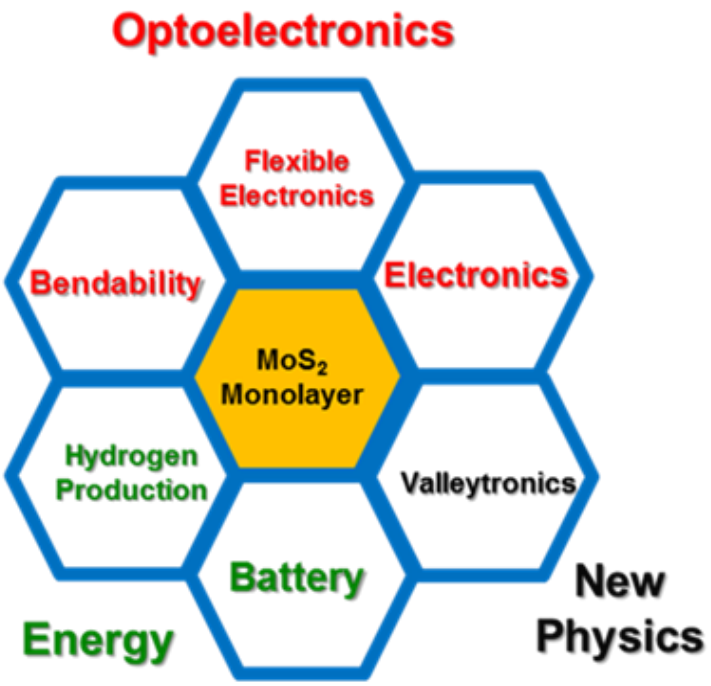

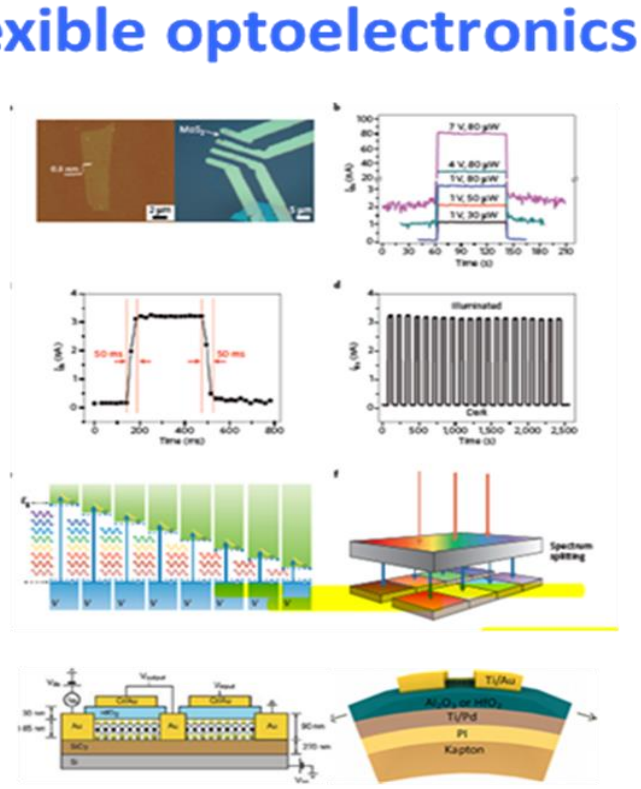

QH **Wang** et al,
Nat. Nano, 7, p699 (2012)

Applications: Electronics

Large-scale CVD-MoS_2 Monolayer Devices:

H. Wang, L. Yu, YH Lee et. al., ***IEDM Tech. Digest***, 2012

-the best paper award in IEDM 2012

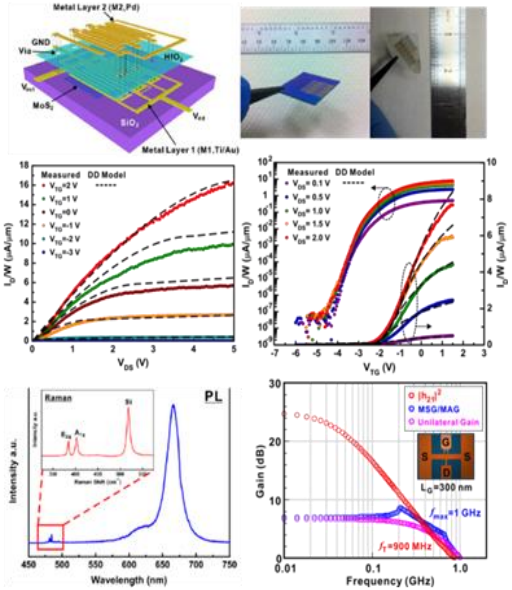

CVD-MoS_2 Monolayer Mixed-signal Circuits

H. Wang, YHLee et. al., (in-preparation)

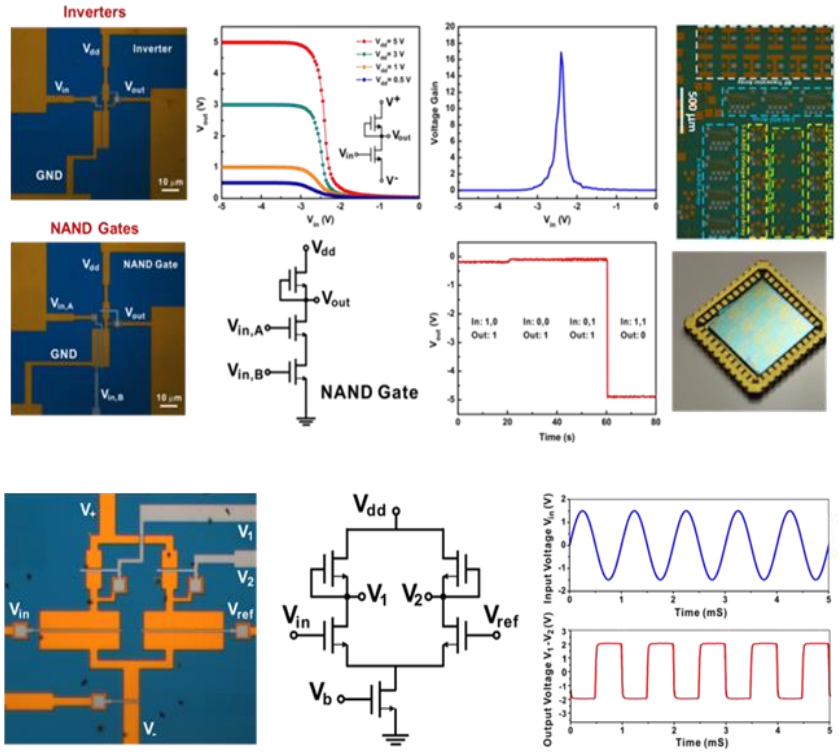

Electronic transport of CVD-MoS_2 Monolayer

W. Zhu, and YH Lee et. al., **Nat. Comm.** 5,3087 (2014)

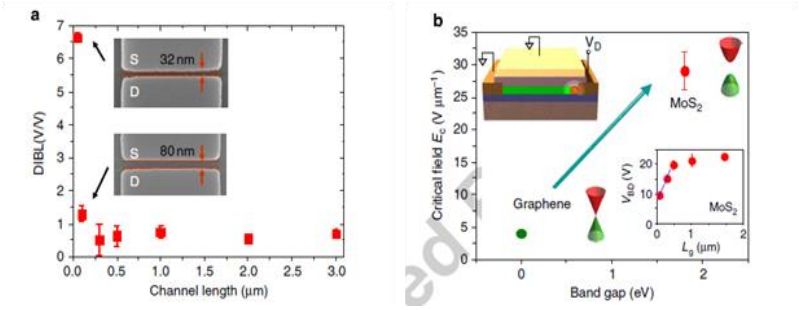

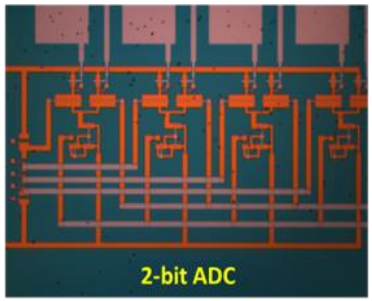

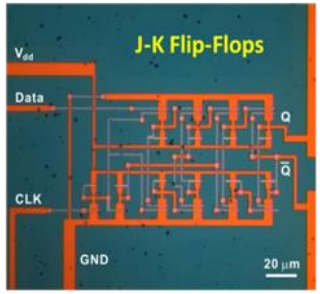

MoS_2 and WS_2 CVD growth

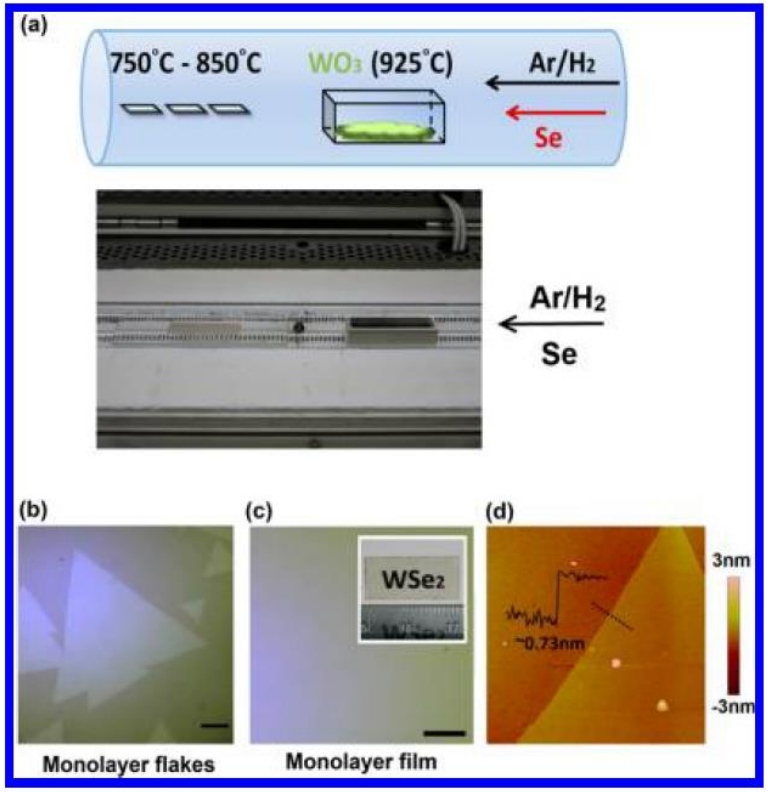

(a) Schematic illustration for the growth of WSe_2 layers on sapphire substrates by the reaction of WO_3 and Se powders in a CVD furnace. A photo of the setup is also shown.

(b) and (c) Optical microscopy images of the WSe_2 monolayer flakes and monolayer film grown at 850 and 750 C, respectively. Scale bar is 10 μm in length. The inset in (c) shows the photograph of a uniform monolayer film grown on a double side polished sapphire substrate.

(d) AFM image of a WSe_2 monolayer flake grown at 850 C on a sapphire substrate.

ACS Nano, 8, 923–930, (2014)

MoS_2 and WS_2 Lateral Epitaxy

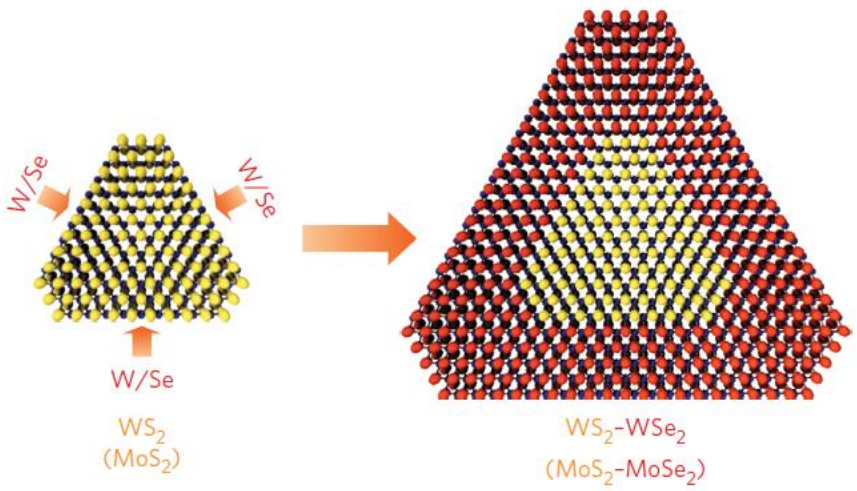

Schematic of lateral epitaxial growth of WS_2–WSe_2 and MoS_2–$MoSe_2$ heterostructures.

- A triangular domain of WS_2 (MoS_2) is first grown using a CVD process.
- The peripheral edges of the triangular domain feature unsaturated dangling bonds that function as the active growth front for the continued addition, and incorporation of precursor atoms to extend the two dimensional crystal in the lateral direction.

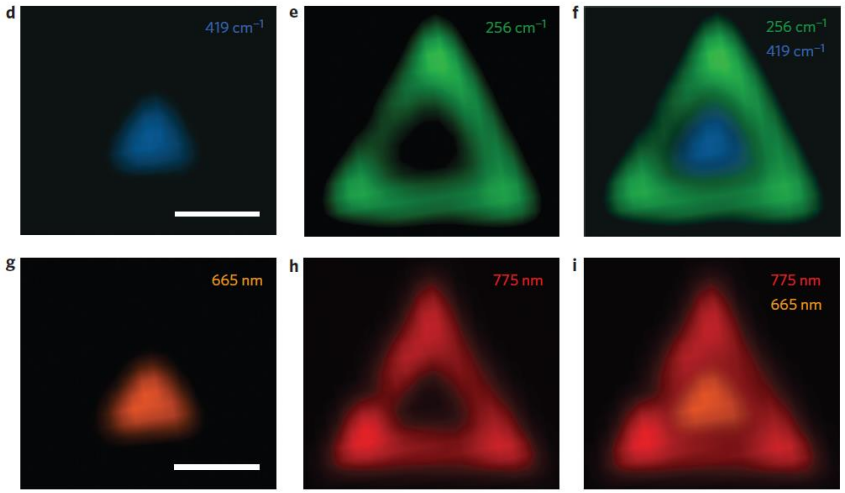

d, Raman mapping at 419 cm−1 (WS_2 A1g signal), demonstrating that WS_2 is localized at the center region of the triangular domain. e, Raman mapping at 256 cm−1 (WSe2 A1g signal), demonstrating that WSe_2 is located in the peripheral region of the triangular domain. f, Composite image consisting of Raman mapping at 256 cm−1 and 419 cm−1, showing no apparent overlap or gap between the WS_2 and WSe_2 signals, demonstrating that the WS_2 inner triangle and WSe_2 peripheral areas are laterally connected. g,h, hotoluminescence mapping images at 665 nm and 775 nm, showing characteristic photoluminescence emission of WS_2 and WSe_2 in the center and peripheral regions of the triangular domain, respectively. i, Composite image consisting of photoluminescence mapping at 665 nm and 775 nm, demonstrating the formation of WS_2–WSe_2 lateral heterostructures.

NATURE NANOTECHNOLOGY , VOL 9, 1024, (2014).

WSe_2-MoS_2 lateral p-n junction with an atomically sharp interface

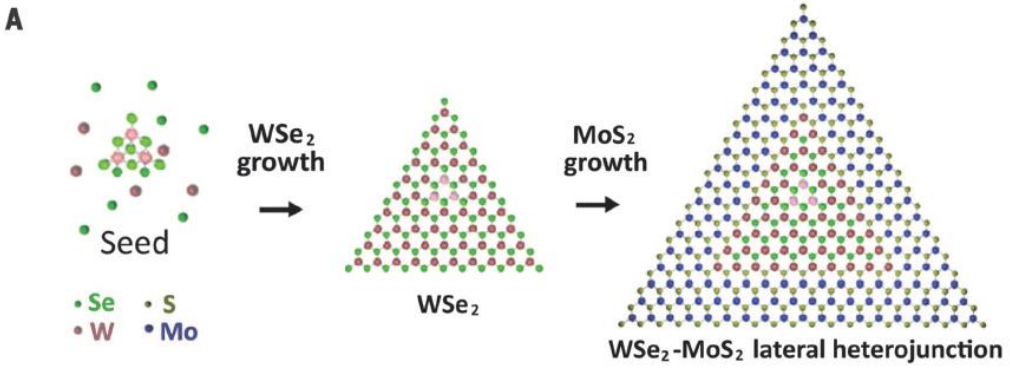

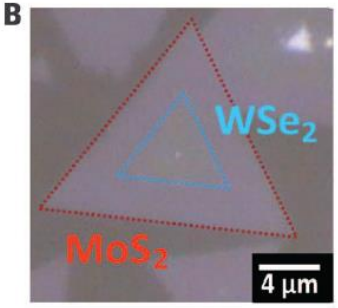

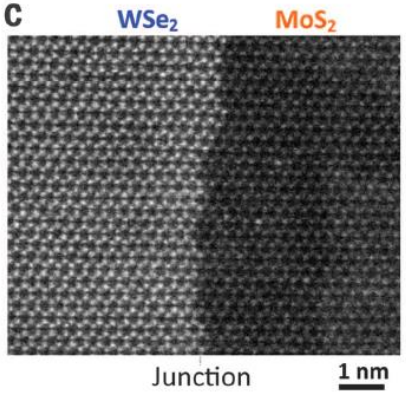

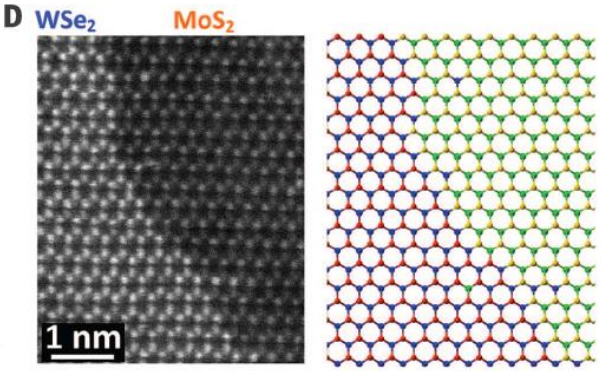

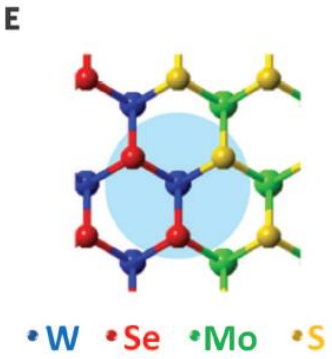

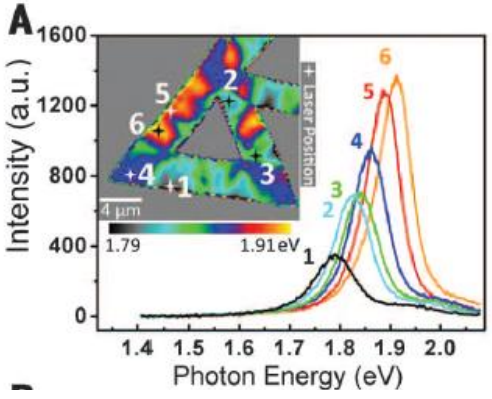

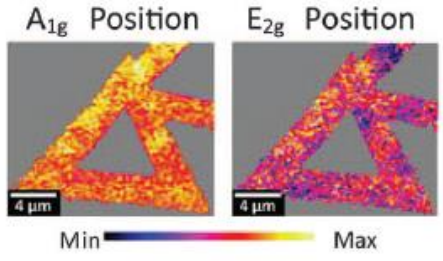

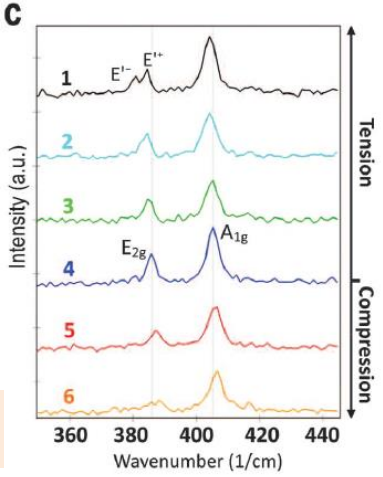

W. H. Chang, Science, 349, 524, (2015)

More on
2-D layered materials

Graphene-like
Series

Silicene, Germanene, Stanene, and more….

- To investigate the growth and characterizations of novel graphene-derived 2D materials, such as *silicene, germanene, stanene, borophene, bisumuthene, etc.* with the predicted gaps of 2, 24, and 100 meV, respectively for the first three.
- Stanene is recently predicted to be quantum spin Hall (QSH) insulator with a large bulk gap ~0.3 eV.
- Their QSH states can be effectively tuned by chemical functionalization and external strain, viable for low-power-consumption electronics.

Another emerging wonder material : Silicene

- Graphene-like 2-D silicon
- A finite band gap < 0.1V, more compatible with existing silicon-based electronics
- Potential application as a high-performance field effect transistor

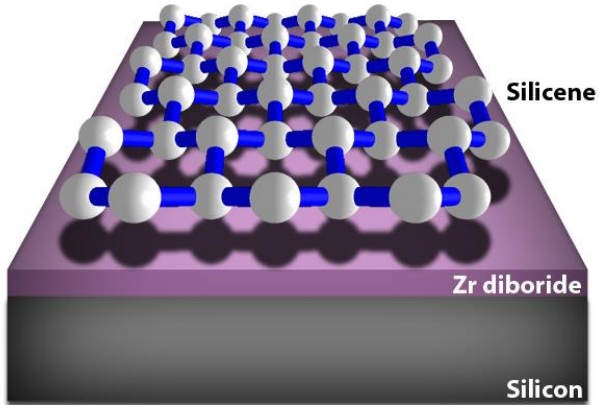

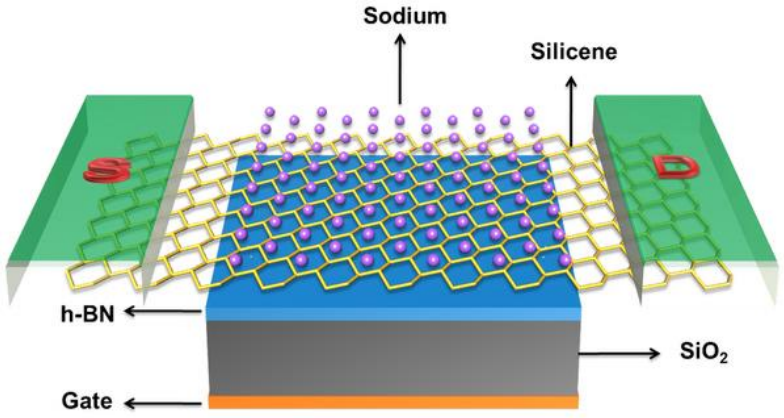

Nature, Scientific Reports **2**, # 853, 2012

To grow Silicene, Germanine, and even stanene on insulating or semiconducting substrate.

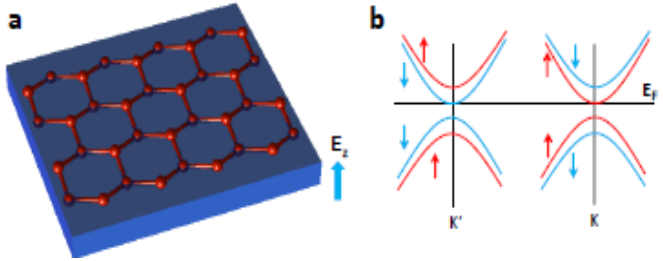

Superconductivity predicted in alkaline or alkaline earth elements doped silicene (CaC_6 T_c = 13K; $CaSi_6$ T_c = ?)

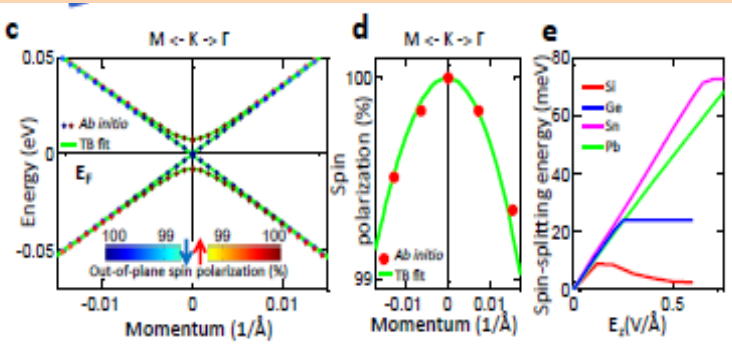

Silicene

- Via deposition of Si on Ag (111) at 450K -500K.
- B. Lalmi et al, APL (2010), and more.
- A buckled structure with a small gap of ~ 1.5 mV

Si/Ag(111)

$(2\sqrt{3} \times 2\sqrt{3})R30°$

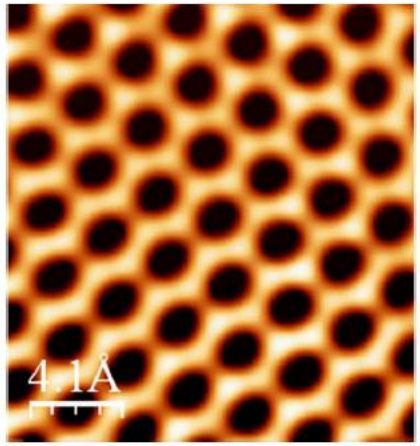

22x22 nm^2 , V=0,1 V , I=1,9 nA

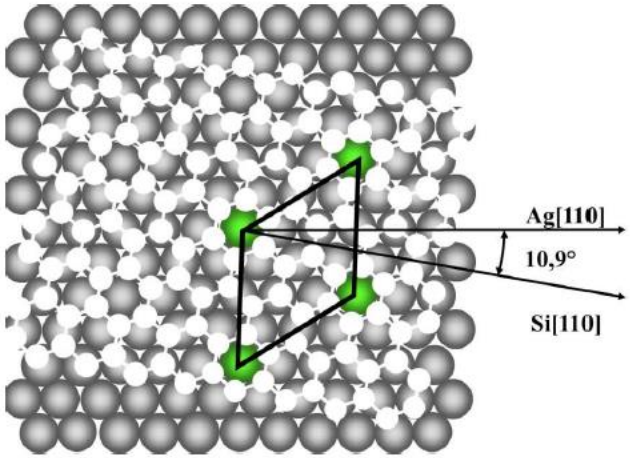

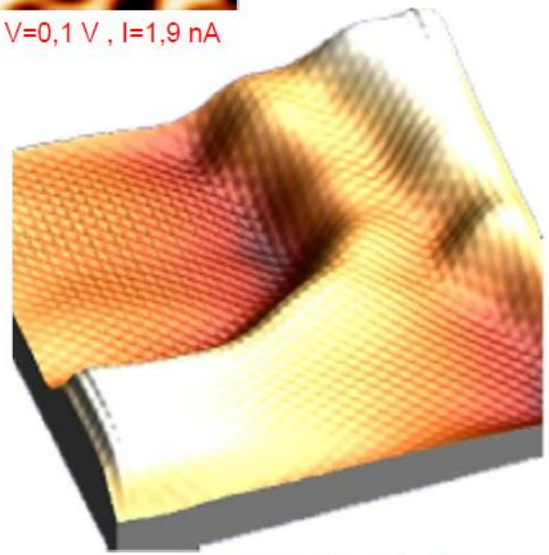

B. Lalmi etal, APL, 97, 223109 (2010)

Electronic properties (HRPES)

(4x4) superstructure

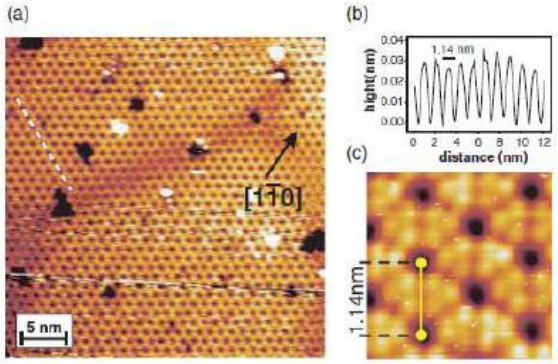

FIG. 2 (color). (a) Filled-states STM image of the 2D Si layer on Ag(111)-(1 × 1) ($U_{bias} = -1.3$ V, $I = 0.35$ nA). Clearly visible is the honeycomblike structure. (b) Line profile along the dashed white line indicated in (a). The dark centers in the STM micrograph are separated by 1.14 nm, corresponding to $\sqrt{3}$ times the Ag(111) lattice constant, in agreement with the (4 × 4) symmetry. (c) High-resolution STM topograph (3 × 3 nm, $U_{bias} = -1.3$ V, $I = 0.35$ nA) of the Si adlayer.

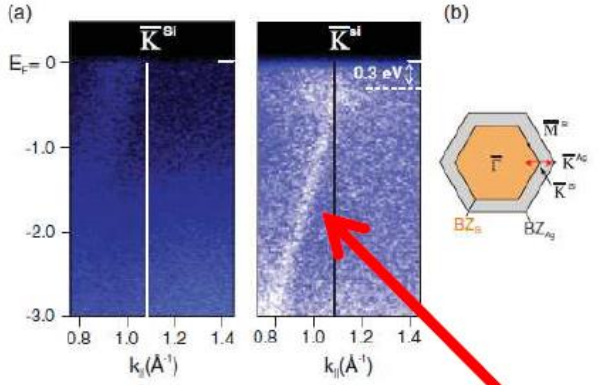

FIG. 3 (color). (a) ARPES intensity map for the clean Ag surface (left) and after formation of the 2D Si adlayer (right), taken along the Ag $\bar{\Gamma}$-$\bar{K}$ direction through the silicene $\bar{K}$($h\nu$ = 126 eV). (b) Brillouin-zone (BZ) scheme of the 2D Si layer with respect to the Ag(111)-(1 × 1) surface. The red arrow indicates the ARPES measurement direction.

Dirac cone

Linear dispesion

P. Vogt et al. PRL 108, 155501 (2012)

PHYSICAL REVIEW B 87, 245430 (2013)

Absence of a Dirac cone in silicene on Ag(111): First-principles density functional calculations with a modified effective band structure technique

Yun-Peng Wang and Hai-Ping Cheng*
Quantum Theory Project and Department of Physics, University of Florida, Gainesville, Florida 32611, USA
(Received 22 February 2013; revised manuscript received 3 April 2013; published 24 June 2013)

We investigate the currently debated issue of the existence of the Dirac cone in silicene on an Ag(111) surface, using first-principles calculations based on density functional theory to obtain the band structure. By unfolding the band structure in the Brillouin zone of a supercell to that of a primitive cell, followed by projecting onto Ag and silicene subsystems, we demonstrate that the Dirac cone in silicene on Ag(111) is destroyed. Our results clearly indicate that the linear dispersions observed in both angular-resolved photoemission spectroscopy [P. Vogt *et al.*, Phys. Rev. Lett. **108**, 155501 (2012)] and scanning tunneling spectroscopy [L. Chen *et al.*, Phys. Rev. Lett. **109**, 056804 (2012)] come from the Ag substrate and not from silicene.

No Dirac cone

???

Y. Peng et al. Phys. Rev. B. 87 245430 (2013)

Demonstration of Germanene:

Germanene grown on Ag (111)

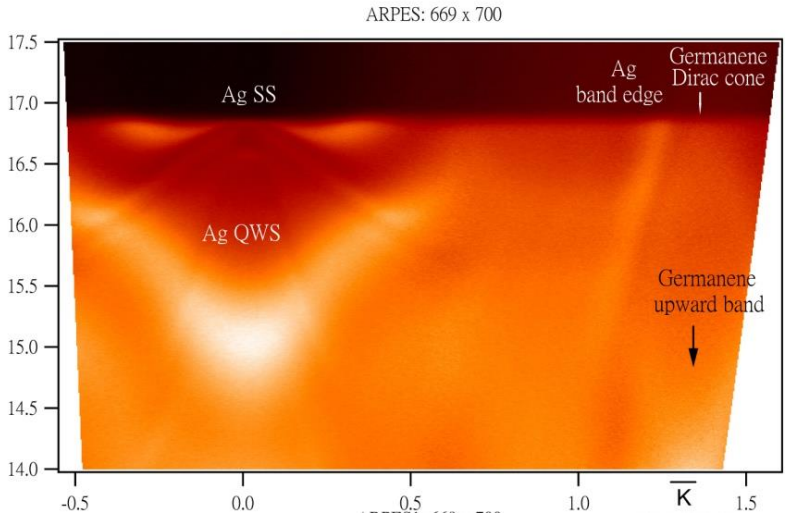

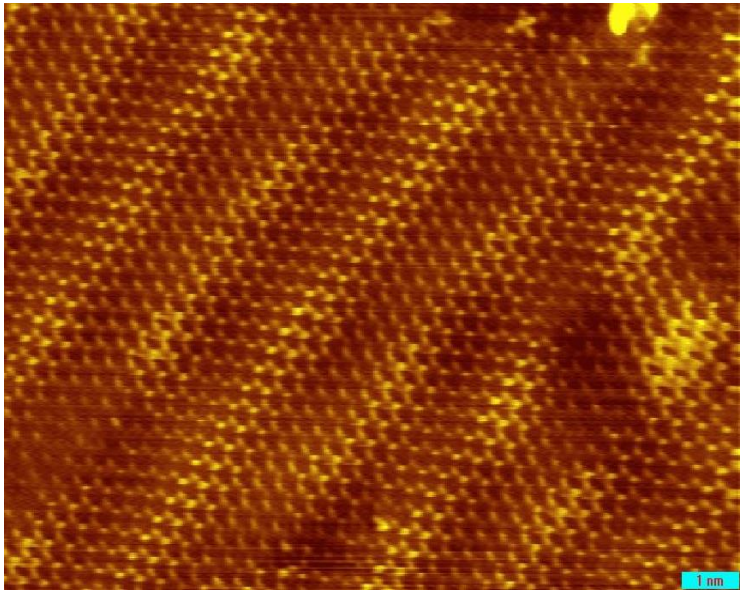

First observation of Dirac cone

First observation of "real" Honeycomb

Prof. Shu-jung Tang et al, NTHU, 2015
Phys. Rev. Materials **2**, 024003, 2018

- To grow silicene on 2D-MoS_2 ?
- To grow Germanene on 2D-MoS_2

YES!

However, it is metallic!

L. Zhang et al., Phys. Rev. Lett. 116, 256804 (2016)

Stanene

- Tin (*Sn*) with its large spin-orbit coupling offers rich electronic structures
- Predicted to exhibit highly efficient thermoelectrics, topological superconductivity, high-temperature quantum spin Hall, and quantum anomalous Hall effects.
- *Stanene could support a large gap (~ 0.3 V) 2-D quantum spin Hall (QSH) state, thus enable the dissipationless electric conduction at RT.*

Y. Xu *et al*. *PRL* **111**, 136804 (2013).

- Integrability with conventional semiconductor industry.

✓ With its elemental nature, *Sn* is free from the stoichiometry and related defects.

✓ *Sn* is commonly used in many group-IV MBE system and is easy to tackle.

- In this 2-D materials, outstanding properties: The Fermi velocity near Dirac point approaches 7.3×10^5 m/s, much larger than that of typical 3-D TI, and close to that of graphene (1×10^6 m/s).
- stanene/Bi_2Te_3 crystal structure

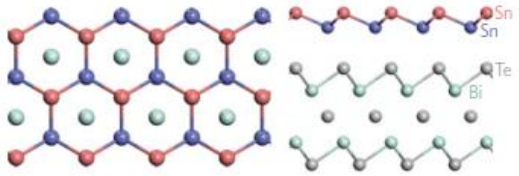

F. Zhu *et al*. *Nature Materials,* **14**, 1020–1025 (2015).

- α-Sn film was grown on *InSb*(001) as a 3-D TI, with nearly massless electron dispersion with a bulk bandgap of 230 mV, showing spin helical band by ARPES.
- One monolayer (111) orientated α- *Sn* is a *buckled*-honeycomb structure, similar to graphene.

Stanene grown on $Bi_2Te_3(111)$

- Monolayer stanene was fabricated by MBE on $Bi_2Te_3(111)$ substrate.
- Obvious discrepancies :

--According to ARPES, the valence bands of stanene are pinned in the conduction band of $Bi_2Te_3(111)$, giving metallic interface states. The inverted bandgap at **Γ** point, the key to QSH state, was not observed.

--Dirac-cone-like features at K point are expected in a honeycomb structure, stanene with a larger SOC, leads to a bandgap of 0.1 eV at the Dirac-cone. However, Dirac-cone at the **K**-point of stanene /$Bi_2Te_3(111)$ was not observed.

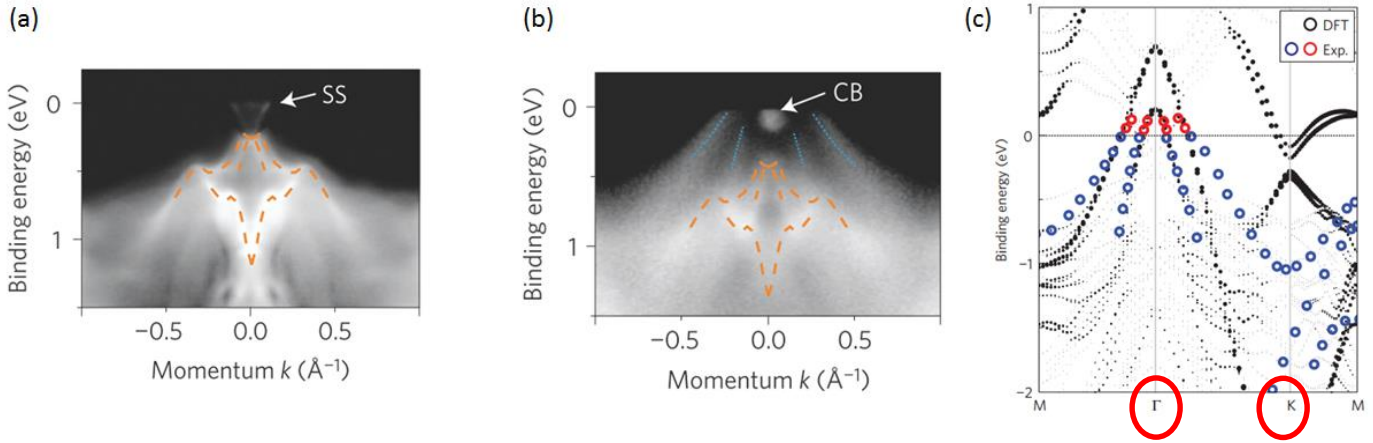

F. Zhu *et al*. *Nature Materials,* **14**, 1020–1025 (2015).

(a) ARPES spectra of $Bi_2Te_3(111)$, (b) stanene on Bi_2Te_3 along K-Γ-K direction. The orange dashed lines mark the bulk band dispersions of Bi_2Te_3. The blue dotted lines mark the hole band of stanene. SS marks the surface state and CB marks the conduction band of Bi_2Te_3. (c) Comparison of experimental results with DFT calculation of stanene/Bi_2Te_3. Red dots above the Fermi level are obtained by *in-situ* potassium deposition that provides the film with electrons.

Progress on Stanene

- Discover superconductivity in few-layer stanene down to a bilayer grown on PbTe, while bulk α-tin is not superconductive.

  a trilayer stanene on top of $PbTe/Bi_2Te_3/Si(111)$

- Stanene on Cu(111) by low-T MBE. Discovered an unusually flat stanene showing an *in-plane s–p* band inversion with a SOC-induced topological gap (~0.3 eV) at the Γ point, which represents a group-IV graphene-like material displaying topological features.

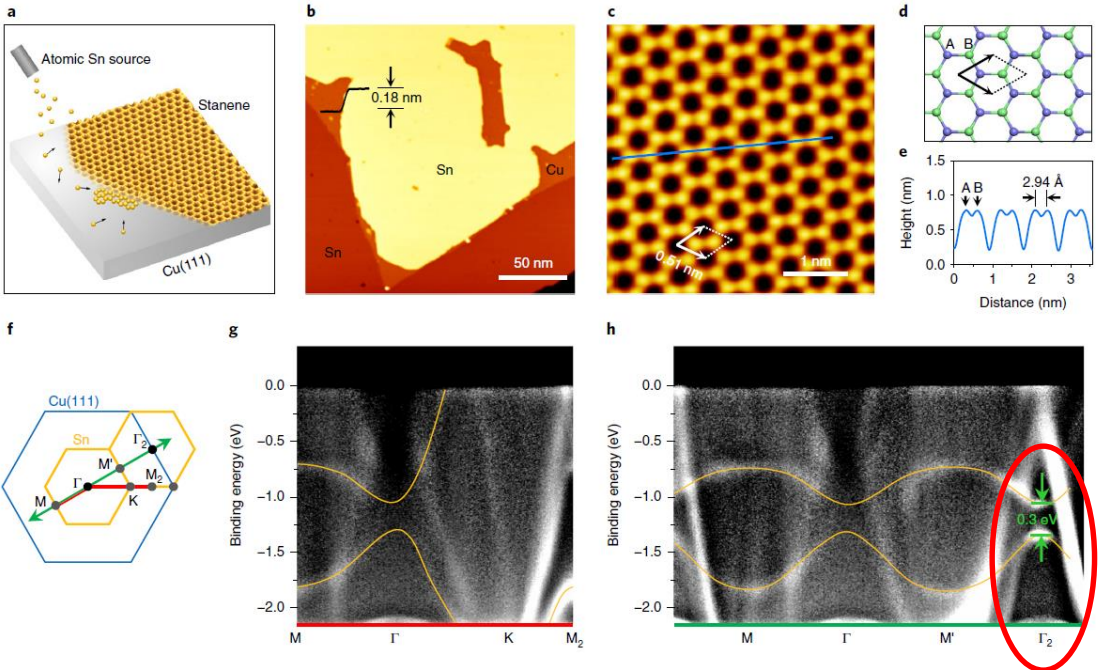

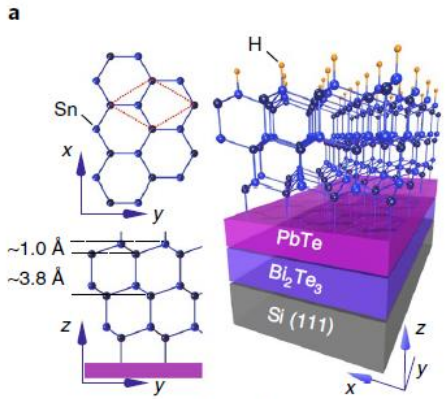

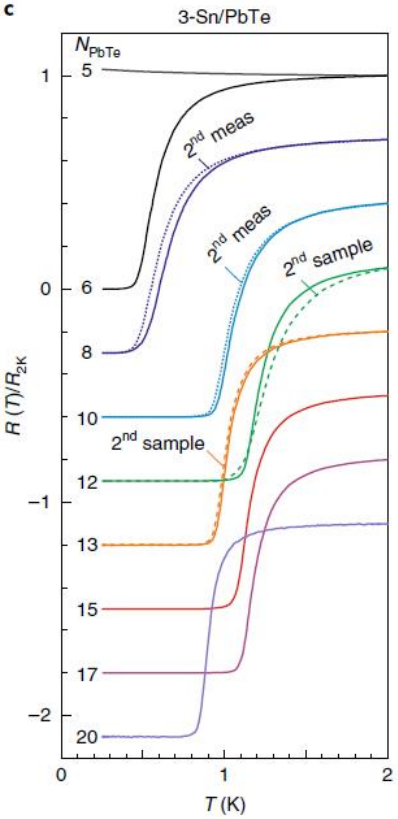

Nature Physics, 14, 344, (2018).

Nature Materials, 17, 1081, (2018).

Borophene

The β_{12} sheet, a borophene structure that can form spontaneously on a Ag(111) surface.

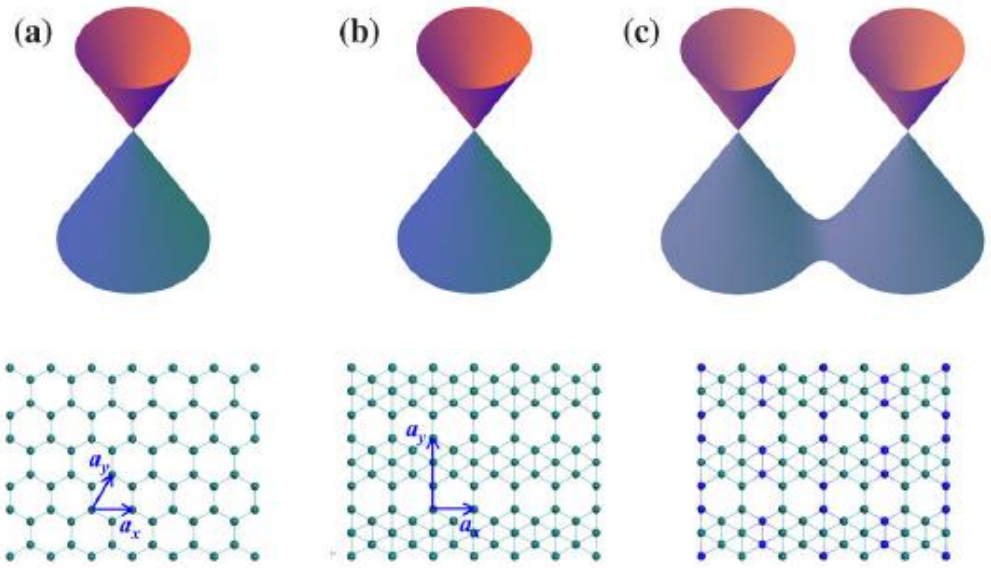

FIG. 1. Schematic drawing of the Dirac cones and lattices. (a) Honeycomb structure. (b) β_{12} sheet. (c) The β_{12} sheet with a 3×1 perturbation. The blue and green balls indicate the boron atoms with different on-site energies in our TB analysis. The top and bottom panels are the band structures and atomic structures, respectively. The basic vectors of the primitive unit cell are indicated by the blue arrows.

I. Matsuda group, PRL, 118, 096401 (2017).

Phosphorene

- Black phosphorus, *phosphorene* is one of three different crystal structures that pure phosphorus can adopt.
- White phosphorus is used in making fireworks.
- Red phosphorus is used to make the heads of matches.
- The bandgap is adjusted by varying the number of phosphorene layers stacking one atop another, significantly larger than the bulk value of 0.31- 0.36 eV.
- Much easier to engineer devices with the exact behavior desired.
- Mobility ~ 600
- Unstable in air.
- Passivated by Al_2O_3 layer and teflon.
- Harnessing phosphorene's higher electron mobility for making electronic devices.

Phosphorene

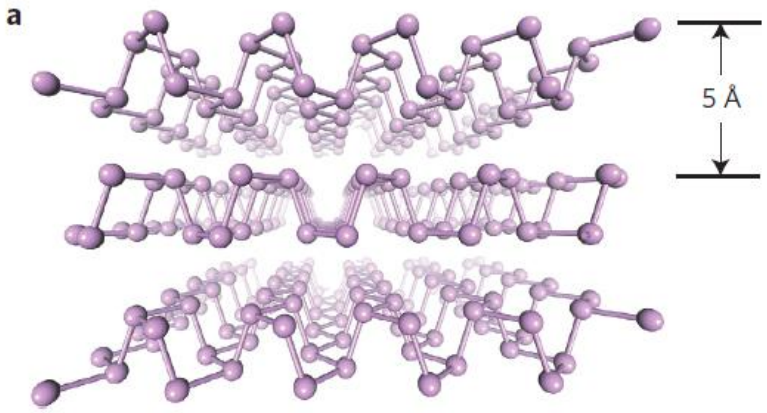

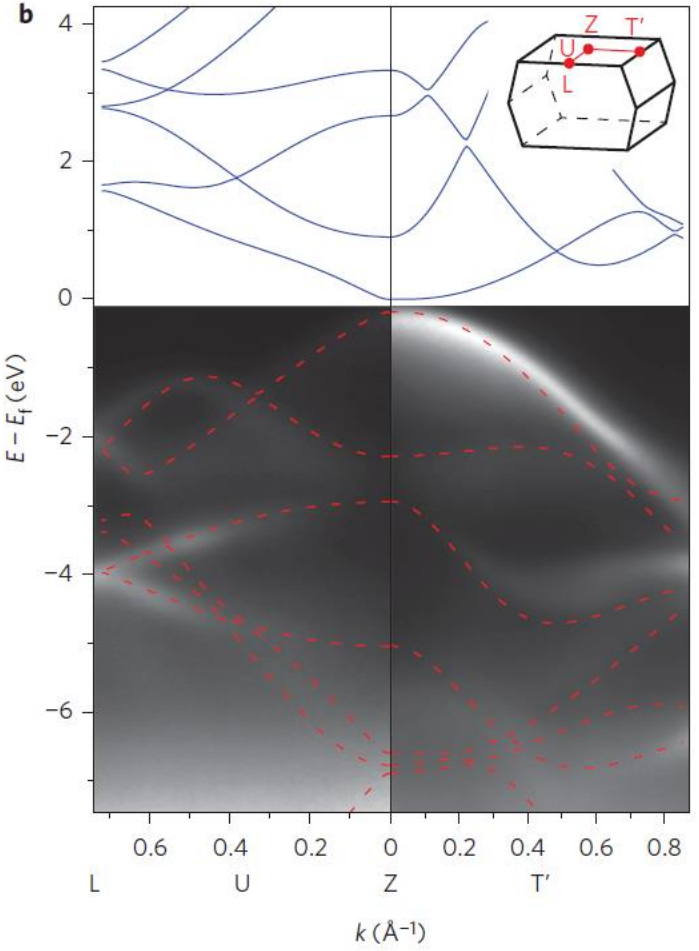

- Black phosphorus was synthesized under a constant pressure of 10 kbar by heating red phosphorus to 1,000 C .
- Then slowly cooling to 600 C at a cooling rate of 100 C per hour.

YB Zhang, Fudan Univ. NATURE NANOTECHNOLOGY | VOL 9 | MAY 2014 | , 372.

Phosphorene

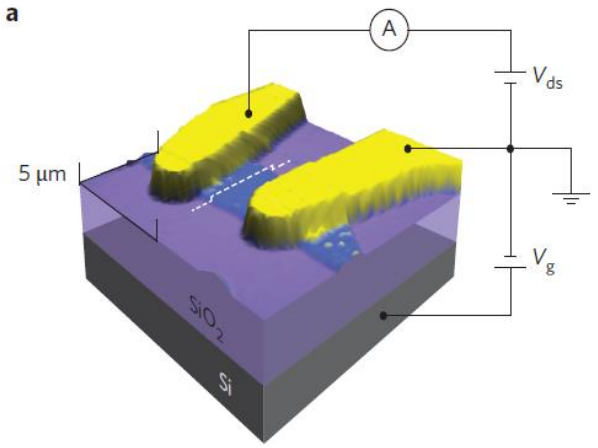

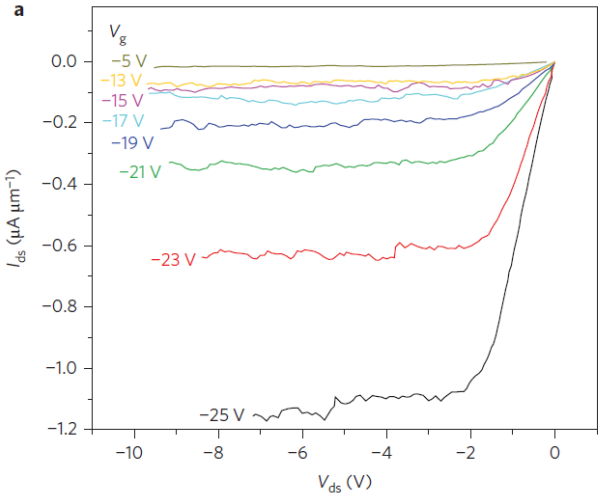

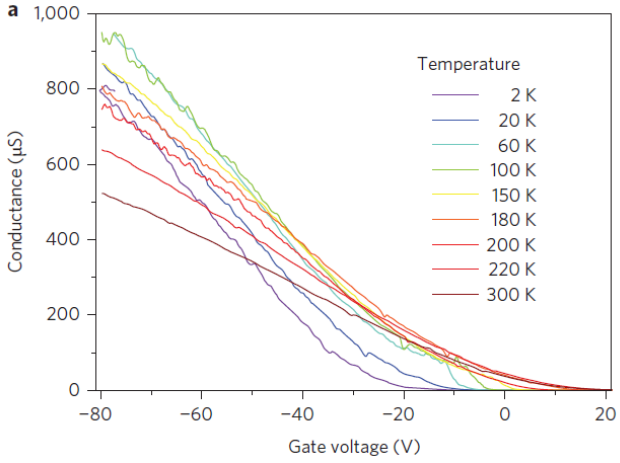

- Reliable transistor performance is achieved at room temperature in samples thinner than 7.5 nm. Channel length and width of the device are 1.6 mm and 4.8mm.
- **Field-effect mobility** (red open circles), and **Hall mobility** (filled squares, three different values of n) as a function of temperature on a logarithmic scale
- $$\mu_{FE} = \frac{L}{W}\frac{1}{C_g}\frac{dG}{d(V_g - V_{th})} \qquad \mu_H = \frac{L}{W}\frac{G}{ne}$$

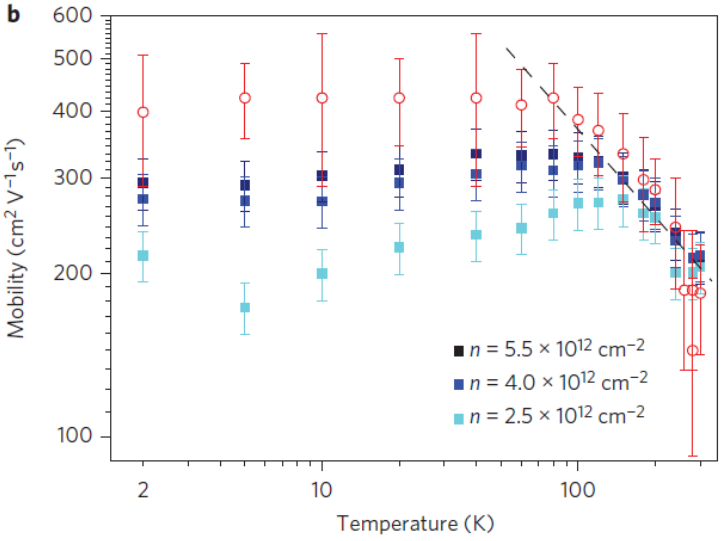

Phosphorene

- fabricating *p*-type FETs based on few-layer phosphorene.
- exhibit ambipolar behavior with drain current modulation up to 10^5,
- a field-effect mobility to 1,000 $cm^2\ V^{-1}\ s^{-1}$ at room temperature, and thickness dependent.

YB Zhang, Fudan Univ, NATURE NANOTECHNOLOGY | VOL 9 | MAY 2014 | , 372.

Tomanek at Michigan State, and Peter Ye at Purdue reported phosphorene-based transistors, along with simple circuits. ACS Nano, **8** (4), 4033–4041, (2014).

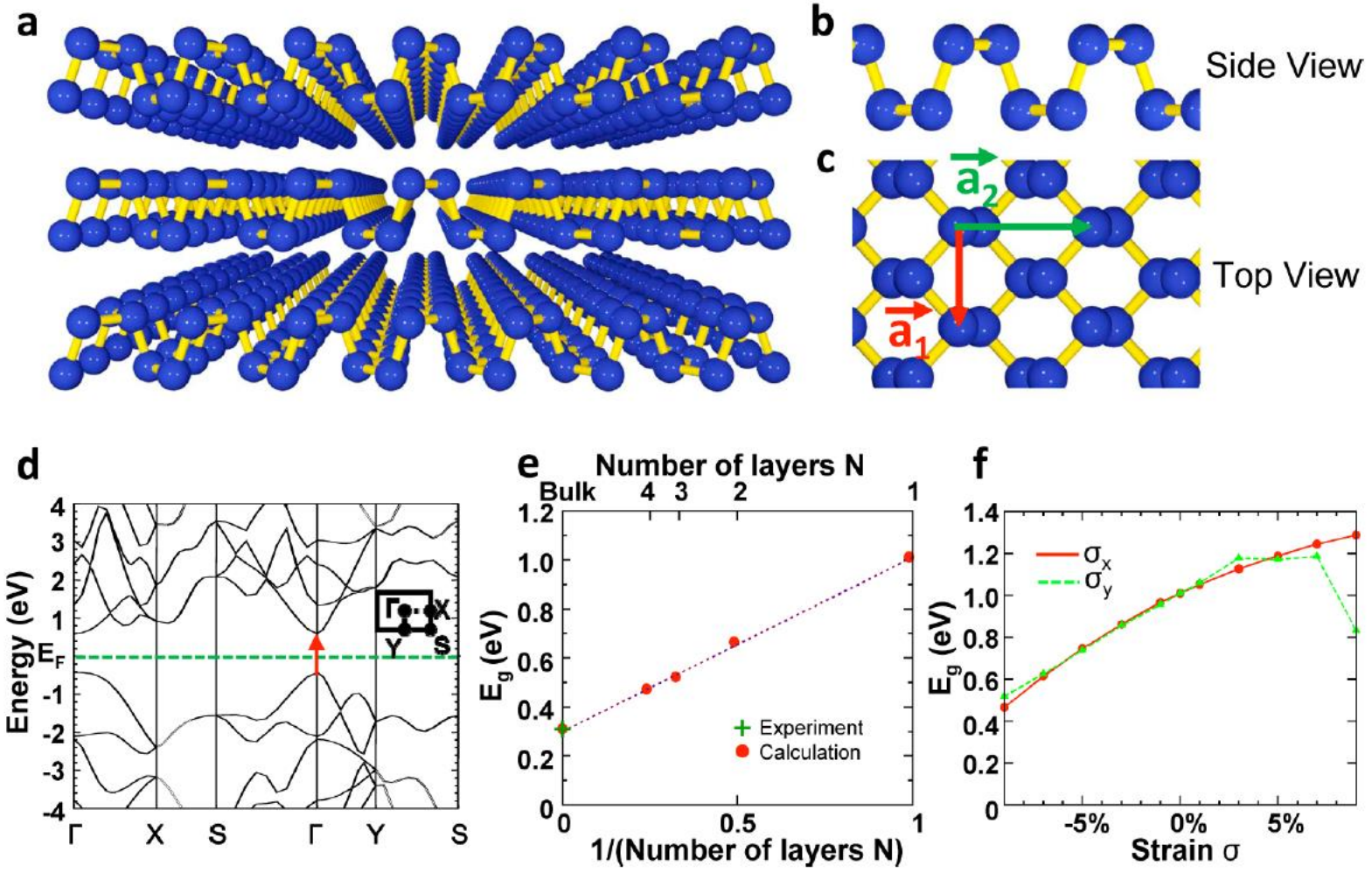

Figure 1. Crystal structure and band structure of few-layer phosphorene. (a) Perspective side view of few-layer phosphorene. (b,c) Side and top views of few-layer phosphorene. (d) DFT-HSE06 band structure of a phosphorene monolayer. (e,f) DFT-HSE06 results for the dependence of the energy gap in few-layer phosphorene on (e) the number of layers and (f) the strain along the *x*- and *y*-direction within a monolayer. The observed band gap value in the bulk is marked by a cross in (e).

Phosphorene-based field effect transistors

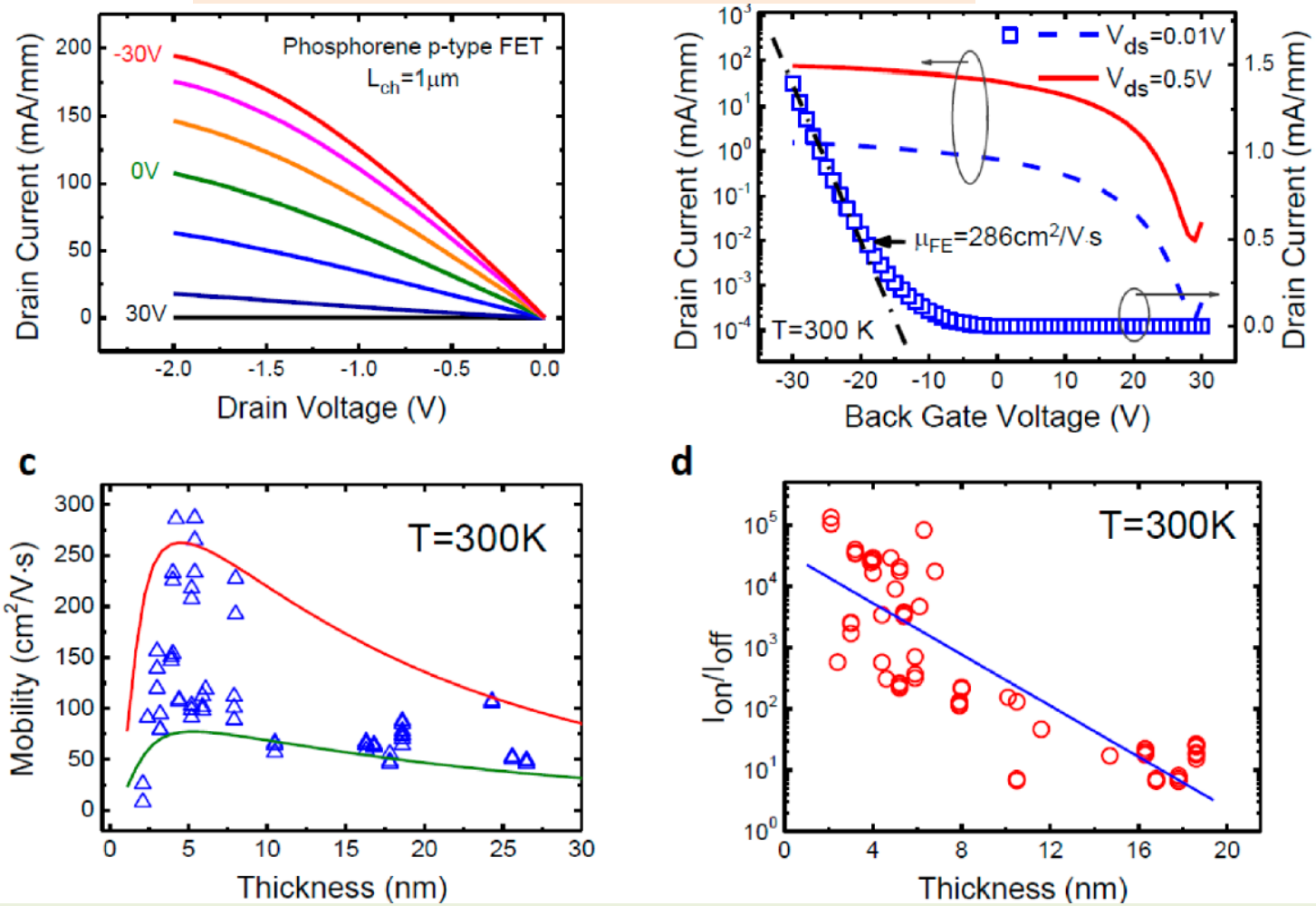

- Tomanek and Ye reported to have made phosphorene-based transistors, along with simple circuits. ACS Nano, 8 (4), 4033–4041, (2014).
- A few-layer phosphorene FET with 1.0 μm channel length displays (a, b) high on-current of 194 mA/mm, (c) high hole field-effect mobility of 286 $cm^2V^{-1}.s^{-1}$,(d) an on/off ratio of 10^4.
- Constructed **a CMOS inverter** by a phosphorene *p*-MOS transistor and a MoS_2 *n*-MOS transistor.

Bismuthene

- Quantum spin Hall materials with dissipationless spin currents required cryogenic temperatures owing to small energy gaps.
- A room-temperature regime with a large energy gap may be achievable that exploits the atomic spin-orbit coupling (SOC).
- The concept is based on a substrate-supported monolayer of a high–atomic number element, and is realized as a bismuth honeycomb lattice on top of the insulating substrate SiC(0001). Using STS, a gap of ~0.8 eV and conductive edge states are detected, consistent with theory.

Reis et al., Science **357**, 287–290 (2017)

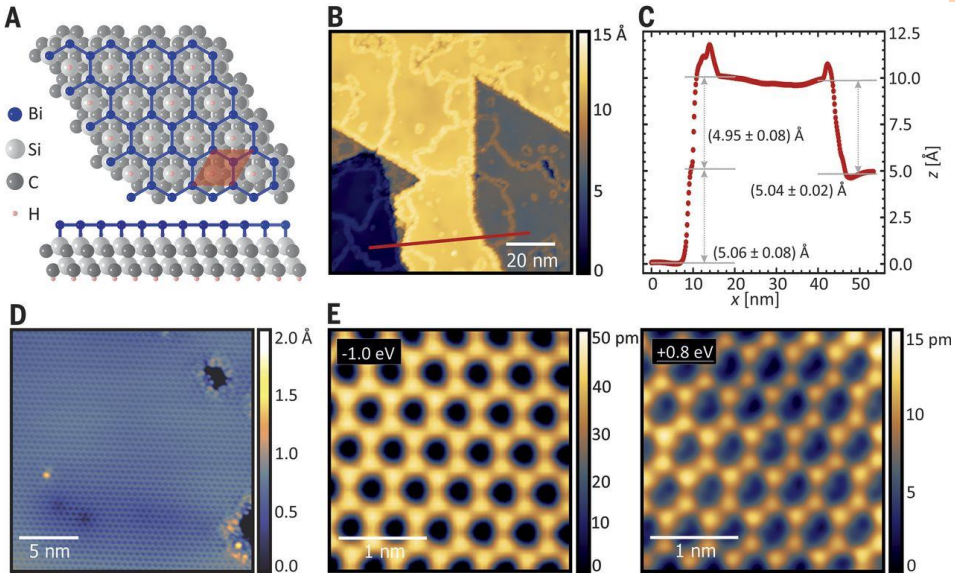

Fig. 1 Bismuthene on SiC(0001) structural model. (A) Sketch of a bismuthene layer placed on the threefold-symmetric SiC(0001) substrate in Embedded Image commensurate registry. (B) Topographic STM overview map showing that bismuthene fully covers the substrate. The flakes are of ~25-nm extent, limited by domain boundaries. (C) Substrate step-height profile, taken along the red line in (B). The step heights correspond to SiC steps. (D) The honeycomb pattern is seen on smaller scan frames. (E) Close-up STM images for occupied and empty states (left and right panels, respectively). They confirm the formation of Bi honeycombs.

Bismuthene

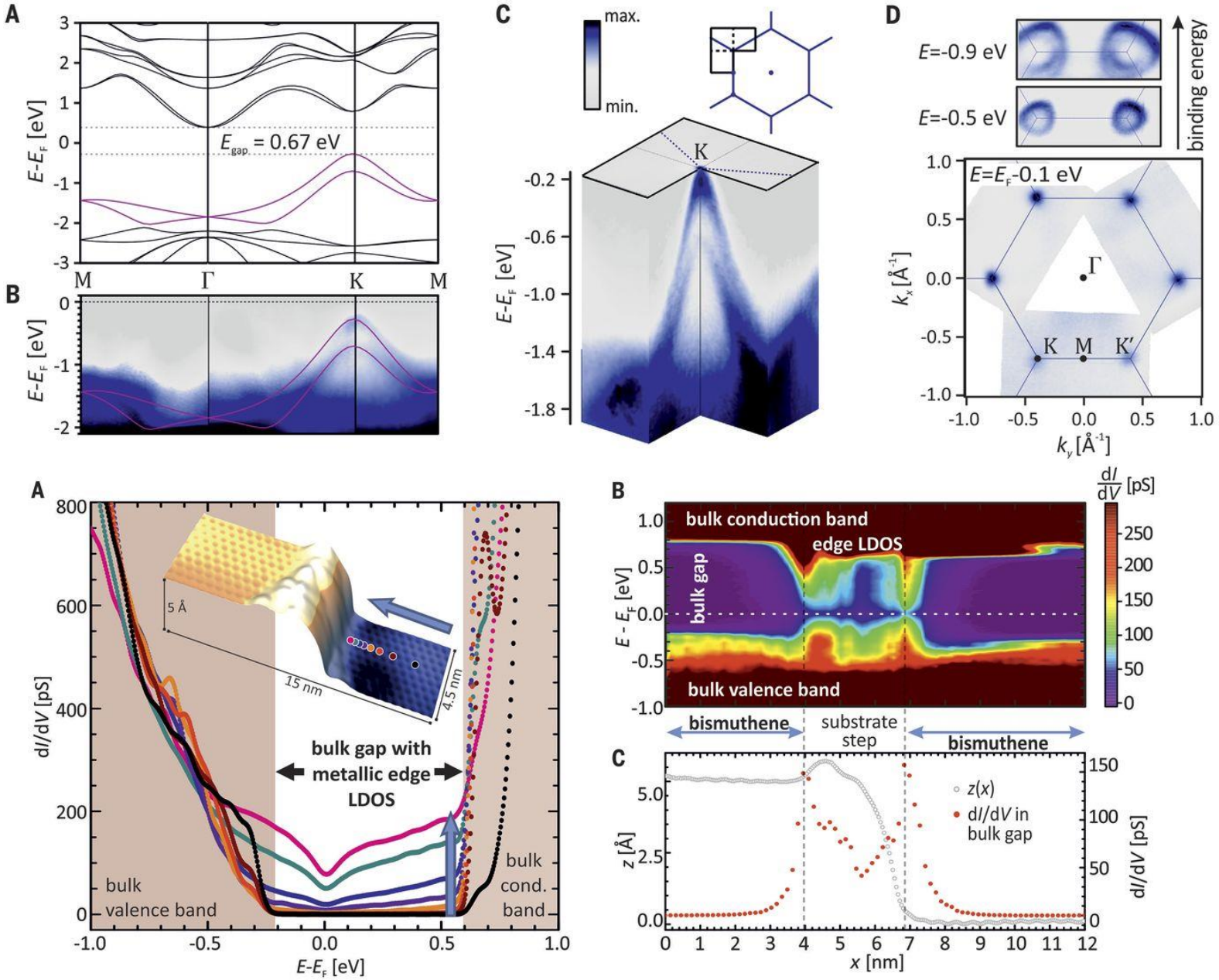
A
B
C
D
E-E_F [eV]
E_{gap} = 0.67 eV
M
Γ
K
M
max.
min.
K
E=-0.9 eV
E=-0.5 eV
binding energy
E=E_F-0.1 eV
Γ
K M K′
k_x [Å^{-1}]
k_y [Å^{-1}]
A
B
dI/dV [pS]
5 Å
15 nm
4.5 nm
bulk gap with
metallic edge
LDOS
bulk
valence band
bulk
cond.
band
E-E_F [eV]
bulk conduction band
edge LDOS
bulk gap
bulk valence band
E - E_F [eV]
dI/dV [pS]
bismuthene
substrate
step
bismuthene
C
z(x)
dI/dV in
bulk gap
z [Å]
dI/dV [pS]
x [nm]

Twisted Graphene

Twistronics

Twisted graphene

- The behavior of ***strongly correlated*** materials, and in particular unconventional superconductors, has been studied for decades, but is still not well understood.
- Prof. Pablo Jarillo-Herrero and his student Yuan Cao of MIT discovered in 2018 that superconductivity existed in twisted bilayer graphene. For twist angles of about 1.1°—forming a Moire pattern at 1.7K, the electronic band structure of this 'twisted bilayer graphene' exhibits flat bands near zero Fermi energy, resulting in **correlated insulating states at half-filling**.
- Upon electrostatic doping of the material away from these correlated insulating states, they observed tunable zero-resistance states with a $\mathbf{T_c}$ up to **1.7K**.
- Twisted bilayer graphene is thus a precisely tunable, purely carbon-based, 2-D superconductor. It is therefore an ideal material for investigations of strongly correlated phenomena.
- They also found the addition of BN between the two graphene layers, **orbital magnetism** was produced at the magic angle of 1.17°. Spectroscopic study showed strong electron–electron correlation at this magic angle.

Moire Pattern

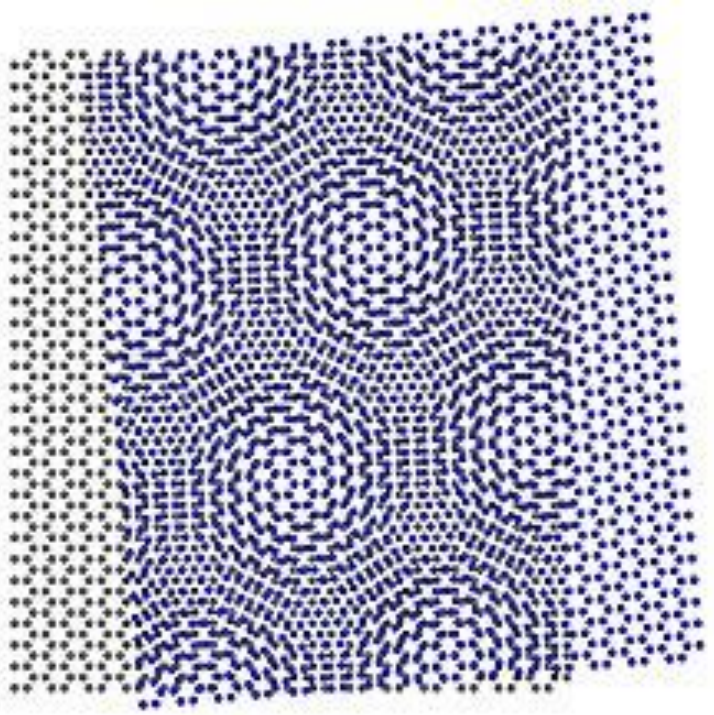

Yuan Cao et al,
Nature **556**, 43–50 (2018).

Nature **556**, 80–84 (2018).

2-D Hetero-structures and applications

- 2-D materials offer stacked like cards in a deck to create the different electronic layers as needed in functional electronic devices. Van der Waals bonding
- Because they do not form tight bonds with the layers above and below.
- Ye's group at Purdue reported to use both MoS_2 and phosphorene to make ultrathin photovoltaics (PVs).
- Geim et al reported in Nature Materials to have assembled multiple 2D materials to make efficient thin LEDs.
- Revolution in electronics and optics just began.
- Flexible, transparent, temperature stable, and cheap to manufacture

Van der Waals heterostructures

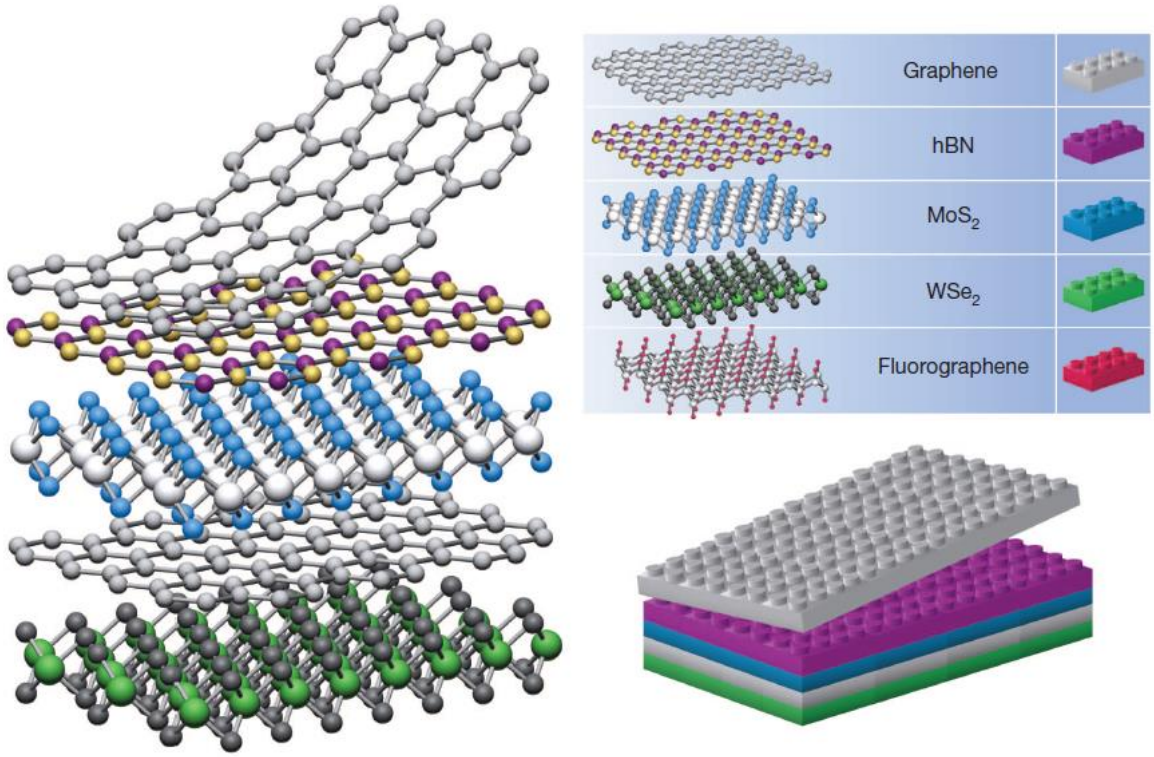

Building van der Waals Heterostructures:

If one considers 2D crystals to be analogous to Lego blocks (right panel), the construction of a huge variety of layered structures becomes possible.

Conceptually, this atomic scale Lego resembles molecular beam epitaxy, but employs different 'construction' rules and a distinct set of materials.

25 JULY 2013 | VOL 499 | NATURE | 419

Current 2D library

- Monolayers proved to be stable under room temperature in air are shaded **blue**;
- Those probably stable in air are shaded **green**;
- Those unstable in air but that may be stable in inert atmosphere are shaded **pink**.
- **Grey** shading indicates 3D compounds that have been successfully exfoliated down to monolayers.
- We note that, after intercalation and exfoliation, the oxides and hydroxides may exhibit stoichiometry different from their 3D parents.

<table>
<tr><td>Graphene family</td><td>Graphene</td><td colspan="2">hBN
'white graphene'</td><td>BCN</td><td>Fluorographene</td><td>Graphene oxide</td></tr>
<tr><td rowspan="2">2D chalcogenides</td><td colspan="2" rowspan="2">MoS_2, WS_2, $MoSe_2$, WSe_2</td><td colspan="2" rowspan="2">Semiconducting dichalcogenides:
$MoTe_2$, WTe_2,
ZrS_2, $ZrSe_2$ and so on</td><td colspan="2">Metallic dichalcogenides:
$NbSe_2$, NbS_2, TaS_2, TiS_2, $NiSe_2$ and so on</td></tr>
<tr><td colspan="2">Layered semiconductors:
GaSe, GaTe, InSe, Bi_2Se_3 and so on</td></tr>
<tr><td rowspan="2">2D oxides</td><td>Micas,
BSCCO</td><td colspan="2">MoO_3, WO_3</td><td rowspan="2" colspan="2">Perovskite-type:
$LaNb_2O_7$, $(Ca,Sr)_2Nb_3O_{10}$,
$Bi_4Ti_3O_{12}$, $Ca_2Ta_2TiO_{10}$ and so on</td><td>Hydroxides:
$Ni(OH)_2$, $Eu(OH)_2$ and so on</td></tr>
<tr><td>Layered
Cu oxides</td><td colspan="2">TiO_2, MnO_2, V_2O_5,
TaO_3, RuO_2 and so on</td><td>Others</td></tr>
</table>

State-of-the-art van der Waals structures and devices

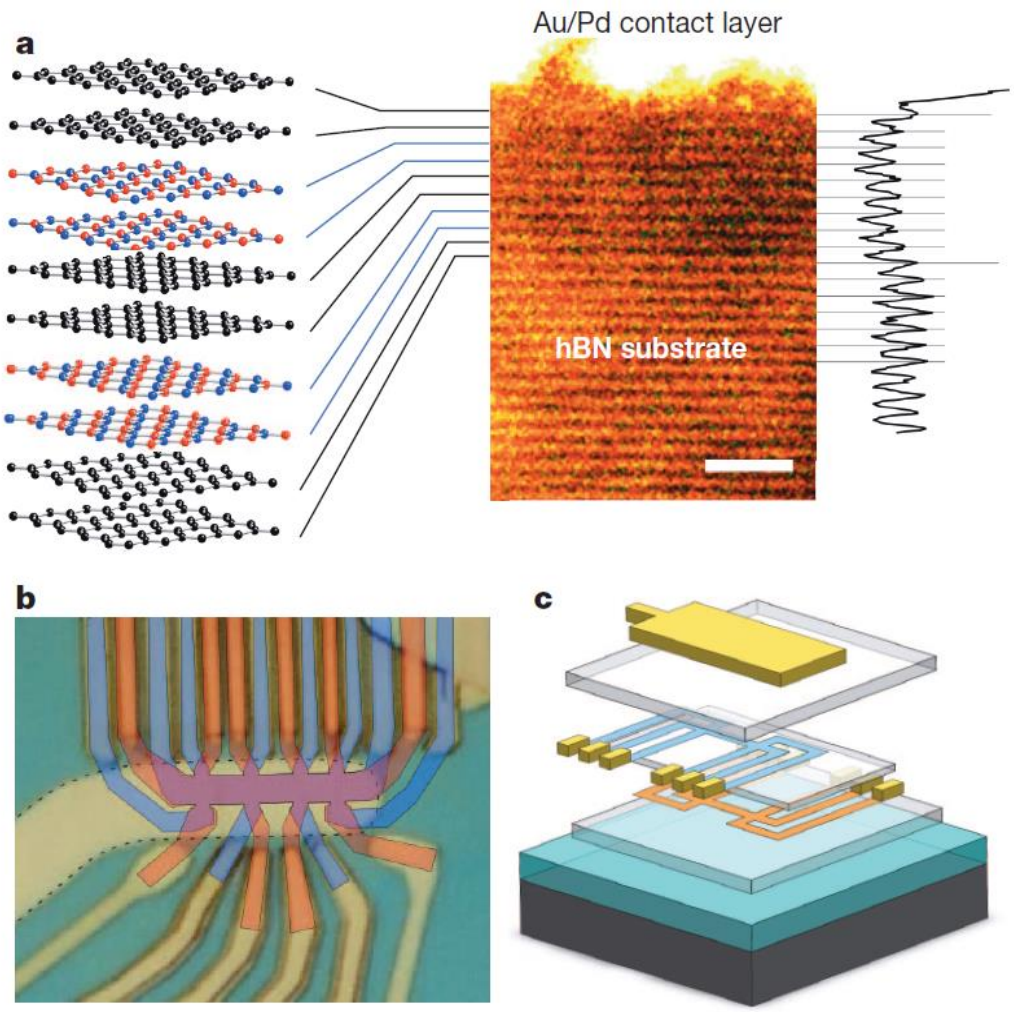

a, Graphene–hBN superlattice consisting of **six** stacked bilayers. On the right its cross-section and intensity profile as seen by scanning transmission electron microscopy are shown; on the left is a schematic view of the layer sequence. The topmost **hBN** bilayer is not visible, being merged with the metallic contact.

b, c, Double-layer graphene heterostructures. An optical image of a working device (b), and its schematics in matching colors (c). Two graphene Hall bars are accurately aligned, separated by a trilayer hBN crystal and encapsulated between relatively thick hBN crystals (hBN is shown in c as semitransparent slabs). The entire heterostructure is placed on top of an oxidized Si wafer (SiO_2 is in turquoise). The colors in b indicate the top (blue) and bottom(orange) Hall bars and their overlapping region (violet). The graphene areas are invisible in the final device image because of the top Au gate outlined by dashes. The scale is given by the width of the Hall bars, 1.5 μm.

25 JULY 2013 | VOL 499 | NATURE | 419

Heterostructure devices with SQW and MQWs by band structure engineering

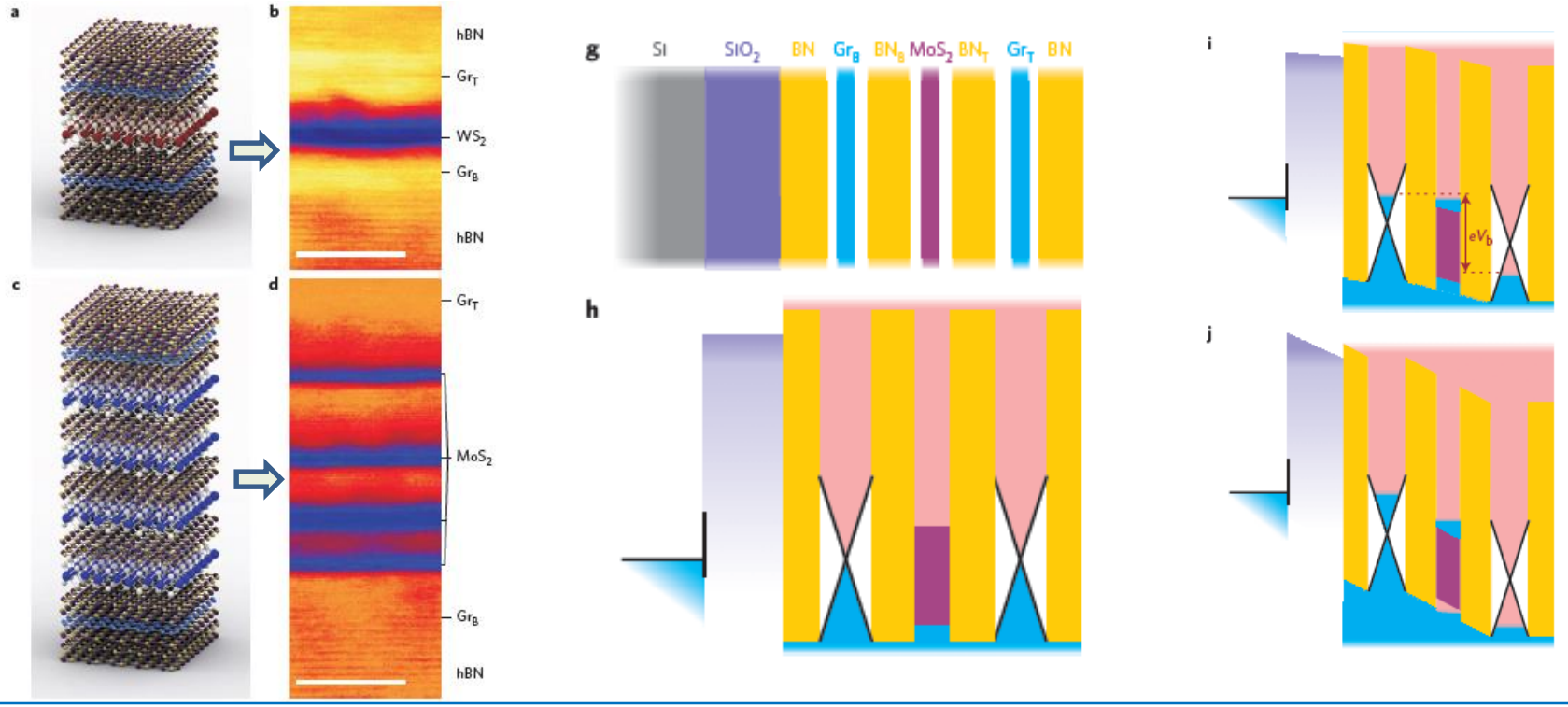

a. Schematic of the SQW heterostructure: $hBN/Gr_B/2hBN/WS_2/2hBN/Gr_T/hBN$.

b. Cross-sectional bright-field STEM image of the type of heterostructure presented in **a**. Scale bar, 5 nm.

c.d. Schematic and STEM image of the MQW heterostructure: $hBN/Gr_B/2hBN/MoS_2/2hBN/MoS_2/2hBN/MoS_2/2hBN/MoS_2/2hBN/Gr_T/hBN$. The number of hBN layers between MoS_2 QWs in **d** varies. Scale bar, 5 nm.

g. Schematic of the heterostructure $Si/SiO_2/hBN/Gr_B/3hBN/MoS_2/3hBN/Gr_T/hBN$.

h–j. Band diagrams for (**h**) the case of zero applied bias; (**i**) intermediate applied bias; and (**j**) high bias for the heterostructure presented in **g**.

NATURE MATERIALS | VOL 14 | 301, 2015

Ferromagnetism in 2-D materials

- In 2-D systems, long-range magnetic order is strongly suppressed by thermal fluctuations, according to the Mermin-Wagner theorem.
- These thermal fluctuations can be counteracted by magnetic anisotropy.

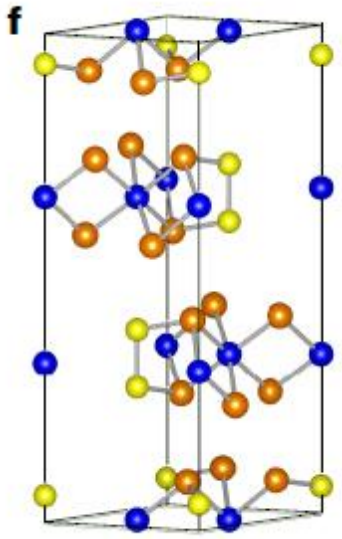

$CrGeTe_3$ with T_c of 70K

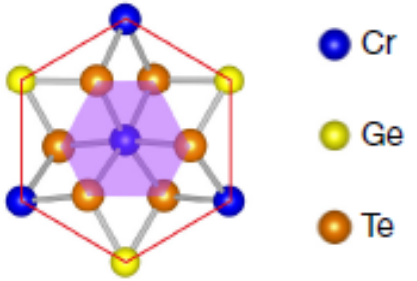

Xiang Zhang group of UC Berkeley

C. Gong et al., *Nature* **546**, 265 (2017).

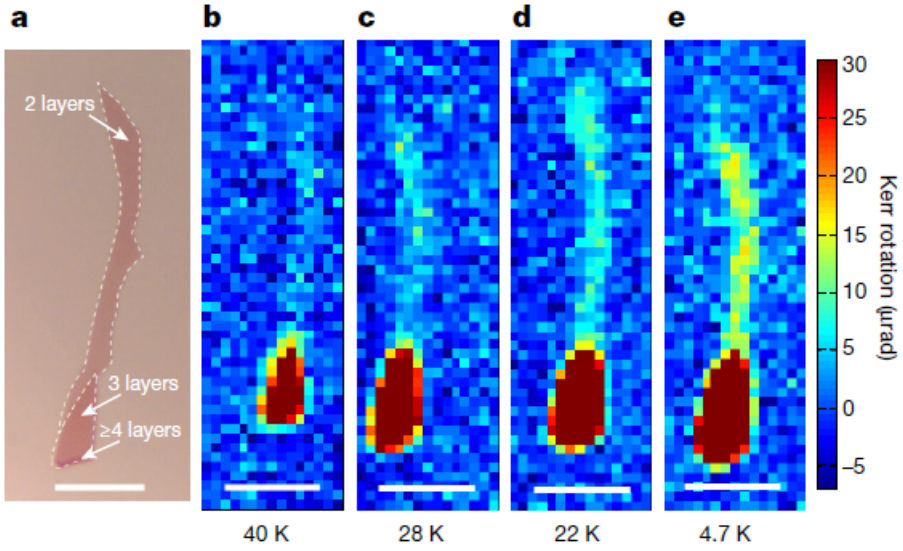

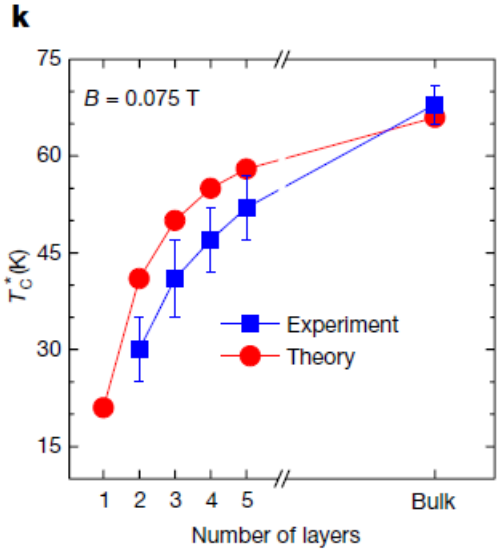

2-D ferromagnet CrI_3(T_c= 60K) and the heterostructure

University of Washington's Xiaodong Xu & MIT's Pablo Jarillo-Herrero

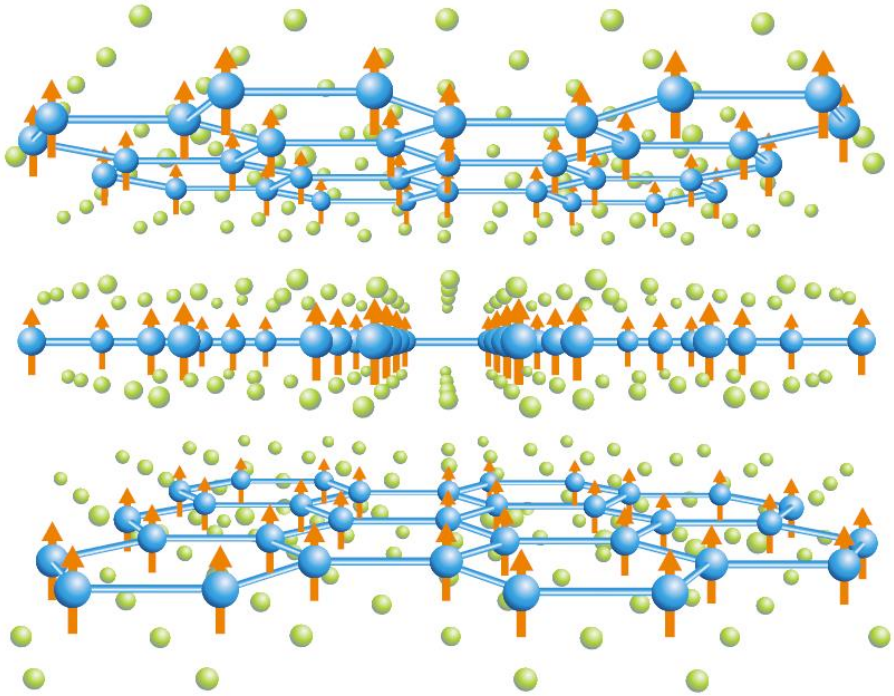

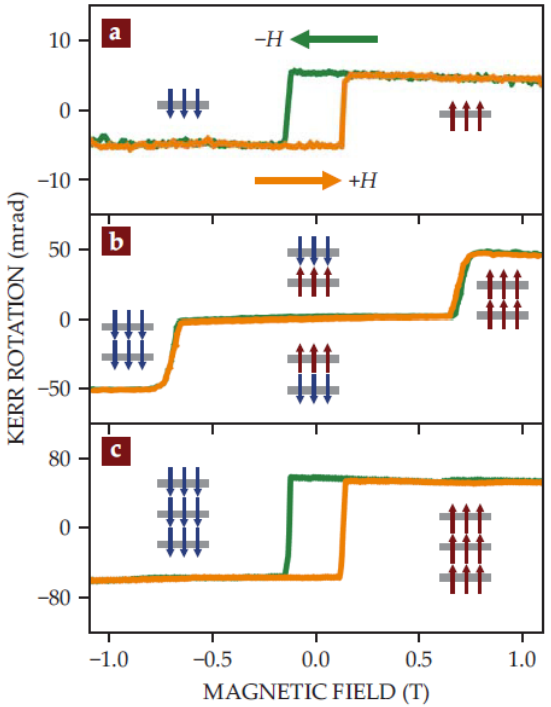

B. Huang et al., *Nature* **546**, 270 (2017).

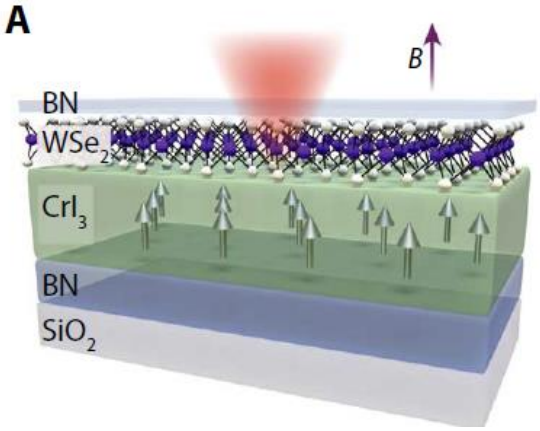

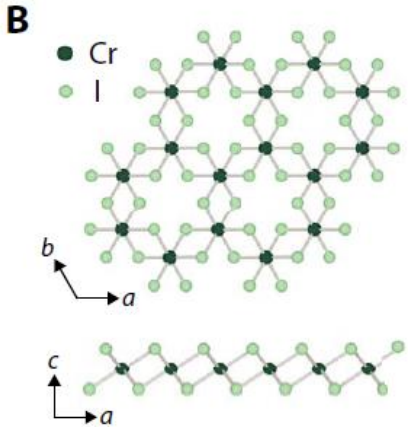

- Van der Waals heterostructures formed by an ultrathin ferromagnetic semiconductor CrI_3 and a monolayer of WSe_2
- Unprecedented control of the spin and valley pseudospin in WSe_2